Final Technical Report on STTR Project DE-FG02-02ER86145

Pressurized RF Cavities for Muon Ionization Cooling

Table of Contents

Overview and Summary

This project was to design and build an RF test cell (TC), which could be operated at 800 MHz, filled with high pressure gases including hydrogen, at temperatures down to that of liquid nitrogen, in strong magnetic fields, in a strong radiation environment, and with interchangeable electrodes, in order to examine the use of high-pressure RF cavities for muon beam cooling.

Many results of this DE-FG02-02ER86145 project are contained in published reports and conference proceedings which are referenced below. Addendum I is a preprint of a paper to the 2006 European Particle Accelerator Conference (EPAC06), which contains the latest measurements using the equipment and procedures developed by the project.

Two test cells were designed and built, and measurements were carried out at Fermilab at the Lab G area and the MuCool Test Area (MTA) [1]. The engineering safety requirements for each TC to allow pressurized hydrogen RF breakdown (sparking) tests were not easily satisfied at a national laboratory and were a significant part of the project [2, and reproduced in part for the MTA case in Addendum II].

Most of the project goals were met in timely fashion with two exceptions which are discussed below. The encouraging result is that RF cavities pressurized with hydrogen gas can be superior to traditional evacuated RF cavities for muon beam cooling. There are also several significant spin-offs from the project, including several new ideas to create muon beams with previously unimagined brightness and, most notably, the rekindling of enthusiasm for an energy frontier muon collider.

For reference, the technical objectives of the Phase I and Phase II components of this project as written in the proposals are reproduced below as the last section of this Overview.

Significant Results

The accomplishments of this project include the measurements for the first time of the breakdown behavior of hydrogen and helium gas and various metallic RF cavity construction materials at 800 MHz as a function of pressure, temperature, and magnetic field. Particularly

---

[1] The RF experimental program in the Fermilab MUCOOL test area.
J. Norem (Argonne) , A. Bross, A. Moretti, Z. Qian (Fermilab) , R.P. Johnson (MUONS Inc., Batavia) , D. Li, M.S. Zisman (LBL, Berkeley) , R.A. Rimmer (Jefferson Lab) , R. Sandstrom (Geneva U.) , Y. Torun (IIT, Chicago) . JLAB-ACC-05-398, PAC-2005-WPAT029, May 2005. 3pp.
http://accelconf.web.cern.ch/AccelConf/p05/PAPERS/WPAT029.PDF

[2] Mark II High-Pressure RF Test Cell Measurements with Molybdenum Electrodes at Lab G, R. E. Hartline, R. P. Johnson, M. Kuchnir, C. M. Ankenbrandt, A. Moretti, M. Popovic D. M. Kaplan, K. Yonehara. Neutrino Factory/Muon Collider Note Number: MUC-NOTE-COOL_EXP-0285
http://www-mucool.fnal.gov/mcnotes/public/pdf/muc0285/muc0285.pdf

noteworthy are the results for pressurized RF cavities operating in strong external magnetic fields, where there is no degradation of maximum gradient even with magnetic fields above 3 T. This implies an additional advantage over evacuated cavities, which have been measured to have a severe reduction of maximum gradient under similar conditions (the maximum gradient in tests at the MTA at 800 MHz was reduced from about 50 MV/m to 16 MV/m in an external field of 2.5 T [3]).

Unanticipated advantages of the pressurized cavities are also noteworthy. The pressurized cavities have very short conditioning times, presumably because multipacting is suppressed, where times of a few hours are typically needed to achieve gradients that typically take weeks to achieve in the case of evacuated cavities. Another aspect of the pressurized cavities is that the absorption of dark current electrons has provided another control variable in the understanding of RF breakdown. We anticipate that models of breakdown that are crucial to the understanding of the 1.3 GHz International Linear Collider (ILC) structures will benefit from insights gained from the study of metallic breakdown in pressurized RF cavities using the apparatus developed in this project.

To achieve the goals of the project, it was necessary to learn how to make pressure seals that were acceptable for RF conductivity and containment of high-pressure hydrogen gas at room and 77 K temperatures [2]. This included the design and construction of a coaxial high-pressure gas barrier to allow RF power to be transferred into the high pressure cavity from the klystron.

Considerable effort was required to satisfy the safety requirements for two different locations at Fermilab (Lab G and the MuCool Test Area (MTA)) for operation of high-voltage apparatus using flammable gases in pressure vessels at cryogenic temperatures. As an amusing aside, this involved satisfying the rules for operation of liquid hydrogen targets, since there was no longer any safety committee at Fermilab capable of assessing gaseous hydrogen operation, in addition to the flammable gas rules. Note that we did not have any liquid hydrogen nor did we have a target. The safety documents for pressure vessel operation, hydrogen use, and oxygen deficiency for the Test Cells used at Lab G and the MTA are reproduced below.

Engineering accomplishments included the conceptual development and first stage ANSYS designs of RF windows to be used in muon cooling applications [4]. In this case, higher gradients can be achieved by using windows made of Al or Be grids to close the openings of the pill box cavities so that the accelerating voltage is not limited by surface gradients at the cavity iris. An essential innovation in the case of pressurized RF cavities is that the grids can be refrigerated by circulating cold hydrogen gas around them, allowing a simpler grid structure with less mass to interfere with the ionization cooling of the muon beams.

---

[3] Moretti et al., LINAC04, http://epaper.kek.jp/l04/PAPERS/TU204.PDF

[4] Thin RF windows for high-pressure gas-filled cavities. M. Alsharoa, R.P. Johnson (MUONS Inc., Batavia) , M. Gosz, D.M. Kaplan, S. Nair (IIT, Chicago) , A. Moretti, G. Romanov (Fermilab). PAC-2005-TPPP053, May 2005. 3pp. http://accelconf.web.cern.ch/AccelConf/p05/PAPERS/TPPP053.PDF

The extrapolations needed to design larger pressurized RF cavities, and in particular, ones that operate at 200 MHz, have been considered since this was one of the items described in the milestone section below. The two most difficult aspects of large pressurized cavities, namely mechanical stability and tuning capability, have rather simple solutions. The mechanical stability is most easily achieved by immersing the entire cavity in a pressure vessel such that the construction of the cavity is no more difficult than any RF cavity (it could be argued it is easier, since in an ordinary cavity there is a one atmosphere difference between the inside and outside). Likewise, the tuning of the cavity is easily achieved by changing the density by varying the temperature and/or pressure and therefore the dielectric of the gas.

Muons, Inc. has designed a 200 MHz cavity, as called for in the milestones, but the actual construction of a prototype will be more expensive than is possible with STTR funding. For example, the 200 MHz normal-conducting prototype RF cavity built by LBNL for the MICE experiment has a budget of more than $500,000.

Derivative Technologies

The original motivation [5] for the concept of pressurized RF cavities was to use them to simultaneously provide the energy absorber for ionization cooling of muon beams and also to provide the reacceleration to replenish the energy lost in the absorber. Thus the cooling of muon beams could be more effective, especially considering the short 2.2 microsecond muon lifetime, if the energy absorber and RF reacceleration components of ionization cooling could be combined to occupy the same real estate.

The realization that high-gradient, pressurized cavities were possible has had profound consequences. The idea of using a continuous, homogeneous gas in a magnetic field that provides the proper dispersion, has led to a revolutionary (and incredibly simple) way to cool the momentum spread of a muon beam. The first public exposition of this STTR project [6] brought the PI into contact with Dr. Yaroslav Derbenev, one of the inventors of the Siberian Snake method of controlling spin resonances in accelerators. The subsequent collaboration has been very fruitful, leading to the concept of the helical cooling channel (HCC) and other new ideas, SBIR/STTR grants, and publications [7,8,9]. The most noteworthy of the applications is

---

[5] Rolland Johnson and Daniel M. Kaplan, MUC/NOTE/COOL_EXP/PUBLIC/195 March, 2001. http://www-mucool.fnal.gov/mcnotes/public/pdf/muc0195/muc0195.pdf

[6] R. P. Johnson, et al. *Gaseous Hydrogen and Muon Accelerators.* International Workshop on Hydrogen in Materials and Vacuum Systems, Newport News, Virginia, 11-13 Nov 2002. Published in AIP Conf.Proc.671:328-336,2003.

[7] High pressure, high gradient RF cavities for muon beam cooling. R.P. Johnson *et al.* Aug 2004. 5pp. Presented at 22nd International Linear Accelerator Conference (LINAC 2004), Lubeck, Germany, 16-20 Aug 2004. http://www.muonsinc.com/reports/TU203.pdf

[8] Six-dimensional muon beam cooling in a continuos, homogeneous hydrogen absorber. Yaroslav Derbenev (Jefferson Lab) , Rolland P. Johnson (MUONS Inc., Batavia) . JLAB-

reproduced as Addendum III to this report [10]. The most exciting new prospect is the concept of the six-dimensional cooling of muon beams to improve the prospects for a muon collider [11].

Once the beams have been cooled to the level achievable by using the high-pressure RF cavities, new ideas for further, sometimes called extreme, cooling become possible [12].

This prospect has been made much more likely by the realization that deep or extreme muon beam cooling may provide a beam small enough that it can be accelerated by the 1.3 GHz RF structures of the ILC [13]. Thus such a muon collider can be considered as an upgrade to the ILC.

The next step will be an experiment to demonstrate the concept of six-dimensional cooling in a continuous absorber imbedded in a HCC [14].

ACP-04-284, May 2003. 4pp. Presented at International Workshop on Beam Cooling and Related Topics (COOL03), Mt. Fuji, Japan, 19-23 May 2003.
Published in Nucl.Instrum.Meth.A532:470-473,2004

[9] High-pressure RF cavities for muon beam cooling. K. Yonehara, D.M. Kaplan (IIT, Chicago) , M. Alsharoa, R.E. Hartline, R.P. Johnson, M. Kuchnir (MUONS Inc., Batavia) , C.M. Ankenbrandt, A. Moretti, M. Popovic (Fermilab). 2005. 3pp.
Prepared for 6th International Workshop on Neutrino Factories and Superbeams (NuFact 04), Osaka, Japan, 26 Jul - 1 Aug 2004. Published in Nucl.Phys.Proc.Suppl.149:286-288,2005
Also in *Osaka 2004, Neutrino factories and superbeams* 286-288

[10] Six-dimensional muon beam cooling using a homogeneous absorber: Concepts, beam dynamics, cooling decrements, and equilibrium emittances in a helical dipole channel. Y. Derbenev (Jefferson Lab) , R.P. Johnson (MUONS Inc., Batavia) . JLAB-ACC-03-177, 2005. 20pp. Published in Phys.Rev.ST Accel.Beams 8:041002,2005
http://www.muonsinc.com/reports/PRSTAB-HCCtheory.pdf

[11]Technical Challenges of Muon Colliderș Rolland P. Johnson, *Muons, Inc.* and Yaroslav Derbenev, *Jefferson National Accelerator Laboratory,* NuFact05
http://www.muonsinc.com/reports/NUFACT05-Johnson.pdf

[12] Recent innovations in muon beam cooling. R.P. Johnson *et al.* 2006. 10pp.
Prepared for International Workshop on Beam Cooling and Related Topics (COOL05), Eagle Ridge, Galena, Illinois, 18 - 23 Sep 2005. Published in AIP Conf.Proc.821:405-414,2006
Also in *Galena 2005, Beam cooling and related topics* 405-414
http://www.muonsinc.com/reports/COOL05-Recent_Innovations.pdf

[13] Muon Acceleration in a Superconducting Proton Linac, Milorad Popovic, *Fermi National Accelerator Laboratory* , and Rolland P. Johnson, *Muons, Inc.,* NuFact05
http://www.muonsinc.com/reports/LinacFrascati.pdf

[14] Letter of Intent to propose a SIX-DIMENSIONAL MUON BEAM COOLING EXPERIMENT FOR FERMILAB. Ramesh Gupta, Erich Willen *Brookhaven National Accelerator Laboratory,* Charles Ankenbrandt, Emanuela Barzi, Alan Bross, Ivan Gonin,

Other Uses of High Pressure RF Cavities

The apparent immunity of hydrogen pressurized RF cavities to external magnetic fields has led to the speculation that the usual frequency-dependence of RF gradient may be completely different than what is experienced in evacuated cavities. That is, much higher gradients may be possible at lower frequencies than is generally though possible, especially at the beginning of a decay channel where the external magnetic fields are large. This might mean new opportunities for muon capture and momentum-time phase rotation to capture a larger fraction of muons into a smaller momentum width than is now considered possible. Also, the gas at the beginning of a channel can provide additional beam cooling [15,16].

Unanticipated delays

The milestones of the project were severely impacted by two unanticipated changes in the availability of Fermilab resources. The first was the early decommissioning of the Lab G experimental area in order to move the 800 MHz klystron to the Linac area to support the operation of the Fermilab Tevatron. This effectively removed our ability to use our test cell from January 2004 until March 2006, when the MuCool Test Area (MTA) was made available. The second change was the redirection of effort to provide the MTA with a beam line.

The two objectives that were not achieved during the course of the project funding period were the operation of the test cell in a magnetic field and the operation of test cell in a radiation field. The first, operation in a magnetic field, was accomplished later under a new Phase I project, DOE STTR DE-FG02-02-05ER86252. The second, operation in a radiation field, awaits the completion of the MTA beam line, which is now scheduled to be completed in summer of 2007.

Stephen Geer, Vladimir Kashikhin, Valeri Lebedev, David Neuffer, Milorad Popovic, Vladimir Shiltsev, Alvin Tollestrup, Daniele Turrioni, Victor Yarba, Katsuya Yonehara, Alexander Zlobin *Fermi National Accelerator Laboratory,* Daniel Kaplan, Linda Spentzouris *Illinois Institute of Technology,* Alex Bogacz, Kevin Beard, Yu-Chiu Chao, Yaroslav Derbenev, Robert Rimmer *Thomas Jefferson National Accelerator Facility,* Mohammad Alsharo'a, Mary Anne Cummings, Pierrick Hanlet, Robert Hartline, Rolland Johnson*, Stephen Kahn, Moyses Kuchnir, David Newsham, Kevin Paul, Thomas Roberts *Muons, Inc.* http://www.muonsinc.com/reports/FNAL%20EXP%206DMANX.pdf

[15] Using high-pressure gas in the front end of a muon source. K. Paul, R.P. Johnson, T.J. Roberts (MUONS Inc., Batavia) , D. Neuffer (Fermilab) , Y. Derbenev (Jefferson Lab). JLAB-ACC-05-360, 2006. 2pp. Prepared for 7th International Workshop on Neutrino Factories and Superbeams (NuFact 05), Frascati, Italy, 21-26 Jun 2005.

[16] Simultaneous bunching and precooling muon beams with gas-filled RF cavities. K. Paul, R.P. Johnson, T.J. Roberts (MUONS Inc., Batavia) , Ya.S. Derbenev (Jefferson Lab) , D.V. Neuffer (Fermilab). JLAB-ACP-05-423, PAC-2005-TPPP055, May 2005. 3pp. Prepared for Particle Accelerator Conference (PAC 05), Knoxville, Tennessee, 16-20 May 2005. Published in *Knoxville 2005, Particle Accelerator Conference* 3295 http://accelconf.web.cern.ch/AccelConf/p05/PAPERS/TPPP055.PDF

In order to expedite the construction of the beam line, Muons, Inc. helped design the beam line [17,18]. Muons, Inc. as part of this STTR project was able to help design the beamline using existing unused magnets for a cost of about $333,000, which was roughly one third of that originally proposed. The report of this design is reproduced as Addendum IV to this report.

Original Technical Objectives from Proposals

The Phase I Project (from original Phase I proposal)

What is planned for the Phase I project (typically, two to three sentences).

The primary goal of Phase I is to build an RF test cell suitable for testing the breakdown characteristics of gases to be used in ionization cooling applications. The test cell will allow the exploration of Paschen's Law, relating breakdown voltages to gas density, over a range of temperatures, pressures, external magnetic fields, and ionizing particle radiation.

Phase I Technical Objectives

The primary goal of Phase I is to build a test cell suitable for measuring the RF breakdown characteristics of gases to be used in ionization cooling applications. For Phase II, the test cell will be used for the exploration of Paschen's Law, relating breakdown voltages to gas density, over a range of temperatures, pressures, external magnetic fields, ionizing radiation, and gases. Determination of the high-voltage breakdown properties of helium gas using this RF test cell at room and liquid nitrogen temperatures will be a measure of the success of the Phase I project.

The optimization of the RF cavity design to be used for an ionization-cooling channel is the primary activity for Phase II of the project. The Phase I test cell is needed for this phase II optimization for two reasons. The first is to confirm and extend the measurements of gas characteristics relating to Paschen's Law. The second reason is to gain experience working in these new conditions. Pressurized, cryogenic RF cavities, as far as we know, have never been built before. Moreover, cryogenic copper RF cavities built to capitalize on lower resistivity do not show up in literature searches, even though there have been suggestions for this application.

Adding to these novel issues that we intend to explore is the use of a large quantity of hydrogen gas in extreme conditions. Thus, our approach will be to commission the test cell using nitrogen and helium gases to gain experience and confidence in the apparatus. Applying the knowledge

---

[17] A Simple beam line for the MuCool test area.
Charles M. Ankenbrandt, David Harding, James Lackey, Elliot McCrory, Milorad Popovic (Fermilab) , Daniel Kaplan, Katsuya Yonehara (IIT, Chicago) , Robert E. Hartline, Rolland P. Johnson (Muons Inc., Batavia). FERMILAB-TM-2243, May 2004. 8pp.
http://www-mucool.fnal.gov/mcnotes/public/pdf/muc0287/muc0287.pdf

[18] Upgrading the Linac 400 MeV Switchyard. Charles M. Ankenbrandt, David Harding, James Lackey, Elliott McCrory, Milorad Popovic, Daniel Kaplan, Katsuya Yonehara, Robert E. Hartline, and Rolland P. Johnson Neutrino Factory/Muon Collider Note Number: MUC-NOTE-COOL_EXP-0294 muc0294.pdf
http://www-mucool.fnal.gov/mcnotes/public/pdf/muc0294/muc0294.pdf

gained in the actual testing of liquid hydrogen absorbers by NIU and IIT at Fermilab, we will be able to move on to the test measurements using cold, pressurized hydrogen gas as part of the phase II project.

The goal of the phase II project is to build a prototype of a 200 MHz cavity, as required by the demands of muon ionization cooling. However, time and availability constraints may dictate that the RF frequency used for the phase I test cavity may be something else. For example, there is an 800 MHz RF system in Lab G at Fermilab that would suit most of our phase I purposes and is operational now. Another test area which is under construction at the end of the 200 MeV Linac at Fermilab will have 200 MHz power available, but is unlikely to be available until 2003, the projected phase II time scale. This Linac test area will be ready in time for phase II tests and is scheduled to have all the additional requirements that we need, including hydrogen safety environment, external solenoidal field, and the 200 MeV H^- Linac beam for radiation tests. In the same spirit as using nitrogen and helium before moving on to hydrogen, we can try working at 800 MHz for Phase I before moving on to 200 MHz. At this higher frequency we can take advantage of an available test set up and also facilitate the project because the components are smaller and easier to build, contain less gas, and are more readily available. For the Paschen curve characteristics that we plan to investigate first, there should be a weak dependence on RF frequency.

The Phase I test cell also will be used to determine the relationship between the power required by an RF cavity as a function of cavity temperature. The 200MHz test cell built during Phase II will be useful for unraveling the frequency dependence of effects like the anomalous skin depth.

The Phase II Project (from original Phase II proposal)

What is planned for the Phase II project - typically, two to three sentences.

The goal of Phase II is to develop RF cavities, which are pressurized with dense hydrogen or helium gas, that are suitable for use in muon cooling and accelerator applications. Measurements of RF parameters (e.g. breakdown voltage, dark current, quality factor) for different temperatures and pressures in magnetic and radiation fields will be made in test cells to optimize the design of prototype cavities for ionization cooling demonstration experiments.

Phase II Technical Objectives

The goal of this project is to develop RF cavities, which are pressurized with dense hydrogen or helium gas, that are suitable for use in muon cooling and accelerator applications. The first step toward that goal is to demonstrate by measurements that there are no intrinsic technical reasons that such cavities are not practical. Measurements of RF parameters (e.g. breakdown voltage, dark current, quality factor) for different temperatures and pressures in magnetic and radiation fields will be made in test cells to demonstrate feasibility and to optimize the design of prototype cavities for ionization cooling demonstration experiments.

The Phase I test cell was needed for this Phase II optimization for two reasons. The first was to confirm and extend the measurements of gas characteristics relating to Paschen's Law. The second reason was to gain experience working in these new conditions. Pressurized, cryogenic RF cavities for a particle beam, as far as we know, have never been built before. Moreover, cryogenic copper RF cavities built to capitalize on lower resistivity do not show up in literature searches, even though there have been suggestions for this application.

Adding to these novel issues that we intend to explore is the use of a large quantity of hydrogen gas in extreme conditions. (Muons, Inc. has the hope that this experience in this project may allow us to contribute to the "hydrogen economy" of the future as part of our commercialization effort.)

The phase II project must arrive at a design of a 200 MHz cavity, as required by the demands of transverse muon ionization cooling. However, the 805-MHz RF system in Lab G at Fermilab suits most of our purposes and is operational now. At this higher frequency we can take advantage of an available test set up and also facilitate the project because the components are smaller and easier to build, contain less hydrogen, and are more readily available. In particular, the LBNL 5 Tesla solenoid is large enough to contain an 805 MHz cavity, but not one of lower frequency. For the Paschen curve characteristics that we plan to investigate, there should be a weak dependence on RF frequency.

Thus the basic Phase II plan is to start with our basic 805 MHz Test Cell design and develop it such that it evolves from a low power device with doorknob electrodes and coaxial pressure feedthrough to a high-power pillbox RF cavity with beryllium windows and a waveguide pressure feedthrough. Each stage of cavity development will be accompanied by more demanding operational tests to add confidence in the feasibility of using pressurized RF cavities as proposed.

The development will involve successive iterations of the components that we have already had experience with. For example, the test cell itself can be improved to allow higher pressures, perhaps up to 130 atmospheres at liquid nitrogen temperature. Another iteration will involve moving to a horizontal geometry with forced LN2 cooling and a cold pressure barrier to allow operation inside the 5-T LBNL solenoid. Larger gaps between the electrodes will allow better understanding of the contributions in the breakdown process from the gas itself and the electrode surfaces (first and second Townsend coefficients). Instrumentation will be added to understand the effects of dense gas on dark currents.

Phase II Performance Schedule

Three months after end of Phase I funding (July 23, 2003)
- Paschen Curve for hydrogen measured to 34 atmospheres and LN2 temperature
- Test Cell redesigned for operation in the LBNL 5 T solenoid and 100 atmospheres
- Improved Coaxial RF Pressure Feedthrough designed and built

Six months after start of funding (October 2003)
- New Test cell constructed, assembled, and tested at low temperature and high pressure
- Measurements of hydrogen Paschen curve in strong magnetic fields
- Studies of electrode materials, dopants, and closed-cell grids begin
- Design and Tests of Waveguide Pressure Feedthrough started

Nine months after start of funding (January 2004)
- 805-MHz Pillbox RF Cavity with Grids and Waveguide designed

Twelve months after start of funding (April 2004)
- 805-MHz Pillbox RF Cavity with Grids and Waveguide built and bench tested

Fifteen months after start of funding (July 2004)
- 805-MHz Pillbox RF Cavity with Grids and Waveguide tested in 5 T solenoidal field

Eighteen months after start of funding (October 2004)
- 805-MHz Pillbox RF Cavity with Grids and Waveguide built and tested in Beam

200 MHz Prototype components designed, constructed

Twenty-One months after start of funding (January 2005)

200 MHz Prototype Components Tested

Two Years after start of funding (April 23, 2005)

200-MHz Pillbox RF Cavity with Waveguide feedthrough designed

Second Test Cell: Design, Engineering, and Operating Requirements

These are the first results from the second (Mark II) 800 MHz RF Test Cell (TC) to be used at Lab G for the study of high voltage breakdown in dense gases. This work is part of a DOE STTR Phase II grant [19] to develop RF cavities that work at high gradient by virtue of being filled with a dense gas to suppress RF breakdown. The cavities are to accelerate muons to be used in a Neutrino Factory, Muon Collider, or Intense Muon Source. The motivation and design requirements for test cells in this study were described previously [20]. The engineering note used for the safety analysis of the Mark II TC is appended to this document and includes ASME pressure vessel calculations and a flammable gas risk analysis. The engineering note for the Mark II used the same 500PSI maximum allowable working pressure as the old TC to simplify safety issues. The November 2003 study reported here had three goals: 1) to compare the new Mark II design with the old TC in the same pressure and temperature conditions, 2) to use molybdenum electrodes to push the hydrogen breakdown measurements to higher densities and voltages, and 3) to study the characteristics of molybdenum as an RF cavity construction material. The Mark II TC worked well; the aluminum seals were much more robust under temperature variations than the lead-tin solder seal of the first TC. The thick stainless steel walls of the Mark II are sufficiently stiff that the gas density can be determined from the resonant frequency, which depends on dielectric. The molybdenum electrodes also worked better than copper, allowing stable surface gradients of almost 80MV/m in hydrogen gas, compared to 50MV/m for copper. As with copper in pressurized gas, the molybdenum conditioned quickly, improving from 70MV/m to almost 80 MV/m in the last 3 hours of testing. It is likely that stable operating surface gradients larger than 80MV/m may be achieved.

Oilcan deformation reduction

The first test cell used at Lab G was limited to pressures of 34 atmospheres because of ASME requirements on the allowable yield strength of the **bolts**. The torque on the bolts that led to this limitation was caused by the "oilcan" deflections of the disks, where the centers of the disks bulge outward and cause the perimeter boltholes to toe inward. Consequently the design of the Mark II TC was modified to double the thickness of the **disks** from 1" to 2" and to increase the bolt (actually threaded rod) diameter from 7/16 inches to 5/8 inches. Only 24 of the larger bolts fit in the available space compared to 32 of the smaller ones in the first TC. Thus the force the bolts provide to contain the gas pressure and to compress the seal has been increased by their cross-sectional area and reduced by their number to give an overall improvement factor of $(24/32)*(10/7)^2=1.5$.

The increased thickness of the disks has reduced the "oilcan" effect. That and the reduction in the average distance from the bolts to the seal and to the center of the disk have effectively eliminated the torque on the bolts. The new ASME calculations in the appendix indicate that the new Mark II TC can operate to 2000 PSI without exceeding the stainless steel yield strength. However, the requirement of derating to 80% of book yield value for non-certified construction gives a maximum allowed working pressure of 1600 PSI.

---

[19] The Phase I proposal can be seen at http://www-mucool.fnal.gov/mcnotes/public/ps/muc0247/muc0247.ps.gz

[20] http://members.aol.com/muonsinc/TC.pdf

Gas temperature stability

Contributing to the additional pressure capability of the Mark II TC is the change in the **cylinder** construction material from copper to stainless steel. The original reasoning for the choice of copper was to have good heat conduction between the LN2 bath and the contained gas to be sure that the gas was at the temperature of the bath since the thermal conductivity of copper is 50 times better than that of stainless steel. Experience from operating the first TC indicated that this precaution was not necessary if an experiment to study breakdown in a gas as a function of pressure started by filling the cavity with gas and waiting until it comes to thermal equilibrium. Subsequent measurements involve only releasing gas from the TC, never letting warm gas enter the TC.

As is seen in figure 1 below and predicted by the calculations in the appended engineering note, the stainless steel provided adequate cooling to the gas to keep it at the temperature of the cooling bath even with all the klystron power going into sparks in the gas. The plots show that the relationship between the Mark II TC resonant frequency and the gauge pressure was linear over a wide range of breakdown conditions. That is, if the breakdowns had caused a temperature increase, the pressure would have increased although the gas density and corresponding dielectric strength would have remained constant since the gas system is closed during measurements.

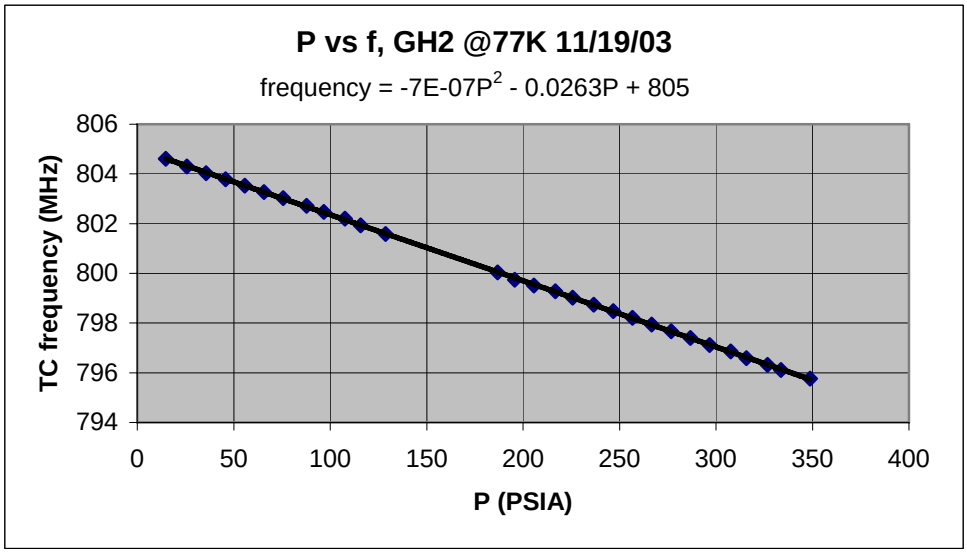

Figure 1. Measurements the Mark II TC resonant frequency and pressure for hydrogen gas at 77K over a wide range of operating conditions with various breakdown rates. The linearity of the plot as seen by the small quadratic coefficient of the fitted curve implies that the gas temperature was constant. The region near 801 MHz corresponds to a breakdown in the waveguide that prevented measurements in the Mark II TC. Below 796 MHz the klystron could not provide enough power cause breakdown.

RF/Pressure seal improvement

Two problems with the Pb-Sn solder RF/pressure seals in the first TC were addressed by changing to 0.017" aluminum gaskets for the Mark II TC. The first problem was that the solder

seals flowed at room temperature under pressure such that gas leaks developed if the TC were not kept cold. Second, the electrical conductivity of the solder did not improve at low temperature compared to the copper such that the Q of the cavity also did not improve as much as expected. The aluminum seals worked well during the experiments reported here, with no detectable gas leaks over several days of operation at room and liquid nitrogen temperatures with pressures up to 500 PSI.

Copper plating consequences

The quality of the Mark II copper plating was not as good as on the first TC. By increasing the thickness of the TC disks we increased their weight to the point that our original vendor could no longer plate them. The plating under the doorknob electrodes seemed particularly vulnerable and 0.017" aluminum gaskets were placed between the plated disks and the new electropolished molybdenum electrodes. The increased capacitance by bringing the two electrodes closer together lowered the resonant frequency of the empty TC to 804 MHz, which had two notable consequences. The first was that with the TC filled with hydrogen at 77K and pressure greater than about 300 PSI, the klystron had to operate so far from its natural frequency that it could not provide enough power to condition the TC. The second consequence was that a resonant breakdown of the klystron waveguide was discovered, which coincided with one region of interest in the measurements of hydrogen breakdown where the Paschen curve meets the breakdown gradient of the metal electrodes.

Molybdenum electrodes

For the experiments reported here, we have used electropolished molybdenum electrodes for the first time. This choice was inspired by reports of success by the CLIC project at CERN operating at 30 GHz with pulse lengths of a few nanoseconds. They reported breakdown surface gradient maxima in ratios of about 1.0: 1.5: 2.0 for copper, tungsten, and molybdenum, respectively. These maxima were obtained after conditioning with millions of pulses, however, so the measurements reported below with limited conditioning time were difficult to predict.

Perry Wilson from SLAC presented a model of electrical breakdown in the October breakdown workshop at Argonne, in which he predicted that chromium should be even better than molybdenum. We have ordered a pair of chrome-plated electrodes to use in tests at Lab G in January 2004.

A small hole has been added in the side of each electrode so that a special tool can be used to secure it to the copper disk for good electrical contact.

Measured TC parameters and calibrations

A network analyzer was used to measure the Q_o of the old and new test cells and to calibrate the pickup probe at room temperature and at liquid nitrogen temperature. The program SuperFish was used to calculate the ideal Q_o and shunt impedance of the cavity from which the power for a given gradient was calculated. The first TC had a measured Q_o of 25,300 at 77 K and 13,600 at room temperature. The Mark II TC had a measured Q_o of 26,540 at 77 K and 14,345 at room temperature. The calculated room temperature Q_o for the TC geometry is 19,200. The measured room temperature Q_o is about 30 % lower than calculated for each. This, however, is within the expected normal range for cavities that are bolted together. One normally comes within 5 % of calculation with high purity copper cavity brazed or electron-beam welded together and with only a few small ports. The slightly better room temperature Q_o of the Mark II TC compared to the old TC may be an indication that the new aluminum seals are better than the Pb-Sn solder, especially since the molybdenum electrodes should have made the Q_o worse.

For the old and the new TC, the Q_o improved a factor of 1.85 at 77 K compared to room temperature. The resistance ratio for pure copper over this temperature range is 8. This corresponds to an expected Q_o improvement factor of 2.82 for highly purified copper since Q is inversely proportional to the square root of the resistively. However, neither TC was constructed of high purity copper.

The changes in the TC design may have had offsetting effects. The first TC had high-purity copper electrodes and cylindrical wall and only the disks were copper-plated. The Mark II TC was entirely copper-plated and had molybdenum electrodes. For these reasons the old TC should have had better Q_0 at low temperature. On the other hand, the lead-tin solder seals of the old TC should have had worse low temperature behavior than the aluminum seals of the Mark2TC. The relative importance of these construction parameters is yet to be sorted out.

Gas density from TC resonant frequency

A notable observation is that the stiffness of the Mark II TC allows a direct measurement of the gas density by measuring its resonant frequency. In the old TC, the oilcan distortion of the disks was a complication that confused this realization. With this distortion, the TC volume increases causing the frequency to decrease as a function of pressure. The distortion also causes the electrodes to separate as a function of pressure, causing the resonant frequency to rise because of decreased capacitance. With the new TC, these two effects are negligible. The TC resonant frequency is now only a function of the dielectric of the contained gas, which increases with gas density. Since the Q of the cavity is high, the resonant frequency during operation is easily and accurately determined by changing the klystron frequency to maximize the amplitude of the probe signal on the oscilloscope as shown in figure 2. There is no need now to have a means to directly measure the temperature of the gas in the Mark II TC.

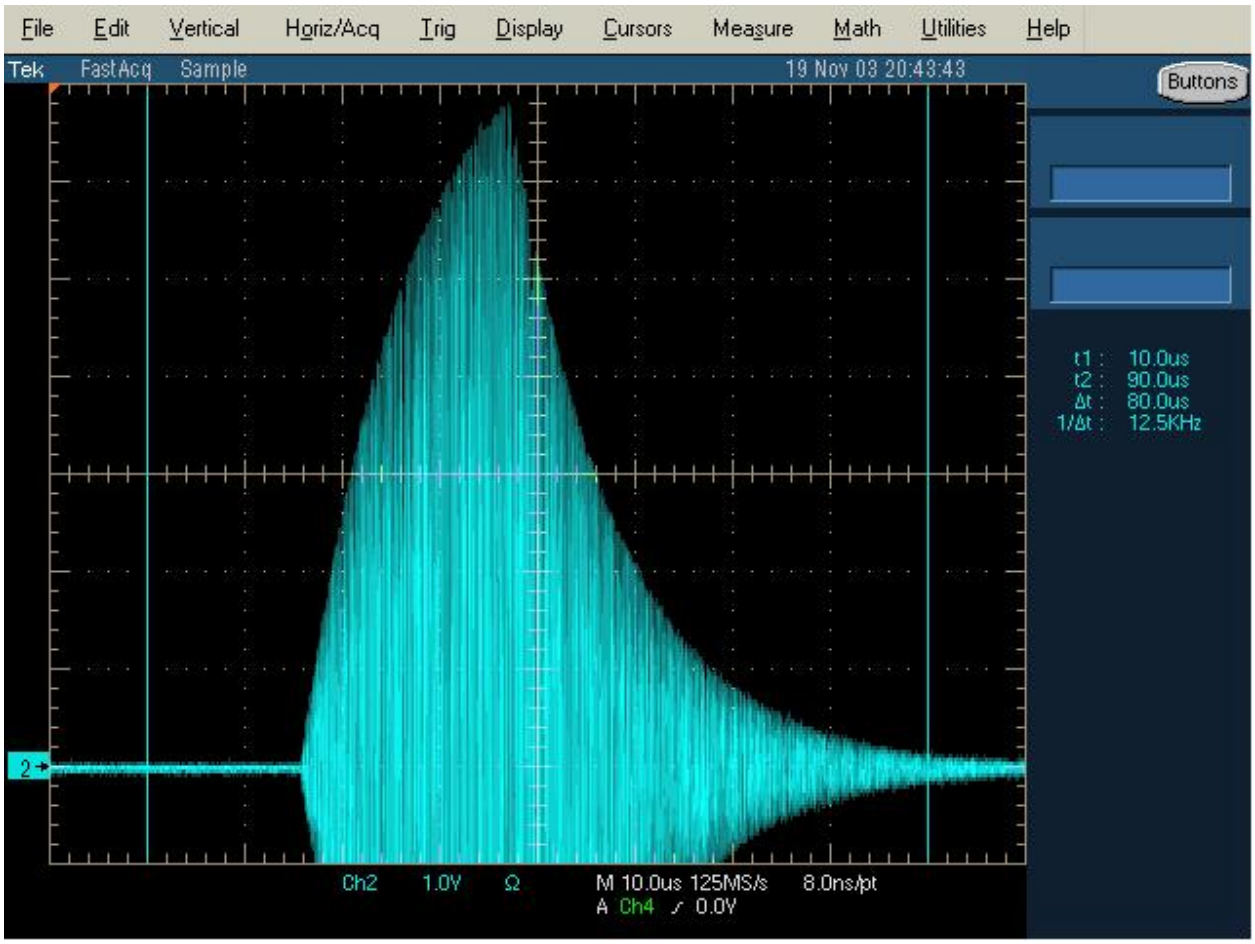

Figure 2. The probe signal taken during the last hours of operation at 250PSI and 77K. The pulse time of 20 μs corresponds to the rising part of the 800MHz envelope. The peak amplitude of 6.8Volts is measured after a 10x attenuator giving 68V on the probe and 68*1.17=79.9MV/m estimated gradient at the surface of the molybdenum electrodes.

Helium data

First measurements at room temperature

Figures 3 and 4 show the first Paschen curve data from the Mark II TC using helium at room and liquid nitrogen temperatures, respectively, taken on November 15. These data compare well to those taken with the first test cell in April 2003, where 28 MV/m was achieved at 77K and 500 PSI. The room temperature expectation is then 28*77/300=7.2 MV/m.

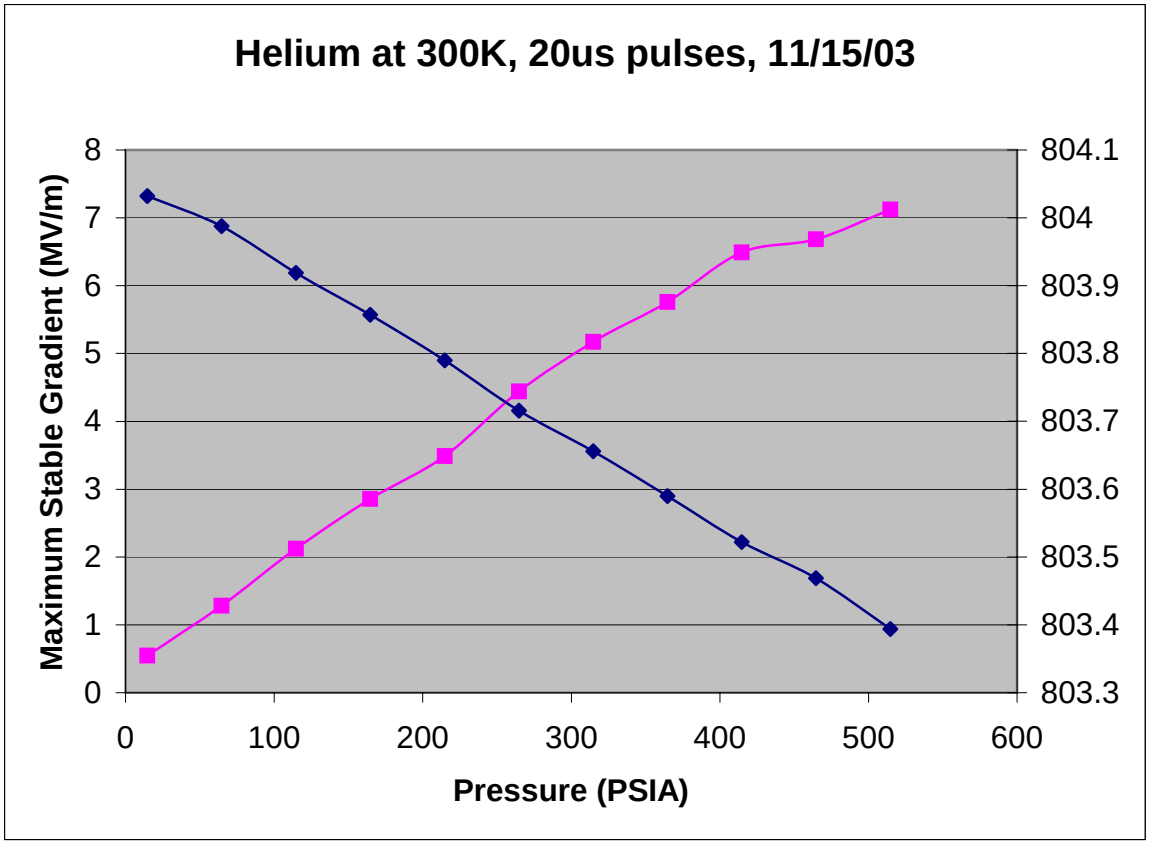

Figure 3. First Mark II Paschen curve measurements for helium at room temperature. The red points are maximum stable gradients, the blue points are Mark II TC resonant frequencies

.

First measurements at LN2 temperature

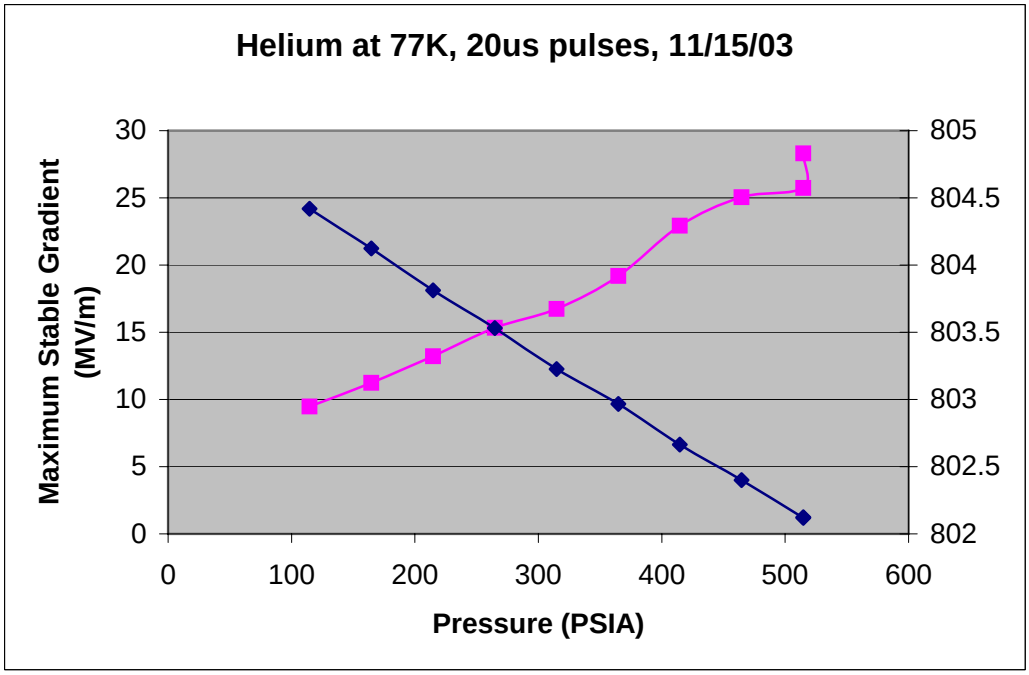

Figure 4. First Mark II TC Paschen curve measurements for helium at liquid nitrogen temperature. The higher gradient point at 514.7 PSIA represents 30 additional minutes of conditioning after the lower point was determined.

Flood in Lab G

After the data in figures 3 and 4 were taken, a heavy rainstorm interrupted operation. During the time of recovery, the Mark II TC was warmed and opened to air. Figure 5 is then a repeated measurement of the data shown in figure 4, four days later.

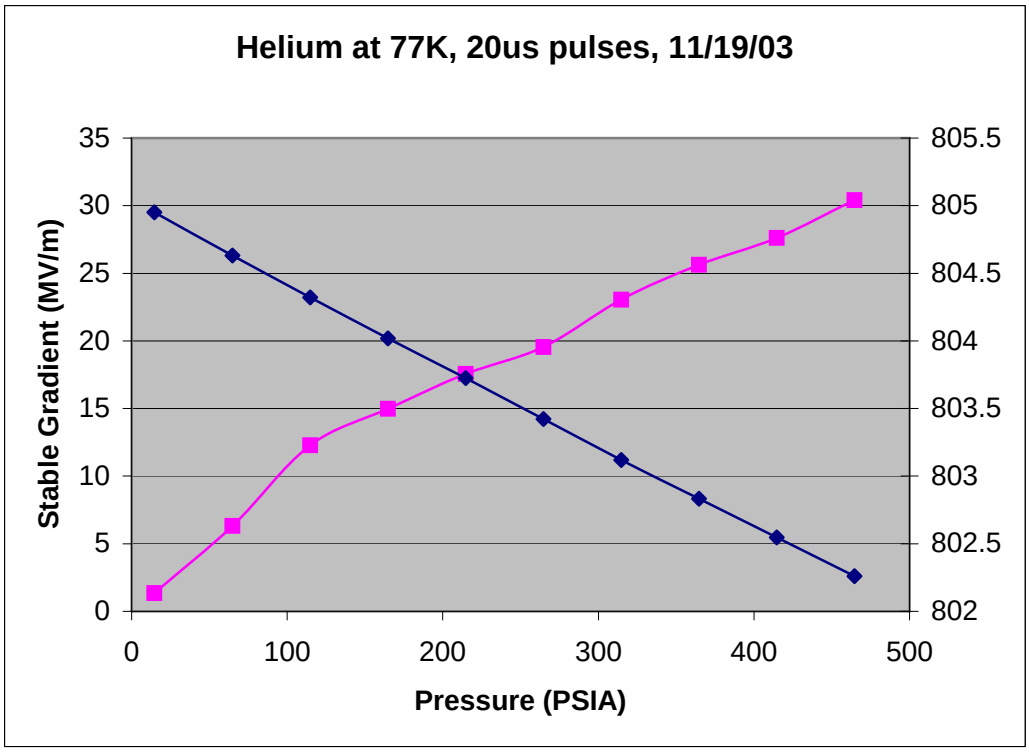

Figure 5. Repeat of the Paschen curve measurements for helium at liquid nitrogen temperature after the lab G flood.

Hydrogen data

Figure 6 shows the maximum stable gradients for hydrogen at 77K. The plot has data from two data acquisition sequences that each start from high-pressure and step downward by venting gas from the Mark II TC. Together the two sequences give a good picture of the character of the data. At high pressure, small changes in the pressure (or corresponding frequency) cause large changes in the maximum stable gradient. At lower pressure, the maximum stable gradient increases linearly and very reproducibly with pressure. This linear region is what we call the Paschen curve region. (The points at zero gradient are artifacts of the plotting program.)

The dip in the stable gradient data centered at 190 PSIA seems to be due to a breakdown in the waveguide. This breakdown has been studied subsequent to our studies and it has been verified that it is not related to the test cell and repeats at intervals of 7 MHz.

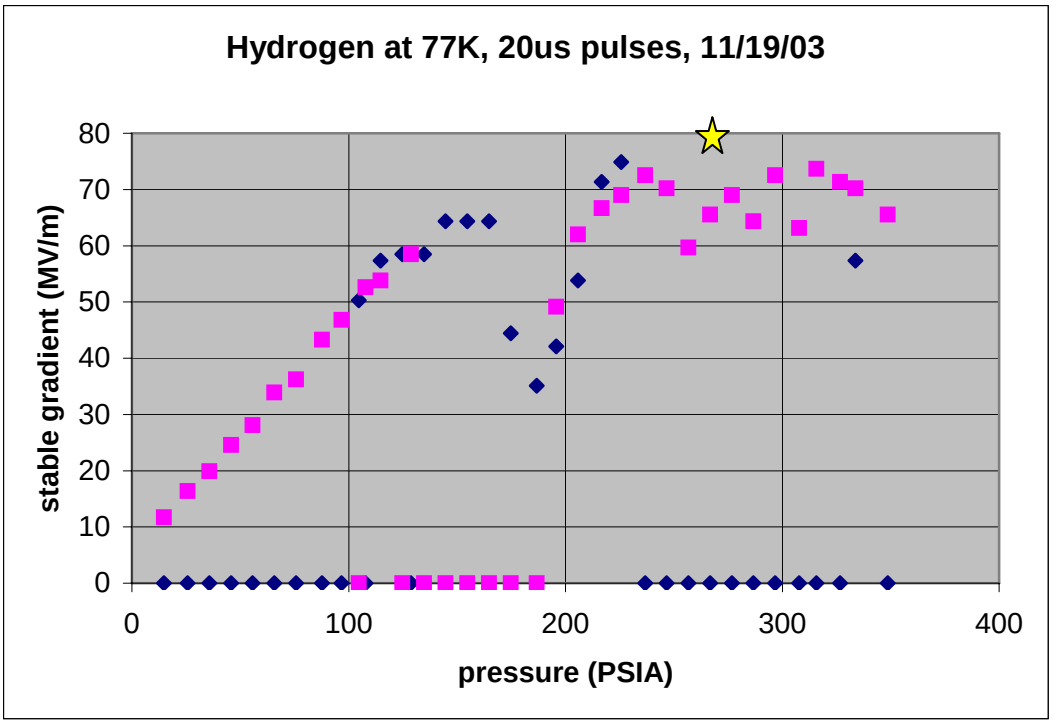

Figure 6. Paschen curve measurements for hydrogen at liquid nitrogen temperature. The blue and magenta points indicate two separate data runs. The points at zero gradient are artifacts of the plotting program. The gold star represents the result of the last 3 hours conditioning at 265 PSIA, where a maximum stable gradient of 79.9MV/m was attained.

Similar to the experience with copper electrodes, the molybdenum conditioned quickly. At a particular setting above the Paschen region it took about 3 hours to increase the stable operating gradient from 70 to 79.9MV/m. However, evidence of minor pitting on the electrodes suggests that the pulse length should be shortened as the breakdown gradient increases in order to condition the metal surface with smaller breakdown discharges.

Extrapolations

These latest measurements of the Paschen curve in hydrogen have the widest range of pressures we have used at 77K and can be used to estimate the breakdown suppression that could be expected with operating conditions we hope to achieve. Extrapolating to 110 atmospheres pressure, where the gas density is about half of liquid hydrogen density, the breakdown suppression should be about 690 MV/m. This number is important to us as a measure of how well the cavities will withstand the ionization created by an intense muon beam.

Assuming no distortion of the Mark II TC, the change in the resonant frequency from no pressure to 110 atmospheres is 42 MHz or 5.2 %. This is another important parameter for us for the design of cavities to be used in a real muon-cooling channel. That is, certain modes of operation may require the ability to tune the cavities.

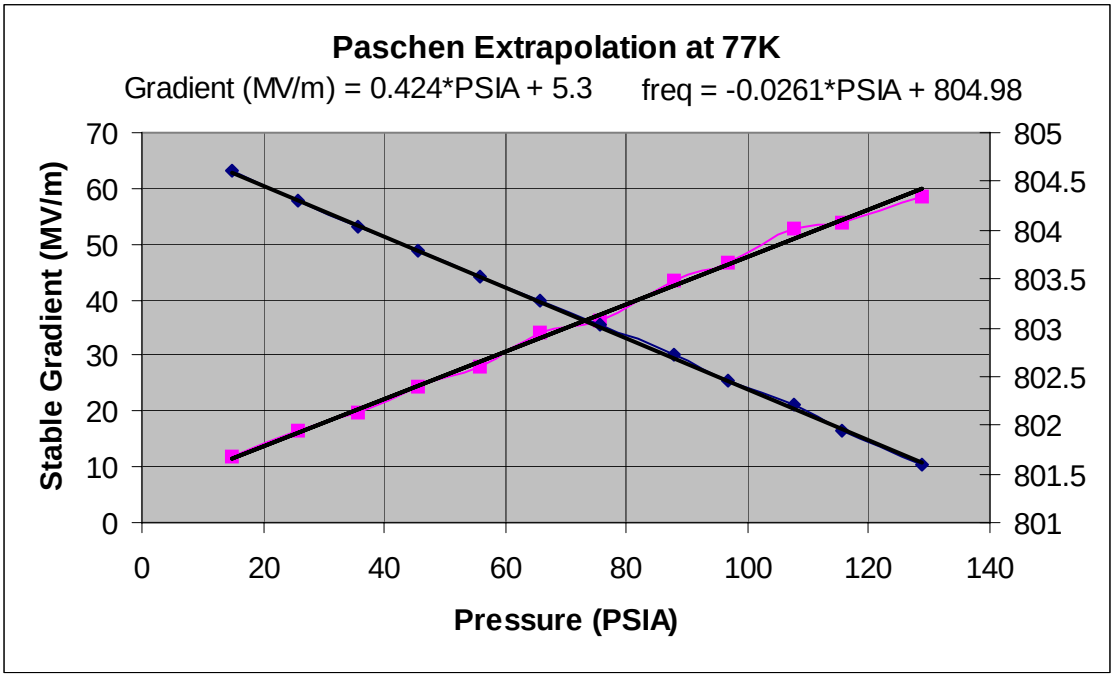

Figure 7. Linear fits to the data from the Paschen region.

HIGH PRESSURE RF CAVITIES IN MAGNETIC FIELDS *

P. Hanlet#, M. Alsharo'a, R. E. Hartline, R. P. Johnson,
M. Kuchnir, K. Paul, Muons Inc, Batavia, IL 60510, U.S.A.
C. M. Ankenbrandt, A. Moretti, M. Popovic, FNAL, Batavia, IL 60510, U.S.A.
D. M. Kaplan, K. Yonehara, IIT, Chicago, IL 60616, U.S.A.

Abstract

The RF breakdown of dense hydrogen gas between metallic electrodes has been studied as part of a program to develop gas-filled RF cavities to be used for muon ionization cooling. A pressurized 805 MHz test cell was used at Fermilab to measure the increase in the breakdown threshold as a function of gas density, known as the Paschen effect. The breakdown behavior of copper, molybdenum, and beryllium electrodes as functions of hydrogen gas density are also reported. First results are reported of RF breakdown using molybdenum electrodes in dense hydrogen in a strong external magnetic field. Unlike evacuated cavities, the pressurized cavity shows no degradation of maximum stable gradient with increasing magnetic field.

INTRODUCTION

Most RF cavities associated with particle accelerators operate in excellent vacuum to avoid electrical breakdown. Electrons or ions that are accelerated by the high voltages in an evacuated RF cavity rarely encounter atoms of residual gas, so the avalanche process of breakdown does not occur. Other RF systems that do not require the ultrahigh vacuum of an accelerator typically suppress RF breakdown by using dense materials between electrodes. Ions passing through these materials, which include high-pressure and/or high-density gases, have such a short mean free path between collisions that they do not accelerate to energies high enough to create an avalanche. The relationship between the electrical breakdown voltage and the product of gas pressure and gap width is known as Paschen's Law. Based on the argument above, the threshold gradient for high voltage RF breakdown of a gas should depend on the gas density [1], the form of Paschen's Law that we will use.

This idea of filling RF cavities with gas is new [2,3] for particle accelerators and is only possible for muons because they do not scatter as do strongly interacting protons or shower electromagnetically as do less-massive electrons. The interest in intense muon beams, muon colliders, and neutrino factories based on muon storage rings has lead to interest in muon accelerators, and thus the need for muon beam cooling. Besides suppressing breakdown, the gas in the cavities also acts as the energy absorber needed for ionization cooling [4], where the angular spread in a beam is reduced by passing the beam through an absorber to reduce all momentum components and RF acceleration is used to replace the longitudinal component.

Although this dual function of suppressing RF breakdown and providing simultaneous energy loss for ionization cooling is the primary motivation for the development of such pressurized RF cavities, there is another very important function. That is, pressurized RF cavities can provide a continuous absorber for ionization cooling which can be used to cool the longitudinal motion of a muon beam [5,6]. This is achieved by providing a magnetic field to create dispersion such that higher momentum particles have a larger path length and correspondingly larger energy loss in the continuous absorber.

For ionization cooling, hydrogen and helium are the best gases because of their favorable energy loss and radiation length. However, hydrogen is superior in all aspects except for safety concerns. Hydrogen gas has over twice the ionization cooling effectiveness as helium in that it allows a final cooled emittance that is smaller by a factor of 1.5 in each transverse plane. At the same pressure, hydrogen suppresses RF breakdown at a voltage that is six times higher than helium [7]. Hydrogen is also superior in heat capacity and viscosity, which are important parameters for the engineering of a practical cooling channel.

APPARATUS

The Test Cell (TC) is a cylindrical RF cavity used for testing in the MuCool Test Area (MTA) at the Fermi National Accelerator Laboratory (Fermilab). The TC is made of copper-plated stainless steel, and has inner height by diameter dimensions of 3.2 x 9.0 in^2. Within the TC, two replaceable 1 inch radius hemispherical electrodes are mounted along the cylindrical axis as shown in figure 1. The cavity is powered at 805 MHz by a klystron located in the Fermilab Linac gallery via an 87 m waveguide and short coaxial line, which has an epoxy-sealed pressure barrier 23 inches from the TC. A capacitively coupled pickup (PU) probe is mounted in the upper plate of the TC to measure the RF voltage as shown in figure 1. In addition to the pickup probe inside the cavity, there are two sets of directional couplers (DC) along the coaxial line which are used to measure the transmitted and reflected voltages into or from the cavity.

The cavity is designed to have a resonant frequency of 805 MHz and to couple to a 50 Ohm impedance waveguide/coaxial line. For an ideal pillbox cavity, the resonant frequency is given by $\nu_0 = 2.405/\sqrt{\varepsilon\mu R}$, where

* Supported by DOE STTR Grants DE-FG02-02ER86145 and -05ER86252
# hanlet@muonsinc.com

2.405 is the first zero of the first regular Bessel function, and R is the radius of the cavity. Since the material used in the cavity is non-magnetic, then $\mu=\mu_0$. The electrodes modify the TC behavior such that it does not act as in ideal pillbox cavity; however, the gas density within the cavity still determines ε and changes the resonant frequency by as much as 10 MHz over the range of densities of interest. Depending on the power required, the practical range of tuning for the klystron is about $\nu \sim 805\pm5$ MHz, so that the TC has to be shimmed according to the expected frequency range of the planned experimental conditions. Circular 15 mil aluminum shims between the electrodes and the end plates are used to adjust the TC resonant frequency primarily by changing the capacitance due to the gap between the electrodes.

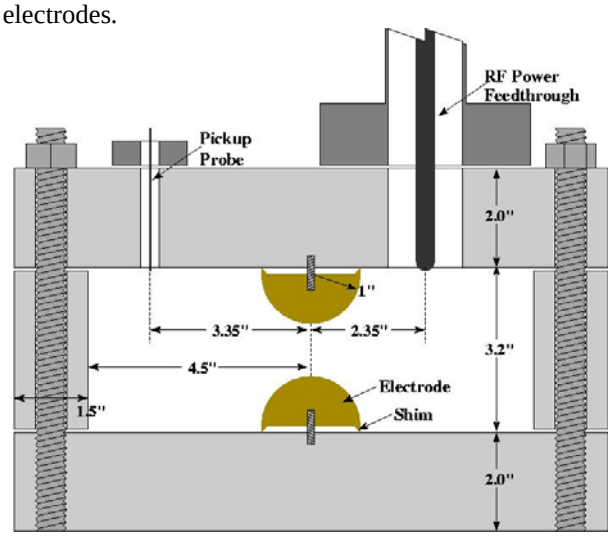

FIG. 1: Cross section of the test cell showing the replaceable one inch radius Cu, Mo, or Be hemispherical electrodes. The top and bottom plates and the cylinder are copper-plated stainless steel (the gas input/exhaust port is not shown in the figure).

Small deviations from perfect coupling from the waveguide/coax to the cavity generate reflections of the RF signal due to impedance mismatch. Over the long length of waveguide between the klystron and the MTA, these reflected waves can add constructively to produce resonances. It was important to avoid running at frequencies where these resonances appeared, so the gas pressures were chosen to yield frequencies between these resonances.

A network analyzer was used to measure the quality factor Q_o and calibrate the pickup probe. The programs SuperFish and ANSYS were used to calculate the ideal Q_o and shunt impedance of the cavity from which the power for a given gradient was calculated. Effectively, the programs related the voltage at the pickup to the maximum surface gradient on the electrodes for the ideal quality factor. The ratio of the measured to ideal quality factor was then used to renormalize the pickup sensitivity.

The procedure for taking data was to set the gas pressure in the cavity, adjust the klystron frequency to match the resonant frequency in the cavity, and then ramp up the klystron power until a breakdown occurred. The power was then reduced until the signal was stable in the cavity; at this point the frequency, drive power, and voltages from the pick up and directional couplers were recorded.

Figure 2 is a picture of the TC in the MTA next to the LBNL superconducting solenoid used for the data shown in figure 3.

FIG. 2: Photograph of the Test Cell in the MTA next to the LBNL superconducting solenoid.

DATA AND DISCUSSION

The data for the external magnetic field both on and off are shown in figure 3. The lower-pressure region in which the maximum stable gradient rises linearly with absolute pressure is called the Paschen region and is determined by the breakdown of the gas. The usual model for this is that increased gas density reduces the mean free collision path for ions or electrons so they have less chance to accelerate to energies sufficient to initiate showers. Within errors, the measurements in the Paschen region seem independent of electrode material and magnetic field.

At higher gradients, the metallic material of the electrodes breaks down. We have studied three electrode materials in order to find the best material for muon cooling applications and to test some theories of RF breakdown. Copper is the standard for RF cavities, molybdenum is a hard material expected to have good resistance to breakdown, and beryllium has a low atomic number that might be useful for ionization cooling of muon beams. As noted in earlier reports, the TC in the electrode-breakdown pressure region conditions quickly with no evidence of multipacting. But because of the short time available for the studies, we cannot be sure that the maximum gradients that were achieved could not have been higher.

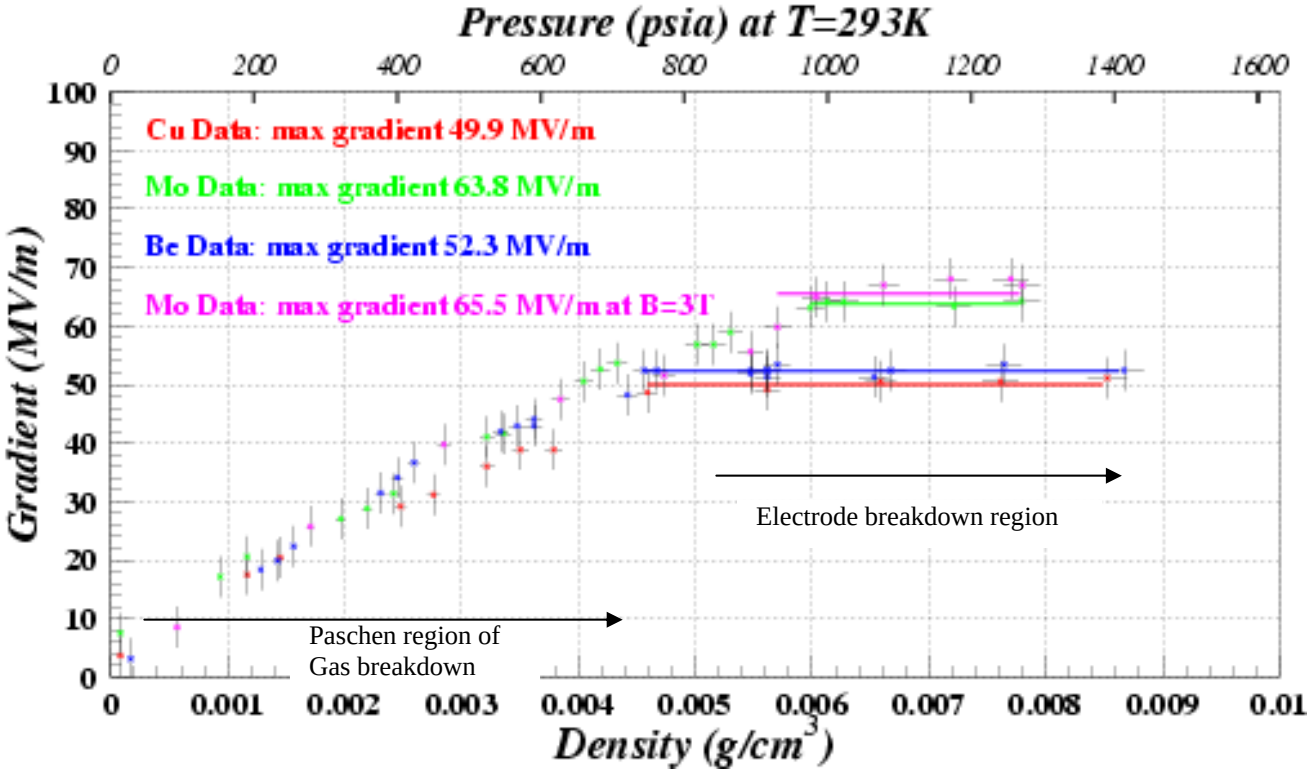

FIG. 3: Measurements of the maximum stable TC gradient as a function of hydrogen gas pressure at 800 MHz with no magnetic field for three different electrode materials, copper (red), molybdenum (green), and beryllium (blue). As the pressure increases, the mean free path for ion collisions shortens so that the maximum gradient increases linearly with pressure. At sufficiently high pressure, the maximum gradient is determined by electrode breakdown and has little if any dependence on pressure. Unlike predictions for evacuated cavities, the Cu and Be electrodes behave almost identically while the Mo electrodes allow a maximum stable gradient that is 28% higher. The cavity was also operated in a 3 T solenoidal magnetic field with Mo electrodes (magenta); these data show no dependence on the external magnetic field, achieving the same maximum stable gradient as with no magnetic field.

We found that copper and beryllium electrodes operated stably with surface gradients near 50 MV/m while molybdenum achieved values near 65 MV/m. These are considerably different than most models of breakdown in evacuated cavities predict [8].

The maximum stable gradient was unaffected by the magnetic field for the molybdenum electrodes, the only material tested in the external magnetic field so far. This is considerably different than measurements at 800 MHz in evacuated copper cavities indicate, where the maximum surface gradient is reduced from 50 MV/m to 16 MV/m in going from 0 to 2.5 T external field [9]. Future tests will include W, Be, and Cu electrodes in the external magnetic field.

REFERENCES

[1] Sanborn C. Brown, Basic Data of Plasma Physics, The Fundamental Data on Electrical Discharges in Gases, American Vacuum Society Classics, AIP Press, 1993.

[2] Rolland Johnson and Daniel M. Kaplan, MUC/NOTE/COOL_EXP/PUBLIC/195 March, 2001

[3] R. P. Johnson, et al. *Gaseous Hydrogen and Muon Accelerators.* International Workshop on Hydrogen in Materials and Vacuum Systems, Newport News, Virginia, 11-13 Nov 2002. Published in **AIP Conf.Proc.671:328-336,2003.**

[4] Daniel M. Kaplan**,** Introduction to Muon Cooling, http://www.slac.stanford.edu/econf/C010630/papers/M102.PDF

[5] Y. Derbenev and R. P. Johnson, Phys. Rev. ST Accel. Beams 8, 041002 (2005)

[6] S. Kahn, H. Kirk, A. Garren, F. Mills and D. Cline, http://hadron.kek.jp/Nufact/Kahn_WG3.ppt

[7] R. P. Johnson et al., proceedings of LINAC2004, http://bel.gsi.de/linac2004/PAPERS/TU203.PDF

[8] Perry Wilson, Theoretical Prediction for the .., http://www.slac.stanford.edu/grp/ara/HGWorkshop/THEORY%20OF%20RF%20BREAKDOWN.pdf

[9] Moretti et al., LINAC04, http://epaper.kek.jp/l04/PAPERS/TU204.PDF

Addendum II: Test Cell Design and MTA Safety Requirements
Pressure Vessel Engineering Note

PRESSURE VESSEL ENGINERING NOTE PER CHAPTER 5031

Prepared by: **Rolland Johnson/Pierrick Hanlet**
Preparation date: **7 September, 2005**

1. Description and Identification

Fill in the label information below:

This vessel conforms to Fermilab ES&H Manual
Chapter 5031

Vessel Title **MTA Mark II High-Pressure RF Test Cell**

Vessel Number_____RSB-570 _____ ←**Obtain from Division/Section Safety Officer**

Vessel Drawing Number _____

Maximum Allowable Working Pressures (MAWP):
Internal Pressure ___**1600 psi**_____
External Pressure _____**N/A**_____
Working Temperature Range: **77K-293K**
Contents **H_2 or He**
Designers/Manufacturer
Rolland Johnson, Robert Hartline/Muons, Inc.
Test Pressure (if tested at Fermi) Acceptance Date: ←**Document per Chapter 5034 of the Fermilab ES&H Manual**

___2,000____PSIG, Hydraulic_____Pneumatic ___X_____
Accepted as conforming to standard by

_____

of Division/Section__Beams Div._ Date:_____ ←**Actual signature required**

NOTE: Any subsequent changes in contents, pressures, temperatures, valving, etc., which affect the safety of this vessel shall require another review.

Reviewed by: _____ Date: _____

Amendment No.:	Reviewed by:	Date:
_____	_____	_____
_____	_____	_____

Lab Property Number(s): **Property of Muons, Inc.**
Lab Location Code: **MuCool Test Area (MTA)** (obtain from safety officer)
Purpose of Vessel(s): **The device is an experimental research instrument being developed to measure high-voltage RF breakdown in high-pressure gases**

Vessel Size/Capacity: I. **Diameter: *9 in* Length: *3.2 in*, Volume *0.12 ft*^{3}** or ***3.3 l***

(Note: The capacity of gas is reduced by the particular choice of internal electrode geometry (*4.2 in*^{3} or *~0.07 l*) and, depending on the calculation of interest, can be increased by the pressurized volume of the attached coaxial RF pipe (*~0.9 l*)).

Normal Operating Pressure (OP) **0 to 1600 *psi***
MAWP-OP = **1600 *psi***

List the numbers of all pertinent drawings and the location of the originals.

Drawing #	Location of Original
Top Plate Schematic	Figure 3 below
Test Cell Schematic	Figure 4 below

2. Design Verification

Is this vessel designed and built to meet the Code or "In-House Built" requirements?
Yes__**X**__ No____.

If "No" state the standard that was used _____.
Demonstrate that design calculations of that standard have been made and that other requirements of that standard have been satisfied.
Skip to part 3 "system venting verification."

Does the vessel(s) have a U stamp? Yes_____ No__**X**__. If "Yes", complete section 2A; if "No", complete section 2B.

Provide ASME design calculations in an appendix. On the sketch below, circle all applicable sections of the ASME code per Section VIII, Division I. (Only for non-coded vessels)

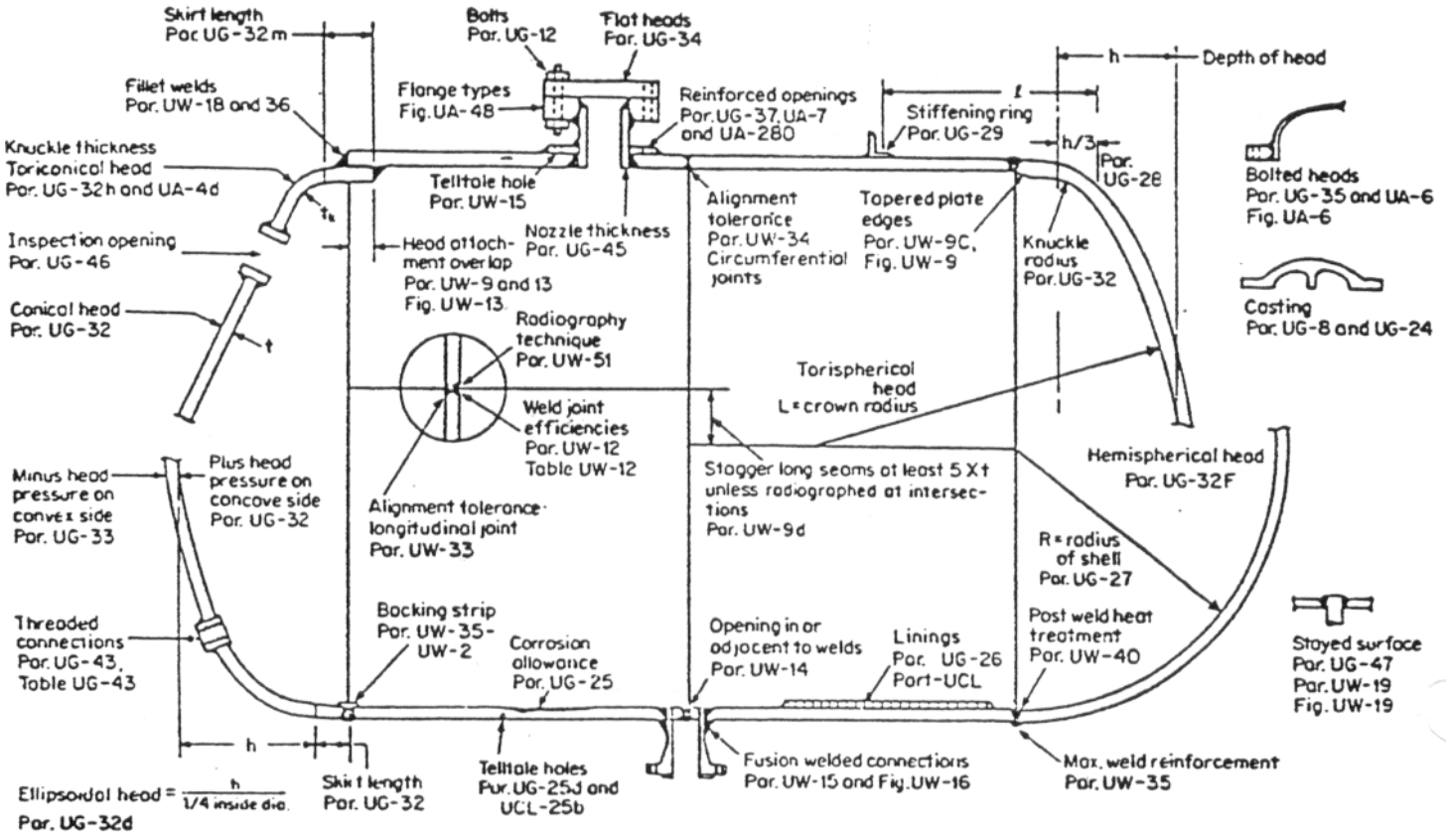

Figure 1: ASME Code: Applicable Sections

2B.

Summary of ASME Code

Item	Reference ASME Code Section	CALCULATION RESULT (Required thickness or stress level vs. actual thickness calculated stress level)
Disks	UG-34 Flanges	See MSG-EAR-03, below
Cylinder	UG-27	See MSG-EAR-03, below
Bolts	UG-12	See MSG-EAR-03, below
Holes in Top Plate		See MSG-EAR-03, below

3. System Venting Verification

The vent system and the operational procedures are discussed in the flammable gas analysis section below.

Discussions of gas flow requirements for the MTA experimental hall are in sections titled "Chapter 3: Note on Flow Rates of Compressible Gases through Pipes and Valves" and "Chapter 4: Additional Test Cell Venting Requirements". There is additional discussion in the section below.

Does the venting system follow the Code UG-125 through UG-137?
Yes _**X**_ No___

Does the venting system also follow the Compressed Gas Association Standards S-1.1 and S-1.3?
Yes _**X**_ No___

A "no" response to both of the two proceeding questions requires a justification and statement regarding what standards were applied to verify system venting is adequate.

List of reliefs and settings:

Manufacturer	Model #	Set Pressure	Flow Rate	Size
Anderson Greenwood	81MS44-4	1600 *psi*	125 *cfm*	0.5 *in*

Note: the H_2 regulator is a Matheson model 2-580, with a maximum flow of 600 *cfm*.

4. Operating Procedure

Is an operating procedure necessary for the safe operation of this vessel?
Yes _**X**__ No____ (If "Yes", it must be appended)
See "Chapter 7: TC Operation Procedures".

5. Welding Information. **This device has no welds.**

6. Existing, Used and Unmanned Area Vessels

Is this vessel or any part thereof in the above categories?
Yes_____ No ___**X**__

7. Exceptional Vessels
Is this vessel or any part thereof in the above category?
Yes_____ No __**X**___

Introduction and Motivation

Pierrick Hanlet, 13 July 2006

Description

Our tests are to be performed at the MuCool Test Area, or ***MTA***, which has been designed and built specifically for the MuCool collaboration. The experimental hall has dimensions: $V = 21ft \times 41ft \times 16ft4in \approx 14{,}063\,ft^3 = 398.2m^3$ plus a "pre-cast'' volume for a future beamline of $V \approx 10\,ft \times 10\,ft \times 25\,ft = 2{,}500\,ft^3 = 70.7m^3$; totaling $V = 16{,}563\,ft^3 = 468.9m^3$.

All tests will be performed using the Muons Inc test cell, or ***TC***. This device, shown in Figs.2-4, is a pill-box shaped pressure vessel constructed of copper coated stainless steel. The end plates are *2 in* thick. The cylinder is *1.5 in* thick and 9 *in* internal diameter and has an internal length of 3.2 *in,* thus having a total volume of:

$$V = \pi(4.5in)^2 \times 3.2in = 203.6in^3 = 3{,}336cm^3 = 3.336 \times 10^{-3} m^3 = 3.336l$$

Internal to the TC will be a pair of electrodes under investigation, see Fig. 4. These electrodes are *1 in* radius hemispheres and will be placed along the cylindrical axis.

Liquid H_2, or LH_2, has a density of $\rho = 0.071g/cm^3$. Ultimately, the TC will be filled with gaseous H_2 at a density that is half that of LH_2, by cooling the TC and gas to LN_2 temperature, $T = 77K$, at a pressure of $P = 1{,}600\,psi = 11.03MPa$. Some tests will be performed at room temperature $T = 293K$ and at a pressure of $P = 1{,}600\,psi = 11.03MPa$, such that the gas inside the volume will have *1/8* the density of LH_2.

The number of moles, *n*, of gas in the TC can be calculated using the van der Waals[21] equation:

$$\left(P + \frac{a\,n^2}{V^2}\right)(V - n\,b) = n\,R\,T$$

$$\Rightarrow \quad \left(\frac{a\,b}{V^2}\right)n^3 - \left(\frac{a}{V}\right)n^2 + (b\,P + R\,T)n - P\,V = 0$$

where the constants a and b depend on the individual gases critical temperature, pressure, and volume. For our tests, we will be using three gases: H_2, *He*, and N_2, for which these gas constants are:

Gas	a (l^2 atm/mol^2)	b (l/mol)
H_2	0.24440	0.02661
He	0.03412	0.02370
N_2	1.39000	0.03913

Table 1: Gas constants for use with van der Waals equation

In the following table, the van der Waals equation was solved numerically to determine the number of moles of gas. The calculations were made for a volume $V_{TC-Electrode} = 3.26\,l$ which is the total volume in the TC when the electrodes are in place.

T	P	n	m	ρ	Δ IGL

[21] van der Waals equation is used instead of the Ideal Gas Law, since at the highest pressure and lowest temperature, deviations from the Ideal Gas Law of up to 36% are calculated.

	K	*psi*	*atm*	*Pa*	*mol*	*g*	*g/cm^3*	*%*
H_2	293	14.7	1.0	101,325	0.14	0.3	8.38E-05	0.1
	293	1,600.0	108.8	11,024,160	13.64	27.5	8.43E-03	8.3
	77	14.7	1.0	101,325	0.52	1.0	3.20E-04	0.2
	77	1,600.0	108.8	11,024,160	50.84	102.5	3.14E-02	10.5
He	293	14.7	1.0	101,325	0.14	0.5	1.66E-04	0.1
	293	1,600.0	108.8	11,024,160	13.40	53.6	1.64E-02	10.2
	77	14.7	1.0	101,325	0.52	2.1	6.31E-04	0.3
	77	1,600.0	108.8	11,024,160	41.26	165.0	5.06E-02	36.2
N_2	293	14.7	1.0	101,325	0.14	3.8	1.17E-03	0.1
	293	1,600.0	108.8	11,024,160	12.94	362.4	1.11E-01	14.1
	270	14.7	1.0	101,325	0.15	4.1	1.27E-03	0.1
	270	1,600.0	108.8	11,024,160	13.93	390.1	1.20E-01	15.0

Table 2: Calculated number of moles, total mass, and density of gases used under possible operating conditions in the MTA. The last column shows the percentage deviation from the Ideal Gas Law; i.e. the positive change shows that van der Waals equation predicts higher density gas than does the Ideal Gas Law.

In addition to pressurizing the TC with H_2 gas, RF power from a klystron will be fed into the TC via a coaxial line. The test setup and gas schematic are shown in Fig. 5.

Tests to be Performed

A series of tests are scheduled for the TC in the MTA:

1. Study material breakdown of the electrodes in high density H_2 gas for materials: Be, Mo, Cr, vs. Cu at *T=293 K*.
2. Study TC performance inside a solenoidal magnetic field
3. Repeat step 1. and for *T=77 K* (or *T=270 K* for N_2)
4. Test TC operation with beam
5. Repeat steps 1. and 2. with beam at *T=77 K* (or *T=270 K* for N_2)

All of these tests may be performed with the three different gases at the different pressures and temperatures.

This engineering only covers test 3 for operation at *T=77 K* with H_2 gas.

Safety Issues to be Addressed

Using a high pressure, flammable gas volume with high power RF leads to the following safety issues:

1. Pressure Vessel: Risk of explosion and Venting
2. Flammable Gas
3. Oxygen Deficiency
4. Electrical Power

"Chapter 2: Stress Analysis of High-Pressure Test Vessel" addresses the issues of using high pressure gas in the TC. "Chapter 3: Note of Flow Rates of Compressible Gases through Pipes and Valves" shows the calculations of flow rates through the setup as shown in Fig. 5. Three failure scenarios are discussed. "Chapter 4: Additional Test Cell Venting Requirements" addresses possible heating of the gas from the RF in case of failure of the klystron safety system.
"Chapter 5: Flammable Gas Analysis for the High-Pressure RF Test Cell Setup at the MTA" addresses safety issues regarding use of gaseous H_2. Chapter 6 addresses as ODH issues. Finally, "Chapter 7: TC Operation Procedures" gives a check list for safe operation of the TC at the MTA.

Figure 2: Picture of the Mark II Stainless Steel Disks and Cylinder before copper plating. Compared to the first test cell, the thickness of the disks has been increased from one to two inches, the cylinder has been changed from copper to stainless steel and made thicker, and the bolt diameter has been increased from *7/16in* to *5/8in*. The RF/Pressure seals have been changed from Pb-Sn solder rings in grooves to flat Al gaskets.

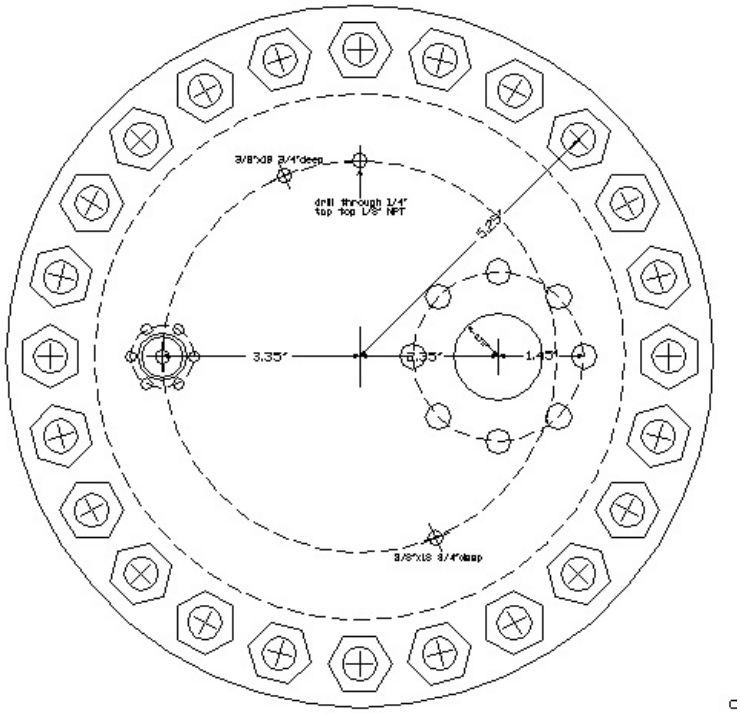

Figure 3: Test Cell Top Plate Schematic

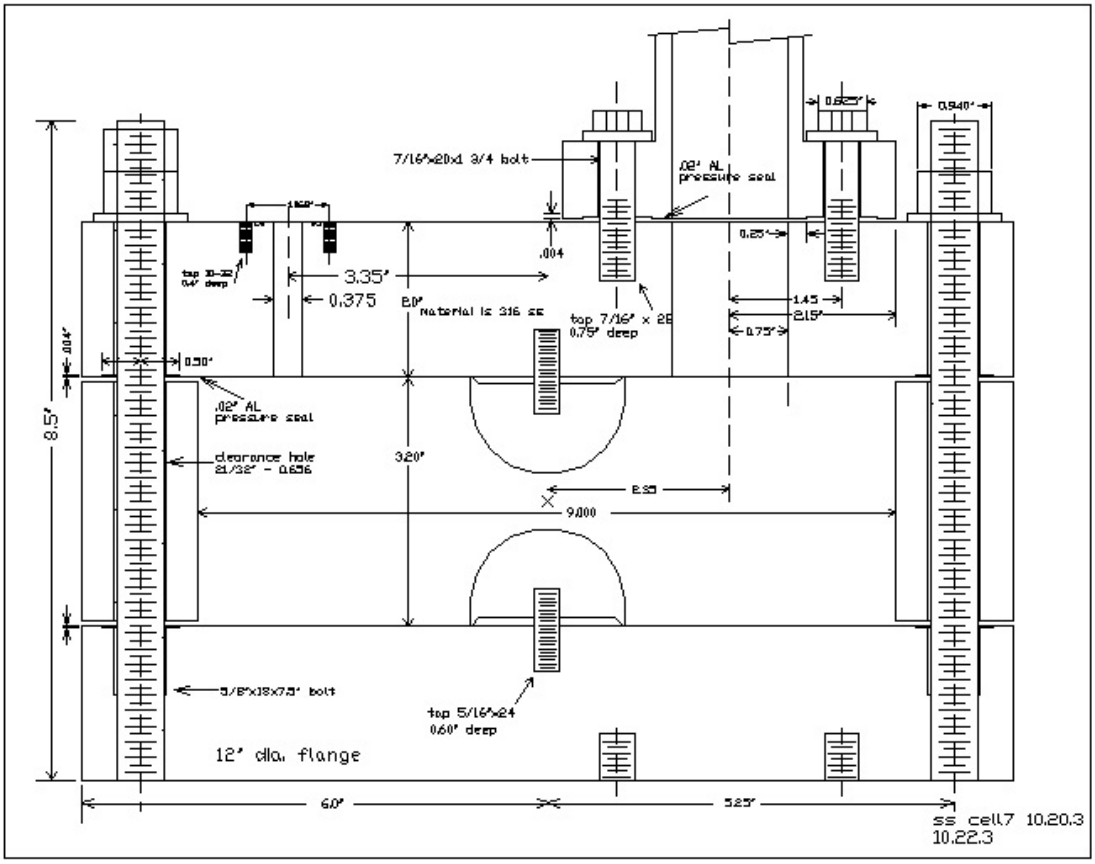

Figure 4: Test Cell Schematic

TC Test Setup and Gas Schematic

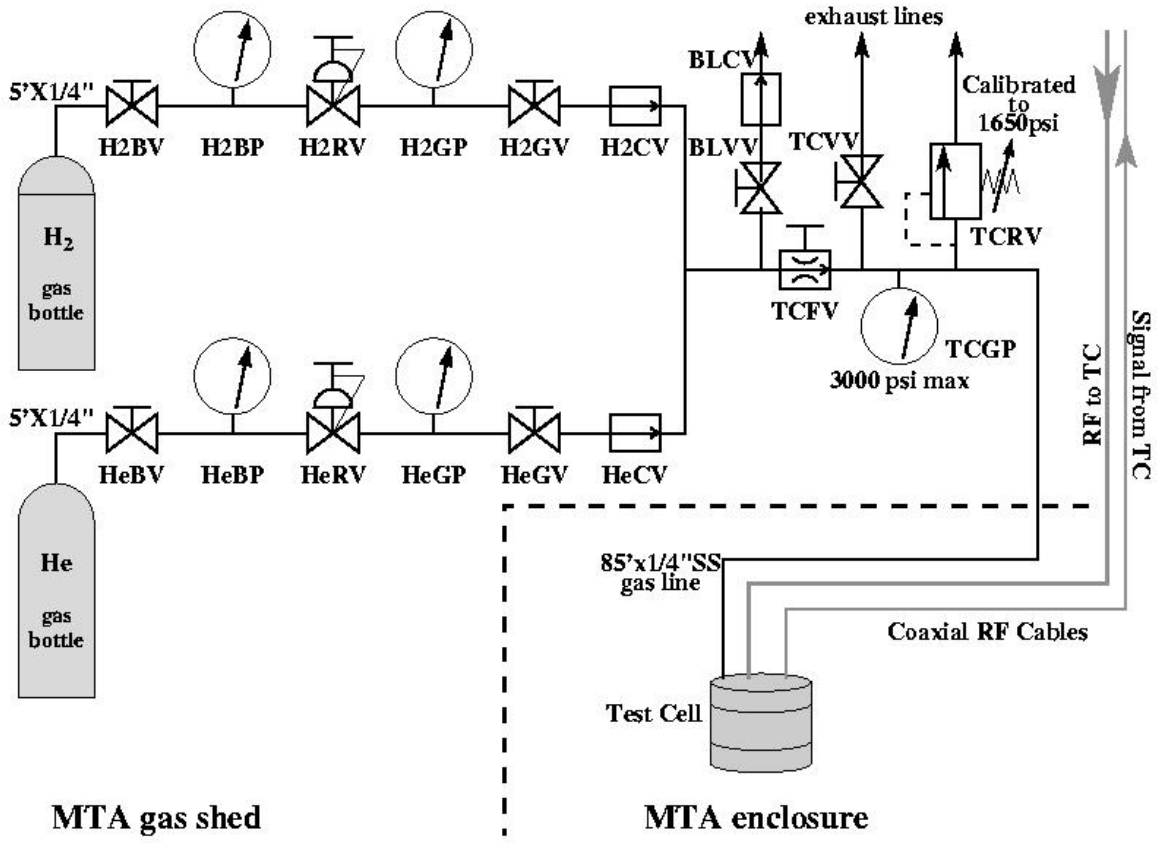

Figure 5: MTA High-Pressure Test Cell test schematic

There are twelve manual valves or regulators:

H2BV – **H**ydrogen-**2** **B**ottle **V**alve
H2RV – **H**ydrogen-**2** **R**egulator **V**alve
H2GV – **H**ydrogen-**2** **G**as **V**alve
H2CV – **H**ydrogen-**2** **C**heck **V**alve
HeBV – **He**lium purge **B**ottle **V**alve
HeRV – **He**lium purge **R**egulator **V**alve
HeGV – **He**lium purge **G**as **V**alve
HeCV – **He**lium purge **C**heck **V**alve
TCFV – **T**est **C**ell **F**ill **V**alve (needle valve)
TCVV – **T**est **C**ell **V**ent **V**alve
BLVV – **B**ottle **L**ine **V**ent **V**alve
BLCV – **B**ottle **L**ine **C**heck **V**alve

There are five pressure gauges:

H2BP – **H**ydrogen-**2** **B**ottle **P**ressure
H2GP – **H**ydrogen-**2** **G**as **P**ressure
HeBP – Helium purge **B**ottle **P**ressure
HeGP – Helium purge **G**as **P**ressure
TCGP – **T**est **C**ell **G**as **P**ressure

An expanded view of the gas manifold, showing the fittings and approximate stainless steel tube lengths, is shown in Fig 6. All tubing is ASTM A213/A269 *¼ in* or *3/8 in* stainless steel with *0.035 in* or *0.049 in* wall thickness. All fittings are rated for the required pressure. To exhaust to outdoors, the *3/8 in* tubing joins to a *1 in* Cu tube manifold. The gas bottles and the gas manifold are mounted inside the MTA gas shed.

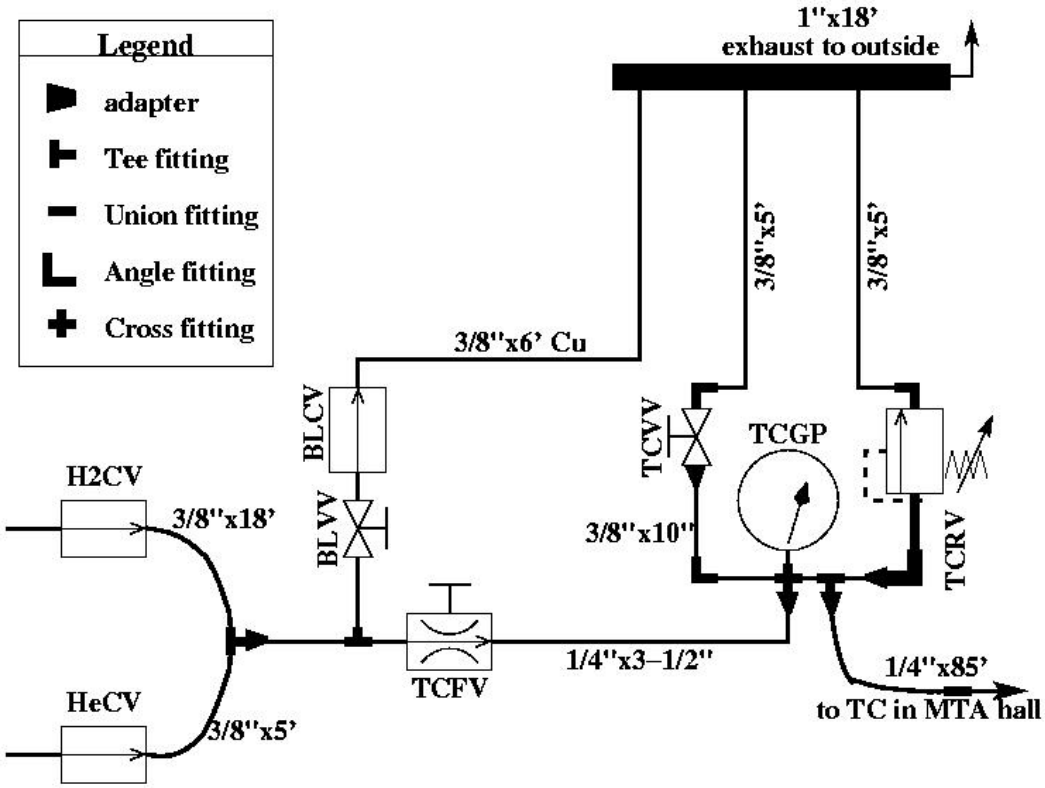

Figure 6: Blow up of gas manifold in gas shed

An independent hydrostatic pressure test was performed on the manifold at 50% over MAWP, or *2,400 psi*, and passed.

MSG-EAR-03-324
September 9, 2003
Revised July 27, 2004
Revised April 13, 2004

Stress Analysis of High-Pressure Test Vessel

BobWands

Introduction and Summary

The ASME Boiler and Pressure Vessel Code, Section VIII, Div. I, is used to verify the design of a 2700 psi test vessel.

The Code calculations show that the required cylindrical shell thickness is 0.794 in; the actual minimum shell thickness is 0.875 inches. The calculations also show that the required flat circular head thickness is 1.99 inches; the actual head thickness is 2 inches. The 1.5 inch diameter penetration in one head is shown to require no additional reinforcement, other than that inherent in the 2 inch thick head. The same is true of the blind holes used to bolt the pipe flanges to the head.

A 3-d finite element model was created to check the Code calculations, and to look at stresses associated with support. (The vessel, without the 1.5 inch diameter pipes, weighs approximately 175 lbs). The stresses in the center of the flat heads do not exceed 17000 psi; the hoop stresses in the cylindrical shell do not exceed 10000 psi. These maximum stresses are less the allowable stress for SS316 steel of 18,800 psi.

This analysis does not address the piping and flanges that bolt to the heads, except as they affect the vessel stresses through their support function. The analysis shows that the contribution of support reactions to the head stress is negligible.

Cylindrical Shell

From the ASME Boiler and Pressure Vessel Code, Section VIII, Div. 1, UG-27, the thickness of a cylindrical shell under internal pressure must be no less than

$$t = PR/(SE-0.6P)$$

where t = thickness of shell
R = inside radius of shell = 4.5 in
P = internal pressure = 2700 psi
S = allowable stress = 18,800 psi (SA-249 welded SS316 tube, per Div. II Part D)
E = weld efficiency = 1 (welded tube allowable stress is used)

Substituting,

$$t = 2700(4.5)/(18800(1)-0.6(2700)) = 0.707 \text{ in.}$$

The shell is perforated by 24 5/8 inch bolts. Although its maximum thickness is 1.5 inches, its minimum thickness (in a plane through a bolt hole) is only 0.875 inches. This is still larger than the minimum requirement of 0.707 inches. Therefore, the shell meets Div. I criterion.

Flat Head

From Section VIII, Div.1, UG-34(c)(2), Formula (1), the minimum required thickness of flat unstayed circular heads must be no less than

$$t = d(CP/SE + 1.9Wh_g/SEd^3)^{1/2}$$

where t = thickness of flat head
C = factor for attachment = 0.25 (from Fig. UG-34(p))
P = pressure = 2700 psi
S = allowable stress = 18,800 psi (SA-240 SS316 plate, per Div. II Part D)
E = weld efficiency = 1 (no welds)
d = diameter of head = 10.5 in (from Fig. UG-34(p))
W = total bolt load (calculated by Appendix 2; unneeded since $h_g = 0$)
h_g = gasket moment arm = 0 (gasket symmetric about bolt)

Substituting,

$$t = 10.5(0.25(2700)/18800)^{1/2}$$

$$t = 1.99 \text{ in.}$$

Actual flat head thickness = 2.0 inches. Therefore, the head meets Div. I criterion.

Reinforcement of Penetrations

There is a single 1.5 inch diameter penetration through one of the 2.0 inch thick heads where a ½ inch thick flange is bolted to connect a stainless steel pipe. From UG-36(c)(3)(a), openings less than 2.375 inches in diameter in shells or heads greater than 0.375 inches thick require no reinforcement other than that inherent in the design.

No reinforcement is required for the 1.5 in. penetration, or for the blind bolt holes used to fasten the pipe flanges to the head.

Finite Element Model

The Code calculations are based on thin shell/plate theory; the test vessel components are relatively thick, and their actual stresses are not well predicted by the Code equations. A 3-D finite element model (Fig. 7) was created to verify the design. Bolt preload was applied such that the bolts reached a stress of 90% yield, or 67.5 ksi. This bolt load produces a total force of about 500,000 lbs, and a compressive stress on the gasket surface of over 10,000 psi.

An internal pressure of 2700 psi was applied to the model.

Seven inches of piping were attached to each head and constrained at the ends to simulate the dead weight support. This length is arbitrary; the actual pipe length may be more or less than assumed here. In any case, the analysis shows that the dead weight support is not a critical contributor to the vessel stresses.

Fig. 8 shows the deformed shape of the vessel. The deflection of the 2 inch thick flat heads is less than 0.00225 inch at the center. For the support system assumed, the entire vessel will sag downward by about 0.006 inches.

Figures 9-11 show stresses along three lines through the critical sections. All stresses are less than predicted by the Code calculations, and less than the 18,800 psi allowable for SS316.

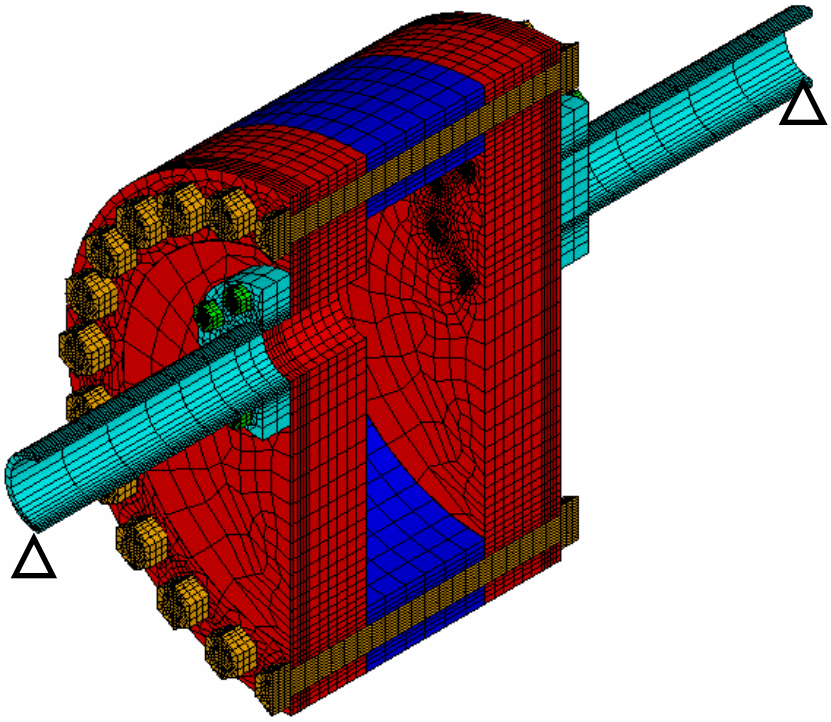

Figure 7: Finite Element Model of Test Vessel

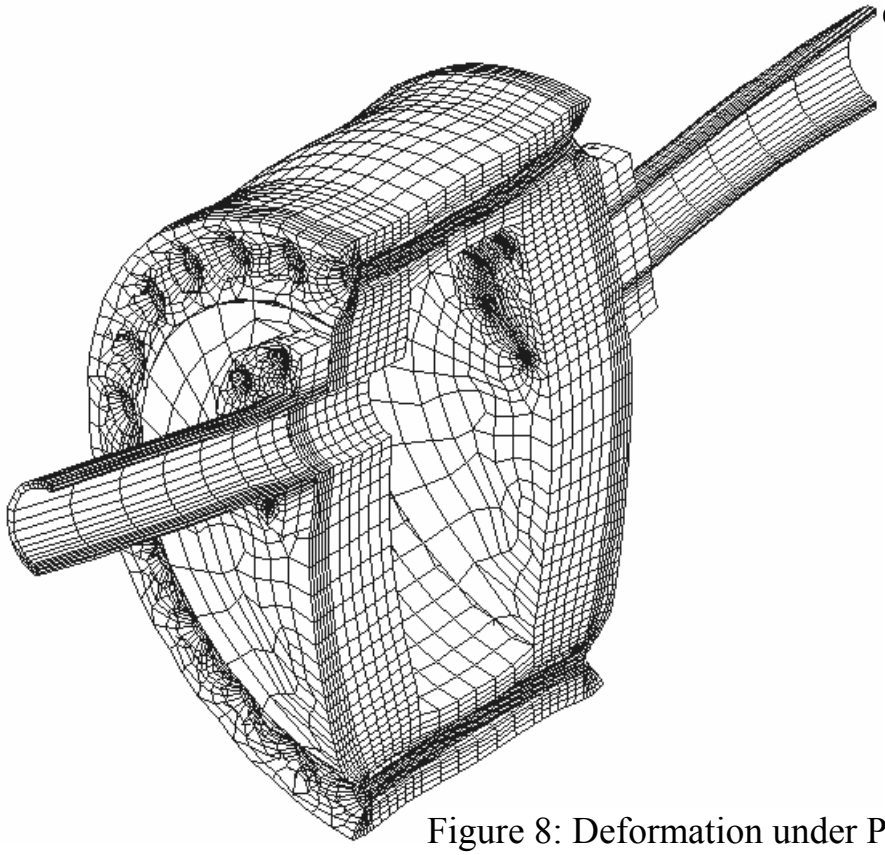

Figure 8: Deformation under Pressure and 1oads

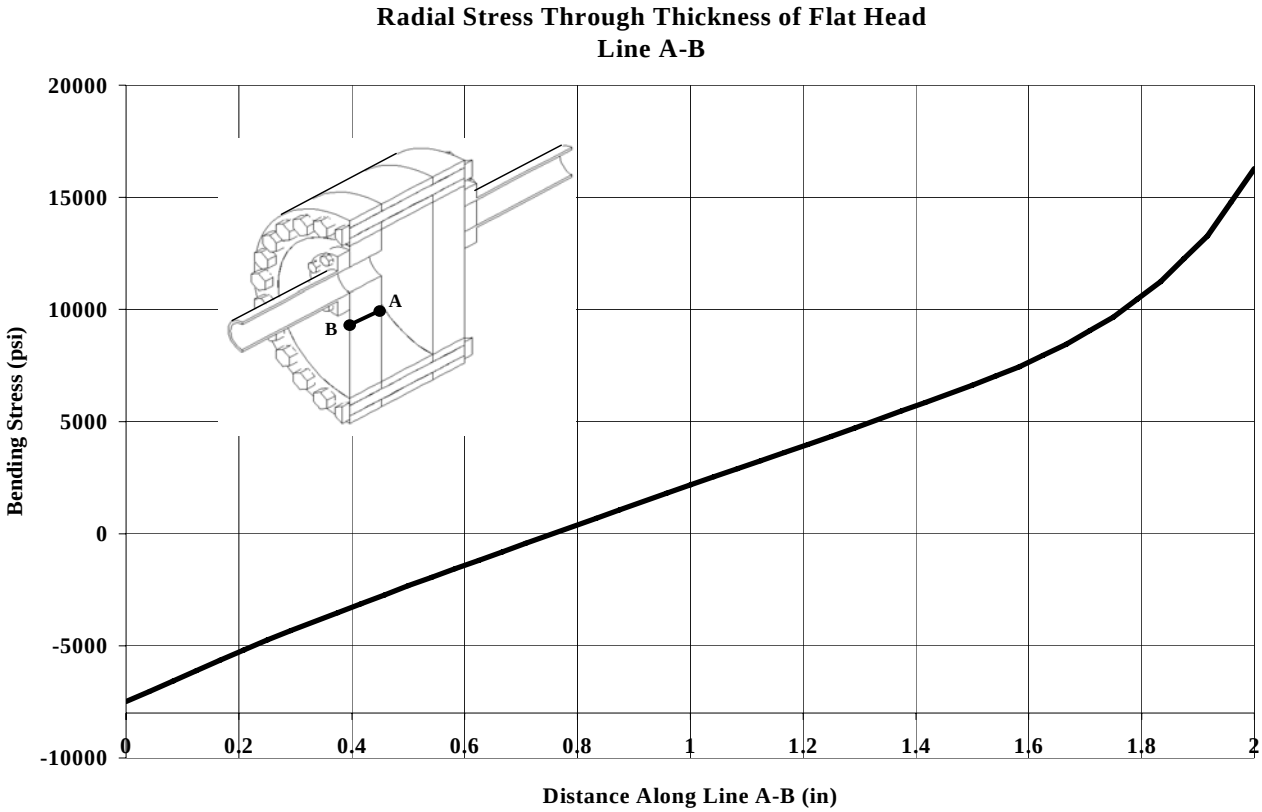

Figure 9: Finite element analysis for f lat heads.

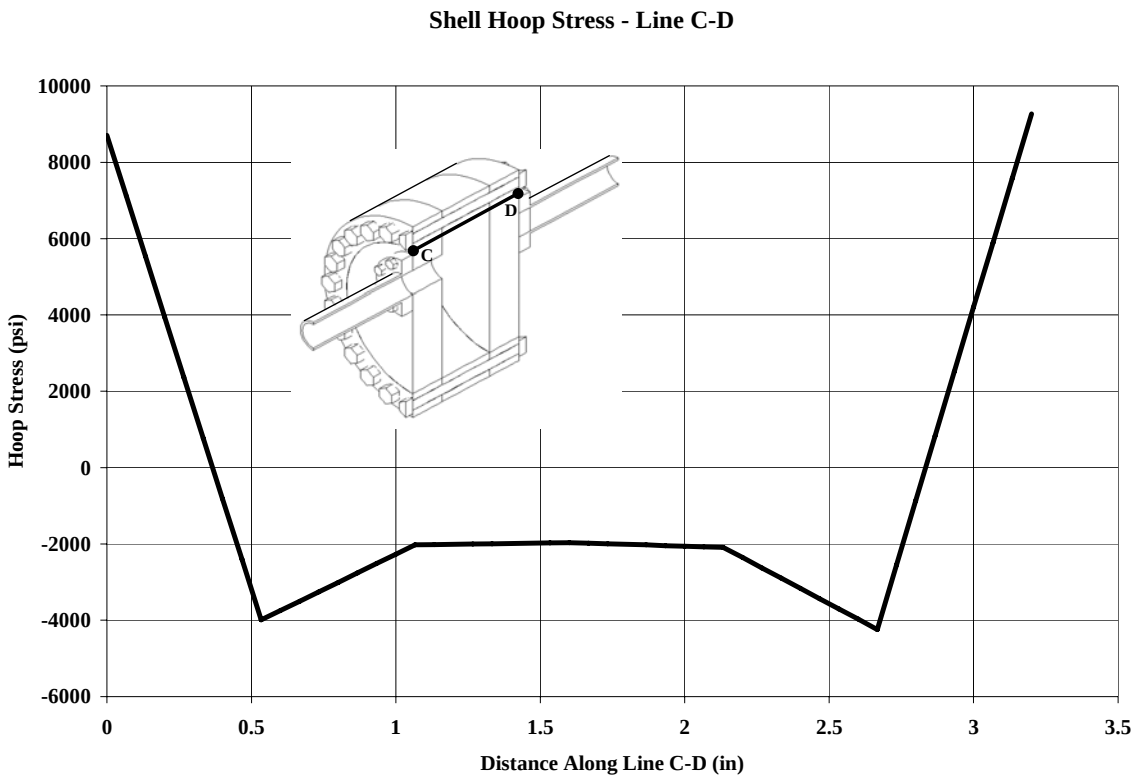

Figure 10: Finite element analysis for interior shell hoop

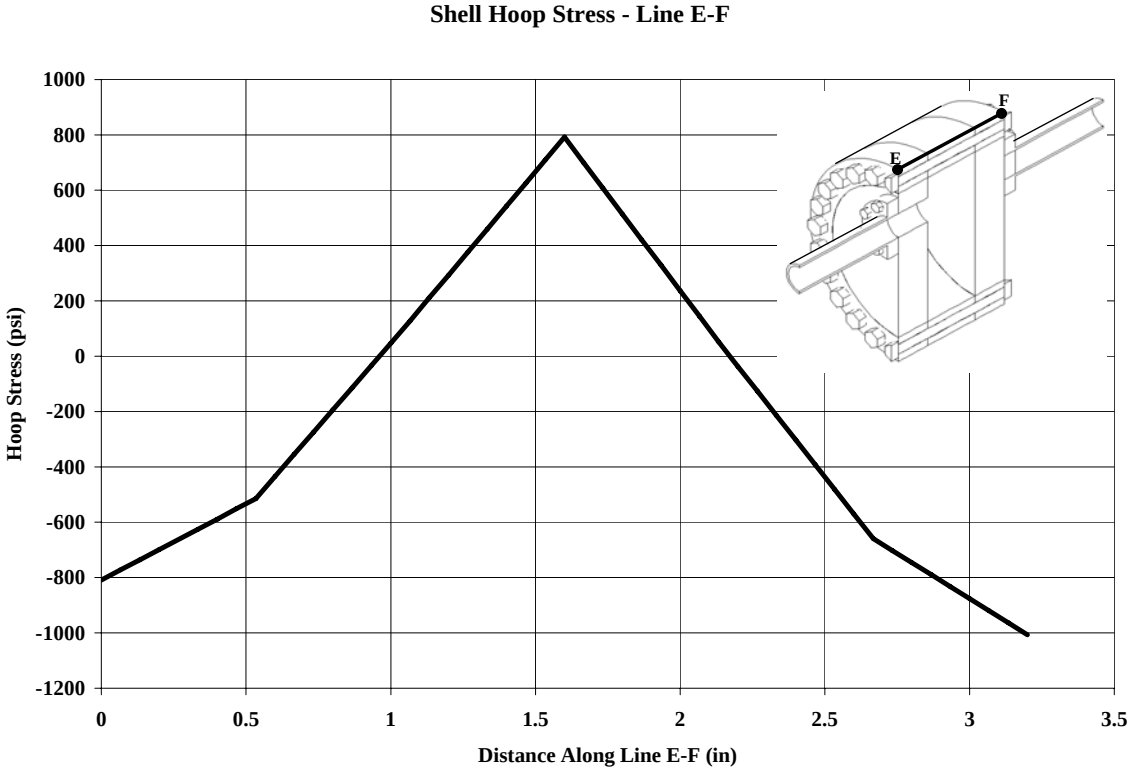

Figure 11: Finite element analysis for exterior shell hoop

Conclusion

This analysis verifies with both ASME Code calculations and a finite element model that stresses in the test vessel are well within the limits imposed by the ASME Code for SS316 stainless steel.

This analysis is confined to the test vessel proper, and does not cover the piping and pipe flanges which bolt to the vessel, except as they affect the vessel in their support function. No high stresses were observed in these regions, but further work should be addressed toward assuring that the piping and flanges are adequately sized for 2700 psi.

As relates to the vessel proper, the concept of support using the pipes bolted to the heads is sound; the vessel weight of 175 lbs produces additional stresses in the head of less than 100 psi, negligible compared with the pressure stresses.

Flow Rates of Compressible Gases through Pipes and Valves

This note follows the procedures in "FLOW OF FLUIDS THROUGH VALVES, FITTINGS, AND PIPE, Technical Paper No. 410", Crane Co. www.cranevalve.com. In what follows, we determine the limiting flow rates for the gas system shown Figs. 5 and 6. We have either *0.25 in* or *0.375 in* stainless steel tubing with *0.049 in* wall thickness, ASTM SA213/A269/A511. The TC fill valve, TCFV, is a Swagelok SS-4MA metering valve with a maximum flow for: H_2 of *78.8 scfm*, *He* of *56.3 scfm*, and for N_2 of *21.2 scfm*.

The form of Darcy's equation to be used is expressed as:

$$q'_m = 412\,\frac{Y\,d^2}{S_g}\sqrt{\frac{\Delta P\,\rho_{\text{int}}}{\kappa}}$$

where:

q'_m is the rate of flow in cubic feet per minute at standard conditions (*14.7 psia* and $60^\circ F$)

Y is the unit-less net expansion factor for compressible flow through orifices or pipes

S_g is the specific gravity of a gas relative to air, or the ratio of molecular weights

$d_1 = 0.152\ in$ is the internal diameter of the *0.25 in* tubing in inches

$d_2 = 0.277\ in$ is the internal diameter of the *0.375 in* tubing in inches

$\Delta P = P_{\text{int}} - P_{ext}$ is the difference in gauge pressures, *psig*, from internal to external

ρ_{int} is the gas density internal to the tubing

$\kappa = f\left(L/D\right) + 1$ is the unit-less resistance coefficient,

where: $f = 0.033$ is the friction factor[22], unit-less (from graph on A-25)

$D_1 = 0.013\,ft$ is the internal diameter in feet of *0.25 in* tubing

$D_2 = 0.023\,ft$ is the internal diameter in feet of *0.375 in* tubing

L is the length of pipe in feet

+1 is the contribution from the exit of the pipe

We consider different scenarios in which operation of the relief valve may be required to ensure a MAWP of *1,600 psi*, and that nothing in the system restricts flow to or from the relief valve. Using Darcy's equation above, we calculate the flow rates for: 1) ensuring that the exhaust system will not limit the flow from the relief valve, 2) overpressure in the TC will be able to flow unrestricted to the relief valve, and 3) a failure in the manifold, when the TC is up to operating pressure, will allow unrestricted flow to the relief valve. For these cases, from Fig. 6, we have the following corresponding lengths of tubing and resistance coefficients: 1) a *0.375 in* section from the relief valve to the *1 in* copper exhaust manifold of length $L_1 = 5\,ft$ and $\kappa_1 = 8.2$, 2) a *0.25 in* tube from the manifold to the TC of length $L_2 = 85\,ft$ and $\kappa_2 = 216.8$, and 3) a $L_3 = 1\,ft$ section of *0.25 in* tubing from the fill valve to the relief valve with $\kappa_3 = 3.5$. Note that there are no contributions considered from the fittings in the system. Using the data from the Cranes Technical Paper No. 410, Fig. 12 shows a curve from which can be determined if flow in the tubing can be considered sonic.

[22] The friction factor, *f*, is based on stainless steel pipe and not stainless steel tubing.

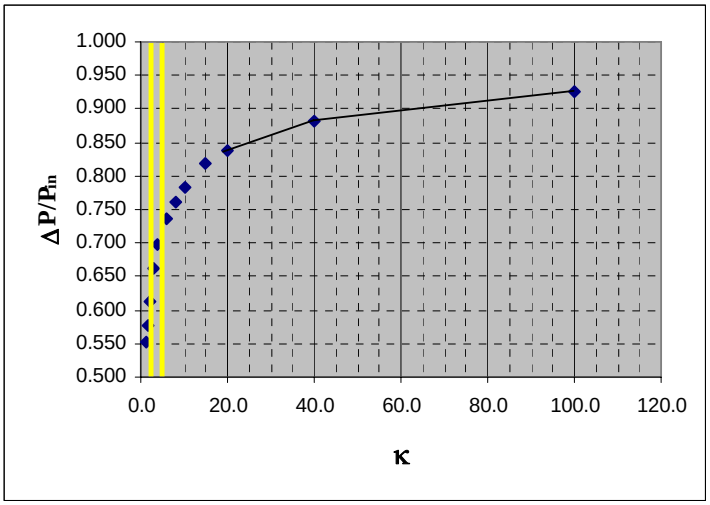

Figure 11: Data points are from Crane Co. Technical Paper No.410. The lines between the last two data points are only to guide the eye. The vertical bars are the resistance coefficients, κ, computed for our purpose. Points above the curve indicate sonic flow.

Case number 1:

Determine the initial flow rate in the vent line from the open relief valve through a *5 ft* tube to the exhaust pipe which leads to the outside of the MTA building.

From Fig. 6, one sees that the exhaust tube from the relief valve feeds into a *1 in* copper pipe. For the purpose of this analysis, it is assumed that the *1 in* pipe will not significantly restrict flow, as its cross sectional area is more than times a *0.375 in* tube, and is therefore ignored.

Here we have the internal gas pressure is $P_{\text{int}} = 1{,}600\,psi$, and it is venting to the outside which is at $P_{ext} = 14.7\,psi$. Then:

$$\Delta P / P_{\text{int}} = \frac{P_{\text{int}} - P_{ext}}{P_{\text{int}}} = 0.99 .$$

Since our value of $\Delta P/P_{int}$ lies above the curve, the velocity is considered sonic. According to the Crane technical paper, for sonic flow, the values at which κ crosses the curve are the de-rating factors for ΔP. Furthermore, the expansion factor assumes its maximum value $Y = 0.71$. For a *5ft* pipe, $\kappa_1 = 8.2$, such that the de-rating factor – from the graph above – is 0.725. Then, $\Delta P = 0.725 \times 1{,}600\,psi = 1{,}160\,psi$. Using the computed values for density from Table 2, and substituting these values into:

$$q'_m = 412\,\frac{Y\,d^2}{S_g}\sqrt{\frac{\Delta P\,\rho_{\text{int}}}{\kappa}} = 412 \times \frac{(0.71)(0.277in)^2}{S_g}\sqrt{\frac{(1160\,psi)\rho_{\text{int}}}{8.2}}$$

we have the following table:

	S_g	ρ_{int} (lbs/ft^3)	q'_m (ft^3/min)
H_2	0.066	0.53	2,944.6
He	0.130	1.02	2,073.9

N_2	0.918	6.93	965.5

Table 3: Calculated flow rates of gases at *P=1,600 psi* and room temperature through a *5 ft* pipe

Case number 2:
Determine the initial flow rate between the TC at *1,760 psi* and the relief valve at *1,650 psi*.

This is the case where the relief valve has opened, but its spring reseats the valve so as to keep the pressure at *1,600 psi*. The pipe between the TC and the relief valve is *85 ft* and $\kappa_2 = 216.8$.
Then

$$\Delta P = 1{,}760\,psi - 1{,}650\,psi = 110\,psi$$

and

$$\Delta P / P_{\text{int}} = \frac{1{,}760\,psi - 1{,}650\,psi}{1{,}760\,psi} = 0.06$$

Here we do *not* have sonic flow, such that from the graph on A-22, one has $Y = 0.97$. The rate of flow is:

$$q'_m = 412\,\frac{Y\,d^2}{S_g}\sqrt{\frac{\Delta P\,\rho_{\text{int}}}{\kappa}} = 412 \times \frac{(0.97)(0.152in)^2}{S_g}\sqrt{\frac{(110\,psi)\rho_{\text{int}}}{216.8}}$$

such that

	S_g	ρ_{int} (lbs/ft^3)	q'_m (ft^3/min)
H_2	0.066	0.53	72.6
He	0.130	1.02	51.1
N_2	0.918	6.93	18.9

Table 4: Calculated flow rates of gases at *P=1,760 psi* and room temperature through an *85 ft* pipe

Note that the density of the gas, ρ_{int}, will be slightly higher at P_{int}=*1,760 psi.* However, as these flow rates are greater then an order of magnitude above the required flow rate of *2.5 scfm (see Chapter 4)*, these estimates are more than adequate.

Case number 3:
Determine the maximum flow rate to the relief valve from the gas bottle should the regulator valves and fill valves fail when the TC is already up to a maximum pressure of *1,600psi*.

In this scenario, we want to avoid the full *2,000 psi* from the gas bottle being forced into the TC which is only rated for *1,600 psi*. Here we have the same line from the TCFV to and from the TC, so we only need to be concerned with the flow from the TCFV through the relief valve, TCRV, to the exhaust. Note that there is actually a combination of *0.25 in* tubing and *0.375 in* tubing; here we use the more limiting case of *0.25 in* tubing.

So

$$\Delta P = 2{,}000\,psi - 1{,}600\,psi = 400\,psi$$

and

$$\Delta P \big/ P_{\text{int}} = \frac{2{,}000\,psi - 1{,}600\,psi}{2{,}000\,psi} = 0.20$$

Here we do *not* have sonic flow, such that from the graph on A-22, one has $Y = 0.93$. The rate of flow is:

$$q'_m = 412\,\frac{Y\,d^2}{S_g}\sqrt{\frac{\Delta P\,\rho_{\text{int}}}{\kappa}} = 412 \times \frac{(0.93)(0.152in)^2}{S_g}\sqrt{\frac{(400\,psi)\rho_{\text{int}}}{3.5}}$$

such that

	S_g	ρ_{int} (lbs/ft^3)	q'_m (ft^3/min)
H_2	0.066	0.53	1,043.9
He	0.130	1.02	735.2
N_2	0.918	6.93	271.4

Table 5: Calculated flow rates of gases at *P=2,000 psi* and room temperature through a *20 ft* pipe

Again, note that the density of the gas, ρ_{int}, will be higher at P_{int}=*2,000 psi*. However, as these flow rates are greater then two orders of magnitude above the required flow rate of *2.5 scfm (see Chapter 4)*, these estimates are more than adequate.

Summary

For all cases listed above, the flow rates are more than an order of magnitude above the required flow rate of *2.5 scfm*. Furthermore, all of these rates are greater than the flow rate of *125 cfm* of the relief valve, TCRV, thus not limiting the capability of the relief valve.

Additional Test Cell Venting Requirements

Pressure Relief Required by RF Heating

The *12 MW* klystron runs at *1 Hz* to *15 Hz*. Each pulse could be as long as *100 μs*, implying a maximum average klystron power of $12\,MW \times 100\,\mu s \times 15\,Hz = 18\,kW$. However, for our tests, we will have an adjustable peak power between *100 kW* and *1.5 MW* in *60 μs* pulses. Thus the maximum power to the TC will be between $100\,kW \times 60\,\mu s \times 1\,Hz = 6\,W$ and $1.5\,MW \times 60\,\mu s \times 15\,Hz = 1.35\,kW$.

Normally, this power is dissipated in the walls of the test cell. The mass and heat capacity of the TC requires *33.6 kJ* of energy to raise the temperature of the walls by *1 K*.

A spark across the electrodes causes the TC to detune. In this condition, the **RF cannot be fed into the cavity** and almost the entire incident wave is reflected back toward the klystron. The reflected wave is detected and used to turn off the klystron. A variable delay, currently about 8 seconds, inhibits the klystron from pulsing, allowing the TC to recover. **Thus the gas in the TC is inhibited from receiving significant direct heating by the process itself, since electrical conduction in the gas detunes the cavity, and by the electronic circuit that inhibits klystron operation into a detuned cavity.**

Nevertheless, we were asked the question "if all of the power of the klystron went into heating the gas, how fast would the pressure rise?" In what follows, we calculate the temperature rise assuming the full *1.35 kW* of input and the volume of gas that would need to be exhausted to accommodate this rise in temperature and still remain at the desired pressure. **From Table 7 below, we see that for both H_2 and *He* this is less than *0.4 scfm.***

The Anderson Greenwood 81MS44-4 relief valve is rated to carry *125 cfm*.

As shown in Table 4 of the previous section, the *85 ft* long, *¼ in* diameter pipe between the test cell at 10% over *1,600 psi* and the relief valve at $60^\circ F$ will carry H_2 at *73 scfm* and *He* at *51 scfm*. As this is the limiting case for flow from the TC to outside the MTA, one clearly sees that the limit is set by the relief valve, and this is still two orders of magnitude above the required relief of *2.5 scfm*.

We conclude that nothing inhibits the required flow of *2.5scfm* to relieve the pressure caused by some mechanism to directly heat the gas in the TC.

RF Heating

The amount of heat, *dQ*, needed to increase the temperature by *dT* of *n* moles of gas with specific heat *C* is given by:

$$dQ = nC_V dT ,$$

where *Q* is in Watts, and for our purpose *C* is the specific heat at constant volume, C_V, and is in Joules/mole/Kelvin. The specific heat is a function of temperature and pressure, and is given in the table below for the appropriate settings of *P* and *T*. Also, the number of moles, *n*, is calculated in Table 2.

From the above specific heat equation, one can determine the change in temperature of *n* moles of gas:

$$dT = \frac{dQ}{nC_V}$$

Also, differentiating van der Waals equation with respect to time, with volume constant, one has the relationship:

$$dP = \left(\frac{n\,R}{V - n\,b} \right) dT$$

Under the worst case scenario of RF heating, the entire *1.35 kW* of power will be absorbed by the gas in the TC. In one second, this corresponds to *1350 J* of energy. Using the above relationships for the gases of interest, the pressure and temperature changes which might be encountered under the condition that the entire *1350 W* of power will be absorbed by the gas in the TC yields:

	T	***P***		***n***	***C_V***	***ΔT***	***ΔP***	
	K	***psi***	***atm***	***mol***	***J/mol/K***	***K***	***psi***	***atm***
H_2	293	14.7	1.0	0.14	21.59	461.3	23.2	1.58
	293	1,600.0	108.8	13.64	21.75	4.6	25.8	1.76
	77	14.7	1.0	0.52	14.60	178.8	34.4	2.34
	77	1,600.0	108.8	50.84	15.37	1.7	55.5	3.78
He	293	14.7	1.0	0.14	12.46	799.6	40.1	2.73
	293	1,600.0	108.8	13.40	12.54	8.0	44.1	3.00
	77	14.7	1.0	0.52	12.47	210.4	40.2	2.73
	77	1,600.0	108.8	41.26	12.89	2.5	55.3	3.76

Table 6: Calculated change in temperature and pressure, assuming a deposit of 1.35 kW of power in the TC due to a failure in the klystron safety system. The number of moles comes from Table 2. The specific heats are given under the same conditions from published literature.

At high pressure, should the entire *1.35 kW* of power be dumped in the TC, the greatest temperature rise for *H_2(He)* would be *461.3 K(799.6 K)*, respectively, and the greatest pressure

rise for $H_2(He)$ would be *3.78 atm(3.76 atm)*. This temperature and/or pressure rise, is equivalent to an increase in volume, at STP. At STP, the gases under consideration, all act as ideal gases to within 0.1%; hence, the ideal gas law can be used to determine the volume change which would need to be exhausted from the TC:

$$\Delta V = \frac{\Delta n\, R\, T}{P}$$

where the change in the number of moles, Δn, is determined numerically from van der Waals equation, as above. The results are given in Table 7.

	T	***P***		***Δn***	***ΔV***			
	K	***psi***	***atm***	***mol***	***l***	***cm^3***	***in^3***	***ft^3***
H_2	293	1,600.0	108.8	0.067	1.6	1610.9	98.3	0.057
	77	1,600.0	108.8	0.378	9.1	9088.5	554.6	0.321
He	293	1,600.0	108.8	0.112	2.7	2692.9	164.3	0.095
	77	1,600.0	108.8	0.379	9.1	9112.5	556.1	0.322

Table 7: Calculated change in volume at STP. This is the volume of gas which must be exhausted from the TC in order to keep the pressure, and hence density, constant.

As these amounts of gas which would need to be exhausted are far below the flow rates calculated in the preceding section of this document, we conclude that the RF heating of the gas does not pose a hazard.

Flammable Gas Analysis for the High-Pressure RF Test Cell Setup at the MTA

Rolland Johnson
1/25/2003, revised 11/12/03
revised by Pierrick Hanlet, 7 September 2005

This Test Cell is required by Fermilab to conform to the Guidelines for the Design, Testing, Installation, and Operation of LH2 Targets. In addition we have elected to conform to the features of FESHM chapter 6020.3 listed below.

This document describes the Flammable Gas analysis for the high-pressure RF Test Cell (TC) to be used at the MTA for the study of high voltage breakdown of dense hydrogen gas. The TC will operate at liquid N_2 temperature $T=77K$. The TC will be filled using a manifold that allows an operator to:

- pressurize the TC from a gas bottle
- depressurize the TC by venting the gas outside of the MTA gas shed
- purge the TC by alternately pressurizing and then venting the gas.

A schematic of the gas system is shown in Fig. 5. The operation procedures, the checklist for preparations, and the conclusion of operations are given in Chapter 7, below.

In the sections below, the relevant sections of the FESHM manual chapter 6020.3 Rev 8/95 are discussed. The extracts from the FESHM are in normal type and *Analysis and Comments are in italics.*

CLASSIFICATION OF GAS STORAGE AND USAGE FACILITIES

The gas system for our tests is separable; the TC will be operated in the MTA experimental hall, and the H_2 gas source will be kept out doors. Even if the gas were kept inside the MTA experimental hall with the TC, a 250 ft^3 bottle of H_2 has but 594 g of gas; i.e. less than the allowable maximum of 0.6 kg for a Class 0 rating.

Furthermore, the maximum volume of H_2 that would be used in the 4l TC (TC+RF feedthru – Electrode) requires a maximum volume of 374 l = 13.2 scf of gaseous H_2 to operate at P=108.8 atm and at T=77 K. One open bottle of 250 scf is the most that will be needed for several fills and the most that will be allowed in the MTA gas shed at one time. By the rules of FESHM chapter 6020.3 revised, as shown in Figure 1 of that manual using the values for hydrogen shown in Table 2 of this document, the Test Cell and its associated gas storage area are Risk Class 0.

PROCEDURES FOR APPROVAL

1. **Risk Class 0**

The risk analysis shall be reviewed by the Fire Hazard Subcommittee or by an independent reviewer appointed by the Division/Section head. A copy of the independent review shall be sent to the FHS. Approval by the Division/Section head is required before the introduction of flammable gas into a system.

REQUIREMENTS FOR FLAMMABLE GAS INSTALLATIONS

A. Risk Class 0 Installations:

1. The area shall be posted "Danger-Flammable Gases, No Ignition Sources" using standard signs available from the Fermilab ES&H Section, Health and Safety Group. A list of responsible persons with their phone numbers shall also be posted.

The TC will only be filled with hydrogen when it is being actively studied. Two responsible persons will always be in the immediate vicinity of the MTA experimental hall and gas shed when hydrogen is being used. The appropriate signs will be posted. These and other requirements are part of the procedures for preparation and conclusion of hydrogen operation as listed in Hydrogen Operation Checklists (see Chapter 7).

2. Combustibles and ignition sources shall be minimized within three meters of gas handling equipment, piping, or apparatus.

Combustibles will be kept away. The equipment in the MTA will be examined for possible ignition sources and a plan for any needed changes will be developed and implemented before hydrogen is introduced. The electrical components relating to the RF equipment are necessarily well shielded and well grounded.

3. A pressure regulator appropriate for the gas and its environment shall be used.

The regulator is certified for use with hydrogen.

4. An orifice, excess flow valve or other fixed means of limiting the flow to no higher than ten times the maximum operational flow rate shall be installed.

A Swagelok metering valve, model SS-4MA, serves as the TC fill valve, TCFV. For H_2, the maximum flow rate through this valve is 78.8 scfm. The TC is a stainless steel vessel which has no maximum operational flow limits and will not be operated beyond its tolerance, according to Chapter 2, there is no limit on the rate at which we fill the vessel. A flow restriction device, the TCFV, will allow an operator sufficient time to react should a problem arise.

5. All gas cylinders shall be secured. Cylinders not in use shall be capped. Empty cylinders shall be promptly removed.

6. Enclosed volumes containing piping or equipment shall be incapable of becoming pressurized. For example, chest freezers shall not have latching doors. Electrical devices enclosing or enclosed within these volumes shall be listed for use in Class 1, Division 2 locations per NEC article 500 or otherwise be documented and approved as non-sparking devices.

There are no such enclosed volumes in this experiment.

7. Leaks from experimental devices such as drift chambers shall be measured and documented prior to initial operation (with nonflammable gas, if possible). Leakage above seven liters/hour from any one chamber shall be mitigated. Recheck for leaks after major repairs or modifications, and at least every twelve months. Leakage exceeding 20% of the lower explosive limit at a distance over two inches from an identified "point" leak shall be repaired.

*Seven liters/hour is thus ¼ scfh. At 1,600 psi the TC contains 374 l = 13.2 ft^3 at STP. A leak of 7 l/hr would cause the pressure to drop at 0.25scfh * 1,600psi / 11.6 scf = 34.5 psi/hr. The TC pressure gauge, TCGP TP in Fig. 5, is calibrated and a pressure change of 10 psi can be easily seen. Furthermore, the TC resonant frequency is dependent on the dielectric constant of the gas in the chamber; should a leak arise, the density of the gas and therefore its dielectric constant would change and would become apparent at the klystron. Thus in a period of ½ hour of constant conditions (thermal equilibrium at room temperature) it can be verified that there is no leak greater than seven liters/h.*

8. Ventilation above one air change per hour shall be maintained in areas using or storing flammable gas. This may be accomplished by mechanical or natural ventilation. For natural ventilation, a room vent with a minimum of 1/2 square foot free area shall be provided per 1000 cubic feet of room volume.

The MTA enclosure is estimated to be 16,563 ft^3. Should the entire volume of a 250 scf H_2 bottle be exhausted into the MTA experimental hall, it would occupy 1.5% of the total volume of the enclosure. In addition, the MTA experimental hall has constant forced ventilation of 2,000 cfm; this corresponds to approximately 7.25 volume changes per hour.

9. Welding permits shall not be issued for areas within ten meters of the equipment containing flammable gas unless approved in advance by the responsible Division/Section head or designee.

Since the hydrogen gas is only being used when responsible people are nearby, welding activity will not be allowed.

Oxygen Deficiency Hazard Risk Assessment

Pierrick Hanlet, 13 July 2006

From Fig. 5, one sees that the entire inventory of gas used for the experiment comes from two *258 ft³* gas bottles. These bottles will be stored inside of the MTA gas shed as will the gas manifold, and the TC in the MTA experimental hall. There exist three *3 in* penetrations between the gas shed and experimental hall. As the unused space of these penetrations are plugged with flameproof material, ODH considerations are separable and considered independently for the MTA experimental hall and for the MTA gas shed.

The following analysis is based on Fermilab ES&H Manual 5064. ODH classifications are based on the product of an event failure rate and the probability of death for that particular event per hour of operation:

$$\phi = \sum_i P_i F_i$$

where P_i is the probability of occurrence of event *i*, and F_i is the fatality factor for that event. $F_i=0$ when the partial pressure of oxygen remains above 18%, and $F_i=1$ when the partial pressure of oxygen is below 8.8%.

MTA Experimental Hall

The MTA experimental hall has a total volume, including "pre-cast" volume, of $V = 16{,}563\,ft^3 = 468.9\,m^3$. In the hall, a forced ventilation system of *2,000 scfm* operates continuously; this corresponds to 7.25 volume changes per hour.

The normal amount of O_2, in moles, in the hall can be calculated from the ideal gas law:

$$n_{MTA} = \frac{PV}{RT} = \frac{(1\,atm)(469{,}011\,l)}{(0.082\,l\,atm/mol\,K)(293\,K)} = 19{,}507\,mol$$

As the partial pressure of O_2 is 21% of the total gas volume, the amount of O_2 in the hall at STP is $n_{O_2} = 4{,}096\,mol$.

The number of moles of gas in a *258 ft³* bottle (regardless of the gas) is:

$$n_{bottle} = \frac{PV}{RT} = \frac{(1\,atm)(7{,}306\,l)}{(0.082\,l\,atm/mol\,K)(293\,K)} = 304\,mol$$

Under the catastrophic scenario in which an entire *258 ft³* gas bottle is emptied into the hall simultaneously with a failure of the ventilation system, then the partial pressure of O_2 will be:

$$P_{O_2} = \frac{n_{O_2}}{n_{MTA} + n_{bottle}} = \frac{4096\,mol}{19{,}507\,mol + 304\,mol} = 20.7\%$$

This is well above the required 18% O_2 concentration, such that the MTA experimental hall will remain ODH class 0. This does not even consider that both H_2 and *He* gases would not significantly displace the O_2 levels at ground, as both gases are lighter than air and would only occupy the upper layer of the MTA experimental hall.

For the present tests, the TC is cooled to *77 K* by placing it inside of large dewar of LN_2. The dewar is a beer keg cooler of volume $V_{dewar} = 88{,}278\,cm^3$, so that it would require

$V > V_{dewar} - V_{TC} = 88{,}278\,cm^3 - 13{,}344\,cm^3 = 74{,}934\,cm^3 \approx 7.4\,l$ of LN_2 to completely fill the dewar with TC immersed. Assuming that we use *7.4 l* of LN_2, this corresponds to *213 mol* of N_2. Should all of the LN_2 boil off, the amount of gas would be *181 ft³* at STP.

Should the LN_2 boil off simultaneously with a catastrophic leak of H_2 into the MTA, then the partial pressure of O_2 would be

$$P_{O_2} = \frac{n_{O_2}}{n_{MTA} + n_{bottle} + n_{LN_2}} = \frac{4096\,mol}{19{,}507\,mol + 304\,mol + 213\,mol} = 20.5\%$$

This is still well above the required 18% O_2 concentration, such that the MTA experimental hall will remain ODH class 0.

MTA Gas Shed

Since the gas manifold will be located in the gas shed, there is a possibility of creating an ODH environment inside of the shed should a bottle leak at the manifold. This room has a volume $V = 8\,ft \times 8\,ft \times 8\,ft = 512\,ft^3 = 14.5 m^3$, with $2\,ft \times 2\,ft$ louvers for ventilation. In addition, there is a *569 cfm* exhaust fan which will be operating throughout the experiment (see Chapter 7), and a blow-off sky light. Despite these safety features, there is still the possibility that should a gas bottle leak into this volume when the ventilation system fails, the gas would occupy *~50%* of the volume of the shed.

$$n_{shed} = \frac{PV}{RT} = \frac{(1\,atm)(14{,}498\,l)}{(0.082\,l\,atm/mol\,K)(293\,K)} = 603\,mol$$

which corresponds to $n_{O_2} = 127\,mol$ at STP.

Under the catastrophic scenario in which an entire *258 ft³* gas bottle is emptied into the shed simultaneously with a failure of the ventilation system, then the partial pressure of O_2 will be:

$$P_{O_2} = \frac{n_{O_2}}{n_{MTA} + n_{bottle}} = \frac{127\,mol}{603\,mol + 304\,mol} = 14.0\%$$

From the graph on page 5064TA-2, this corresponds to a *fatality factor* $F_i = 1 \times 10^{-4}$. As a leak in the gas system is the only type of ODH event that could occur, this factor will apply all different failures, such that $F=F_i$.

Since the exhaust system guarantees at least one volume change of air per minute, any failure mode which would lead to an ODH event would have to include a failure of the exhaust system.
Therefore, in order to determine the hazard, one must consider a simultaneous double failure mode in which the exhaust system fails at the same time as a leak is developed. The worst case scenario is to have the entire *258 ft³* gas bottle emptied into the shed while there is an unscheduled power outage, or another cause for exhaust fan failure. Thus, the classification equation becomes:

$$\phi = P_{fan} F \sum_i P_i$$

where $P_{fan} = 3 \times 10^{-4} / demand$ is the probability of an exhaust fan failure. The details of the manifold are shown in Fig 6, and can be used to count the fittings and devices which could potentially be a leakage source; there are 25 such fittings. The fittings from the gas bottles are counted to be 22.

Device	Number	Failure Rate *(hr $^{-1}$)*
Tubing (*>5 ft*)	4	1×10^{-9}
Fitting Connections	47	3×10^{-7}
Check Valves	2	1×10^{-8}
Manual Valves	2	1×10^{-8}
Relief Valve	1	1×10^{-5}
Pressure Gauge	1	3×10^{-7}

Table 8: Probability rates for failure of devices listed.

The entries in Table 8 correspond to possible failure events which would cause a gas leak; these sum to 2.4×10^{-5}. So:

$$\phi = P_{fan} F \sum_i P_i = \left(3\times10^{-4}\right)\left(1.0\times10^{-4}\right)\left(2.44\times10^{-5}\right) = 7.32\times10^{-13}$$

According to the Fermilab ES&H Manual 5064, this result classifies the MTA gas shed as a Class 0 ODH environment.

TC Operation Procedure

Two responsible operators are required to be in immediate vicinity of the MTA while hydrogen is being used; one will be in the Linac Gallery and one will be adjusting the pressure in the TC. As the MTA experimental hall will be interlocked during running with RF, any access will be made as a *controlled access*, and the pressure in the TC will be reduced to $P \leq 1{,}000\ psi$, *½ the test pressure or 63% of MAWP*, prior to any access.

Tests will be made by ramping the TC pressure between atmospheric pressure and *1,600 psi*. At each pressure, the RF frequency will be adjusted to find the resonant frequency of the cavity; thereby allowing maximum power into the TC. Afterwards, the RF power will be ramped until breakdown occurs. Several measurements will be performed for each of the electrodes under investigation. We do not expect to need to enter the MTA experimental hall except to refill the LN_2 dewar, or to change the electrodes, which would require that the TC be completely vented using the procedures below.

Hydrogen Operation Checklists

Before Operation with Hydrogen:

1. Post Signs at the *hydrogen gate* entrance to the MTA experimental hall and at the MTA gas shed. The signs must say "Danger-Flammable Gases, No Ignition Sources" using standard signs available from the Fermilab ES&H Section, Health and Safety Group. Post a list of responsible persons with their phone numbers near the Gas Manifold.

2. Check for combustibles or ignition sources within 3 meters of the TC and 3 meters from the Gas Manifold. Remove combustibles and disable or remove ignition sources. LOTO ckts. 25 and 50-52-54.

3. Verify the condition of the gas system noting that the approved hydrogen regulator is functioning properly.

4. Verify that gas cylinders are secured and that cylinders not in use are capped. Remove empty cylinders.

5. Verify that the blower system is operating in the MTA experimental enclosure.

6. Verify that the blower system is operating in the MTA gas shed.

7. Check O_2 levels in MTA experimental hall and MTA gas shed; there are 2 readings for each.

8. Check H_2 levels in MTA gas shed.

9. On the first purge cycle, verify that the TC maintains pressure for ½ hour to ensure that there are no leaks.

10. Verify the correct operation of the TCFV needle valve.

Test Procedure for Normal Operation:

1. Verify seven manual valves are closed:
   H2BV, **H2RV**, **H2GV**, **HeBV**, **HeRV**, **HeGV**, **TCVV**.
   The **TCFV** should be set once and not touched afterwards.

2. Purge the TC with *He* to reduce residual H_2, N_2, and O_2 levels:
   Open **HeBV** and **TCFV**. Use **HeRV** to set **HeGP** to *500 psi*.
   Open **HeGV**. Use **HeGV** to raise **TCGP** > 4*50 psi*.
   Close **HeGV**. Verify **TCGP** is steady, signifying no leaks.
   Use **TCVV** to lower **TCGP** to *~0 psi*. Close **TCVV**.
   Close **HeBV** and **HeGV**.
   Repeat Step 2 if the TC has been open to air.

3. Purge the TC with H_2 to reduce residual *He* levels:
   Open **H2BV**. Use **H2RV** to set **H2GP** to *1,600 psi*.
   Open **H2GV**. Use **H2GV** to raise **TCGP** to *1,600 psi*.
   Close **H2GV**. Verify **TCGP** is steady.
   Use **TCVV** to lower **TCGP** to *~0 psi*. Close **TCVV**.

4. For measurements of RF breakdown, the TC must be filled with H_2 and remain in a static condition for several minutes to make sure the gas temperature has come to thermal equilibrium with the TC. Subsequent measurements at lower pressure are made by venting gas from the TC using the **TCVV** and monitoring **TCGP**.

Do not leave the manifold unless HeGV and H2GV are closed.

5. When finished, close **H2GV** and **H2RV**, and repeat step 2 to purge with *He*. Use checklist below.

After Operation with Hydrogen:

1. Complete the Operation Procedure, ending with the purge to *He* gas to *0 psi* as shown in step 2 and with all valves closed.

2. Verify that gas cylinders are secured and that cylinders not in use are capped. Remove empty cylinders.

3. Remove the Danger signs from the MTA entrances. Leave the list of responsible persons posted near the Gas Manifold.

To Change a Hydrogen Bottle:

1. Purge the system to *He* as described in step 2 of the normal TC operation Procedure above.

2. Change the bottle, removing the empty one from MTA gas shed.

3. Purge the system to H_2 as described in step 3 of the normal TC operation Procedure above.

To Make a Controlled Access into MTA experimental hall

We anticipate no more than several controlled accesses during the course of the weekend for the purpose of adding LN_2 and/or changing electrodes in the TC.

1. Go to the Main Control Room, *MCR*, to request a controlled access and pick up keys
   First time at MCR, experimenters: Pierrick Hanlet, Robert Hartline, Rolland Johnson, Alfred Moretti, Kevin Paul, Milorad Popovic, and Katsuya Yonehara must read and sign work permit

2. Vent TC

3. LOTO the H_2 and *He* bottles

4. Lock Gas Shed (this will need to be done each time an experimenter is leaving the shed)

5. Upon completion of access, verify that Hydrogen Safety door is closed *(not locked!)*

6. Return access keys to MCR

TC Cooldown Procedures

The MTA is ODH class 0. Nonetheless, certain precautions should be taken to ensure the safety of users.

Place the TC in the cryostat and connect it to the klystron via coaxial/waveguide lines. Once connected, fill the cryostat using hand carried dewars filled from the LN_2 located outside the MTA gas shed. Approximately *30 l* of LN_2 will boil off during this cooldown. Additional filling of the cryostat will be needed as the LN_2 will boil off as tests are performed; this amount depends on heat leaks and RF loads.

Six-dimensional muon beam cooling using a homogeneous absorber: Concepts, beam dynamics, cooling decrements, and equilibrium emittances in a helical dipole channel

Yaroslav Derbenev
Thomas Jefferson National Accelerator Facility, Newport News, Virginia 23606, USA

Rolland P. Johnson*
Muons, Inc., Batavia, Illinois 60510, USA

(Received 15 December 2003; revised manuscript received 15 September 2004; published 29 April 2005)

The fast reduction of the six-dimensional phase space of muon beams is an essential requirement for muon colliders and also of great importance for neutrino factories based on accelerated muon beams. Ionization cooling, where all momentum components are degraded by an energy absorbing material and only the longitudinal momentum is restored by rf cavities, provides a means to quickly reduce transverse beam sizes. However, the beam energy spread cannot be reduced by this method unless the longitudinal emittance can be transformed or exchanged into the transverse emittance. Emittance exchange plans until now have been accomplished by using magnets to disperse the beam along the face of a wedge-shaped absorber such that higher momentum particles pass through thicker parts of the absorber and thus suffer larger ionization energy loss. In the scheme advocated in this paper, a special magnetic channel designed such that higher momentum corresponds to a longer path length, and therefore larger ionization energy loss, provides the desired emittance exchange in a homogeneous absorber without special edge shaping. Normal-conducting rf cavities imbedded in the magnetic field regenerate the energy lost in the absorber. One very attractive example of a cooling channel based on this principle uses a series of high-gradient rf cavities filled with dense hydrogen gas, where the cavities are in a magnetic channel composed of a solenoidal field with superimposed helical transverse dipole and quadrupole fields. In this scheme, the energy loss, the rf energy regeneration, the emittance exchange, and the transverse cooling happen simultaneously. The theory of this helical channel is described in some detail to support the analytical prediction of almost a factor of 10^6 reduction in six-dimensional phase space volume in a channel about 56 m long. Equations describing the particle beam dynamics are derived and beam stability conditions are explored. Equations describing six-dimensional cooling in this channel are also derived, including explicit expressions for cooling decrements and equilibrium emittances.

DOI: 10.1103/PhysRevSTAB.8.041002 PACS numbers: 29.27.−a, 29.20.−c, 14.60.Ef, 41.85.Lc

I. INTRODUCTION

The fast reduction of the six-dimensional (6D) phase space of muon beams is an essential requirement for muon colliders [1–3] and also of great importance for neutrino factories [4–6] based on accelerated muon beams. Ionization cooling [7,8] provides a means to quickly reduce transverse beam sizes, but the beam momentum spread cannot be reduced by this method unless the longitudinal emittance can be transformed or exchanged into the transverse emittance.

In the scheme advocated in this paper, a muon beam cooling channel is made of a series of rf cavities filled with high-density hydrogen gas, which provides simultaneous emittance exchange and transverse ionization cooling by virtue of a superimposed helical magnetic field. Coils placed outside of the rf cavities create a solenoidal magnetic field component, which does not change direction, and transverse dipole and quadrupole helical components, which change direction along the channel axis in the same manner as is found in spin-rotating magnets used in Siberian snakes [9]. The energy loss, the rf energy regeneration, the emittance exchange, and the transverse cooling happen simultaneously. Except for the pressure windows at the two ends of the channel, the muons pass only through hydrogen for the most efficient cooling possible. As the beam travels down the channel the beam bunches become shorter and smaller such that higher-frequency rf cavities with smaller transverse dimensions can be used to allow more efficient rf parameters and smaller diameter magnets to enable higher fields and gradients.

A. Emittance exchange in a homogeneous absorber

The idea that is the basis of this paper for a 6D cooling channel is seen in a comparison of Figs. 1(a) and 1(b). Figure 1(a) is a conceptual picture of the usual mechanism for reducing the energy spread in a muon beam. The dispersion of the beam generated by the dipole magnet in Fig. 1(a) creates an energy-position correlation at a wedge-shaped absorber. Higher energy particles pass through thicker parts of the absorber and so have more energy loss than particles of less energy. After the absorber the beam becomes more monoenergetic. This process is emit-

*Corresponding author.
Email address: rol@muonsinc.com

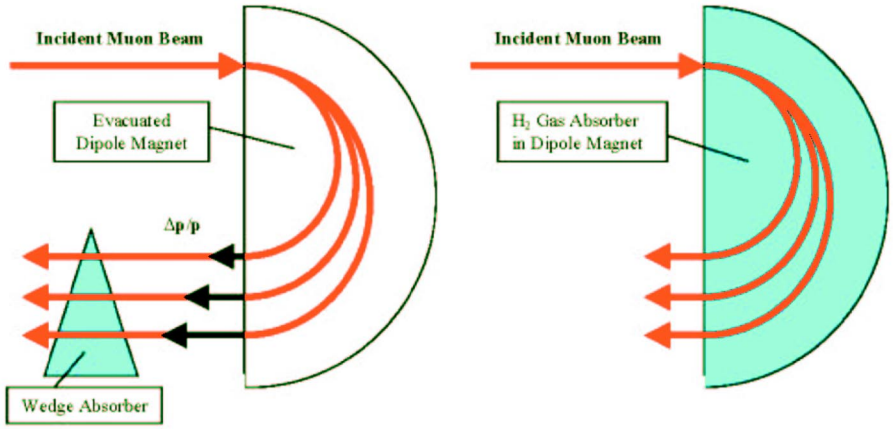

FIG. 1. (Color) (a) Wedge absorber technique and (b) new homogeneous absorber technique.

tance exchange, as it is sometimes called, because the transverse emittance must grow to allow the longitudinal emittance to be cooled. In Fig. 1(a), the beam is in vacuum except in the wedge absorber. Subsequent rf cavities, also in vacuum, replace the energy lost in the absorber. The process is limited by multiple scattering in the absorber and the high-Z windows that isolate the evacuated rf cavities and that contain the absorbers.

In previous cooling plans, both the emittance exchange process and the transverse ionization beam cooling processes have been implemented by sequentially alternating absorbers and evacuated rf cavities. Moreover, the usual 6D schemes require sequential use of wedge absorbers for emittance exchange followed by unshaped absorbers for transverse cooling followed by rf cavities to regenerate the lost energy.

The new idea advocated in this paper is shown conceptually in Fig. 1(b). In this simpler picture, the cooling-channel magnets are filled with dense gaseous energy absorber. The magnetic dispersion creates a longer path length for particles of higher momentum. The longer path length, in turn, times the absorber dE/ds gives the energy loss correlation with momentum needed for 6D cooling. Thus a homogeneous absorber, without shaped edges, can be used to accomplish emittance exchange. Note that the 180° geometry shown in the figures is chosen purely to illustrate the principles involved; the geometry of the cooling channel proposed below is quite different.

A second new idea advocated here is that the rf cavities can be inside the cooling-channel magnets and operate while filled with the gaseous energy absorber. Thus the ionization energy loss and the rf energy regeneration can be simultaneous rather than sequential.

B. rf cavities filled with absorber

The initial concept that a homogeneous absorber, one without shaped edges, would be attractive for emittance exchange is related to the development of rf cavities filled with dense gas [10]. A project [11] presently underway at Fermilab has demonstrated that an 800 MHz rf cell filled with cold, pressurized hydrogen gas can achieve 80 MV/m with exceptionally short conditioning times [12]. This project is to study the use of high-pressure gases in rf cavities to facilitate large gradients by suppressing high-voltage breakdown by virtue of Paschen's law [13]. A series of contiguous pillbox cavities similar to the one being developed in this project could define the helical cooling channel described in this paper.

Most rf cavities associated with particle accelerators operate in as close to a vacuum as possible to avoid electrical breakdown. This is done so that electrons or ions that are accelerated by the high voltages in the rf cavity rarely encounter atoms of the residual gas, and so the avalanche process of breakdown is inhibited. Other rf systems that do not require the ultrahigh vacuum of an accelerator typically suppress rf breakdown by using dense materials between electrodes. Ions passing through these materials, which include high-pressure and/or high-density gases, have such a short mean free path between collisions that they do not accelerate to energies high enough to create an avalanche. The relationship between the electrical breakdown voltage and the product of gas pressure and gap width is known as Paschen's law.

The gas in the cavities also acts as the energy absorber needed for ionization cooling, where hydrogen or helium are the only realistic choices because of their favorable energy loss and radiation length. All things considered, however, hydrogen is superior in all aspects except for perceived safety concerns. Hydrogen gas has over twice the ionization cooling effectiveness as helium in that it allows a final cooled emittance, proportional to $(Z + 1)$, that is smaller by a factor of 1.5 in each transverse plane. At the same pressure, hydrogen suppresses rf breakdown at a voltage that is 6 times higher than helium. Hydrogen is also superior in heat capacity and viscosity, which are important parameters for the engineering of a practical cooling channel.

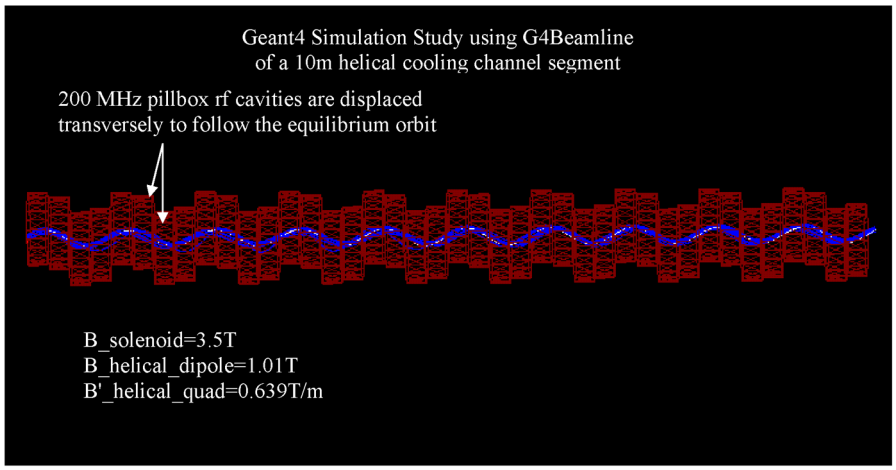

FIG. 2. (Color) G4BEAMLINE display of a 10-m-long segment of a helical cooling channel that is being simulated. The outlines of the forty 200 MHz pillbox rf cavities are shown in red. In this simulation, superimposed magnetic fields with solenoidal and helical components provide focusing and dispersion as the muons pass through the hydrogen-filled rf cavities. Muon trajectories are shown (blue) as they oscillate about the equilibrium orbit (white).

This idea of filling rf cavities with gas is new for particle accelerators and is only possible for muons because they do not scatter as do strongly interacting protons or shower electromagnetically as do less-massive electrons. Additionally, use of a gaseous absorber presents other practical advantages that make it a simpler and more effective cooling method compared to liquid hydrogen flasks in the conventional designs of transverse cooling channels, such as the scheme envisioned by the MICE Collaboration [14] for a demonstration experiment proposed for Rutherford Appleton Laboratory (RAL).

C. Helical cooling channel segment example

Figure 2 is a display from G4BEAMLINE [15], a simulation program based on GEANT4 [16], of an initial 10-m-long cooling channel segment, which shows one possible arrangement of pressurized rf cavities. In this example, the rf cavities are displaced transversely from the structure axis such that the muon beam passes through their centers. The 40 rf cavities shown in red in this example are 200 MHz pillbox cavities with 30 cm diameter aperture. Figure 3 is an end view of the same channel, where the (red) outlines of the rf cavities can be seen. Fifty muon trajectories (blue) are seen relative to the (white) equilibrium orbit.

Superconducting coils (not shown) surround the rf cavities to provide a magnetic field with solenoidal, helical dipole, and helical quadrupole components to create the muon orbits indicated by the blue traces in the figure. The object of this paper is to describe the characteristics of this magnetic channel, which has unusually good acceptance and cooling qualities. The simulations of this channel are underway and will be reported in later papers. Later in this paper, a cooling channel example is described which has three segments such as the one shown here, each with rf frequencies and dimensions adjusted as the beam shrinks to attain optimum cooling rates.

D. Comparison with ring coolers

There have been several proposed emittance exchange schemes based on the use of wedge absorbers in muon beam accelerators and storage rings [1,2,17]. The most recent progress in the study of 6D cooling has been with ring coolers (RC), where muons pass several times through a small storage ring with dispersion regions for emittance

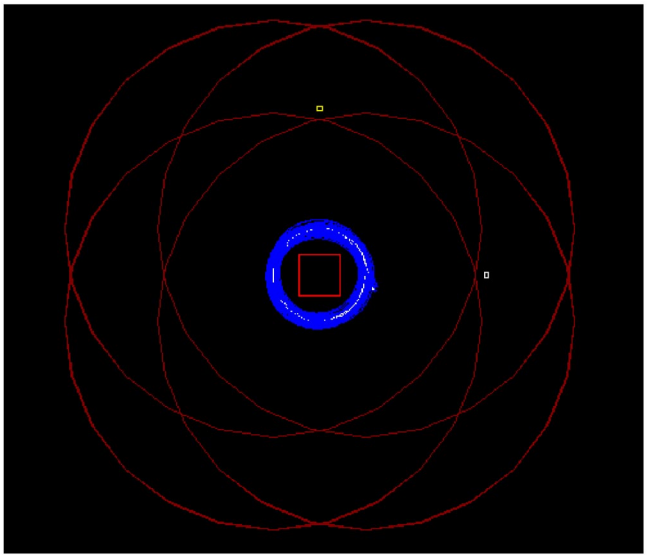

FIG. 3. (Color) The same conditions as Fig. 2, but viewed looking down the cooling channel. The beam here is at 200 MeV/c with a helix radius of 11 cm. The outlines of the radially displaced rf cavities are shown in red. The red box shown for orientation in the center is 10 cm on a side.

exchange cooling [18]. RCs are sophisticated devices, where many difficult problems have been addressed using combinations of dipole, solenoidal, and quadrupole magnets interspersed with rf cavities and energy absorbers of different materials and shapes.

Although 6D cooling is very much required to satisfy the requirements of a muon collider, in the most recent exercises it is looked at more often as a possible way to economize the construction costs of a neutrino factory. In this context, 6D cooling reduces transverse beam sizes and bunch lengths so that higher frequency and therefore more economical rf can accelerate muons to the energy of the storage ring of a neutrino factory. This acceleration to the storage ring energy in Fermilab and Brookhaven neutrino factory design studies used recirculating linacs, which amounted to more than a quarter of the neutrino factory construction costs.

An RC is in itself a way to economize in that the 15 or so turns the beam makes during the cooling process allows equipment to be reused. A ring is also a rather familiar device for accelerator physicists, where tricks for dispersion creation and simultaneous matching of transverse and longitudinal constraints are known.

All RCs share common difficulties. Injection (and extraction to a lesser extent) is particularly troublesome because it requires a kicker magnet with parameters unlike any that have been built up to now because the initial beam size is large. The space in the ring lattice taken up by the injection/extraction system usually causes some problem because it changes the symmetry of the ring and displaces rf and absorbers, reducing cooling efficiency. The RC must be designed to accommodate the initial conditions of the muon beam when it is injected. As the beam gets cooled, all six dimensions shrink and the RC is less and less a good match to the beam size, especially from the standpoint of dispersion, absorber parameters, and rf frequency. Additional difficulties with ring coolers arise from the multiple passes of the beam through rf cavities and absorbers, where rf beam loading and absorber heating issues are just being addressed.

Since the cooling channel that we are advocating in this paper is essentially a linac filled with absorber, these difficulties are not issues. Injection and extraction, matching to the beam dimensions as the beam cools, and rf beam loading and absorber heating from multiple passes are not problems for a linear cooling channel.

RCs cannot easily take advantage of the pressurized high-gradient rf cavities being developed by Muons, Inc. and IIT at Fermilab. To use these rf cavities effectively, the entire ring would have to be filled with dense hydrogen gas since pressure windows would be counterproductive. Beam passing through areas without rf cavities would then suffer a large energy loss. Reducing the gas density could reduce the energy loss, but that would diminish the hoped-for gains of the pressurized cavities. Nevertheless, we note that the idea of using gas-filled ring coolers is being investigated with encouraging results [19].

RCs and the helical channel proposed here are similar in two respects. First, neither will easily accept a beam from a pion decay channel without some transverse precooling, rf bunching, and carefully matched injection parameters. Second, the helical channel has features of a weak focusing storage ring [20] (installed in a vertical plane, with an effective field index calculated below), where the orbits follow a spiral rather than a circular path.

II. GENERAL TECHNICAL APPROACH

A. Helical magnets

The technology of helical dipole magnets [21] is well known, for example, at Brookhaven where helical ''Siberian snakes'' [22] are used for spin control in RHIC. A helical dipole can be imagined as a superconducting dipole magnet wound on a beam tube, much like a Tevatron superconducting dipole, twisted about its axis so that the dipole bending field rotates its direction as the particle passes down the tube. A schematic of a helical dipole magnet [23] is shown in Fig. 4. We note that for initial ionization cooling of a muon beam, the helical magnets may require 4 times the aperture than has been used up to now (~ 30 cm). Also note that the field of a helical dipole magnet is not intuitively obvious. For example, depending on the dimensions and period, the longitudinal and the transverse components can be comparable and have significant gradients. Given the right initial conditions, a particle will pass through this magnet on a helical trajectory about the magnet axis.

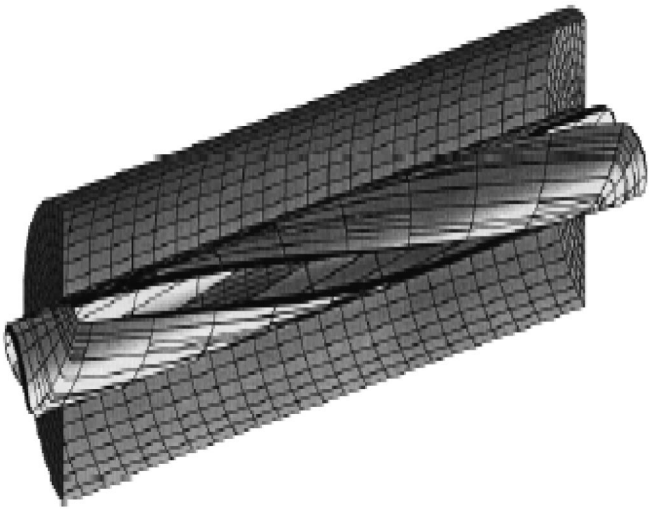

FIG. 4. Schematic representation of a helical dipole magnet showing the coil configuration and a cutaway view of the iron flux-return cylinder.

B. Helical cooling channel

The path of a muon traveling down a solenoid without helical magnets is also a helix, where the muon momentum transverse to the axis of the solenoid generates a projected circular orbit with the usual Larmor or cyclotron radius and frequency. If the muons pass through an energy absorber as is required for ionization cooling, the momentum and the cyclotron radius are reduced. This damping of transverse momentum in a solenoid without helical magnets is the basis for most schemes to accomplish transverse ionization cooling. Namely, rf cavities replace the energy lost in the absorber, boosting the beam momentum in the longitudinal direction so that the angular spread $(p_\perp/p_z)$ is reduced until it is limited by multiple scattering in the absorber [24].

However, in order to cool the 6D emittance of a beam, the longitudinal motion must be moved to the transverse directions where ionization cooling is effective, as indicated in Fig. 1(b). This emittance exchange is accomplished in the channel proposed in this paper by superimposing a transverse helical dipole magnet to the solenoid on the same axis to make possible longitudinal as well as transverse cooling. As will be shown, the helical dipole magnet creates an outward radial force due to the longitudinal momentum of the particle while the solenoidal magnet creates an inward radial force due to the transverse momentum of the particle, or

$$\begin{aligned} F_{h\text{-dipole}} &\approx p_z \times B_\perp; \qquad b \equiv B_\perp, \\ F_{\text{sol}} &\approx -p_\perp \times B_z; \qquad B \equiv B_z, \end{aligned} \tag{2.1}$$

where B is the field of the solenoid, the axis of which defines the z axis, and b is the field of the transverse helical dipole at the particle position. These are the Lorentz forces that are the starting point (3.6) for the derivations of the stability conditions for particle motion in these fields in Sec. III. By moving to the rotating or helical frame of reference that follows the field of the helical dipole magnet, a time and z-independent Hamiltonian is then developed to explore the characteristics of particle motion in the magnetic fields of the channel. After this, a continuous homogeneous energy absorber is added along with the ''continuous'' rf cavities needed to compensate for the energy loss and thus maintain the radius of the equilibrium orbit. Equations describing six-dimensional cooling in this channel are also derived, including explicit expressions for cooling decrements and equilibrium emittances.

Some of the actual theoretical development of this cooling channel was worked out some years ago by one of the authors [17]. In that work, the absorber was seen as composed of a homogeneous part and a part with a density gradient. Since the thinking at the time was that the wedge absorber scheme shown in Fig. 1(a) should be dominant, especially in that discrete absorbers were always envisioned, the contributions from the homogeneous absorber were not considered as significant. The ideas and mathematical descriptions become more transparent in the case of a continuous homogeneous absorber. Much of the conceptual simplicity is lost in the case of discrete absorbers that must be carefully placed between magnetic coils and between rf cavities.

For a given beam momentum, one can vary the solenoid field and the strength and period of the helical dipole field. (The hydrogen gas energy-absorber density is also a free parameter provided the density is sufficient to suppress rf breakdown at the required level.) As we will demonstrate below, the helical field that must be superimposed on the solenoidal field must have a quadrupole component in addition to the dipole component in order to give the beam additional stability. This component could be added with ''cos2θ'' quadrupole magnets having the same twist period as, and superimposed on, the helical dipole coils.

It is important to note that the direction of the solenoidal field does not change in the cooling channel described below. This is an essential difference between the helical dipole method and the solenoidal schemes with alternating field directions that have been envisioned up to now. This may also be some technical advantage to the extent that the large magnetic forces on the superconducting coils at the field reversal regions can be eliminated. Although a discussion of technical issues should follow the complete analysis of beam dynamics and cooling, we note that the use of continuous (or long) solenoids inherent in the helical concept should allow a higher maximum effective longitudinal field than that of schemes with alternating solenoidal field directions. Consequently, the helical scheme will achieve a smaller equilibrium emittance, faster cooling rate, and decreased particle loss from decay.

III. HELICAL ORBIT DYNAMICS

Beam dynamics in a helical channel has been studied for free electron lasers using a specific structure with only odd transverse field harmonics and a solenoid [25] and for a structure including a quadrupole harmonic but no solenoid [26]. Below we reproduce an analysis performed earlier [17] for the general case. In developing the cooling theory for a helical beam channel, the only important requirement is that the beam size $\sigma_\perp$ should be small with respect to the helix parameter, $\lambda/2\pi$. A small beam momentum spread is not assumed.

A. Notation

In this paper it is assumed that

$-e = 1$, in order to simplify later equations involving magnetic fields;

$c = 1$;

$\vec{p}$ is the particle vector momentum;

$E = \gamma m = \sqrt{p^2 + m^2}$; $\beta = \sqrt{1 - (1/\gamma^2)}$;

$k = 2\pi/\lambda$, where λ is the transverse field period, and also the helical orbit period;

a is the helix orbit radius (a function of p);

$\kappa = ka$ is a in terms of $\lambda/2\pi$, such that $\kappa = p_\perp/p_z$ for the periodic orbit;

$D = p\frac{da}{dp}$ is the dispersion; $\hat{D} = D/a$ is the dispersion factor;

x, y, z is the Cartesian laboratory frame;

$\vec{\rho} = (x, y)$ is the particle transverse coordinate relative to the structure axis;

ρ and φ are the axial coordinates: $x + iy = \rho e^{i\varphi}$;

$\hat{x}$ is the complex transverse coordinate in the rotating or helical frame:

$$\hat{x} = (x + iy)e^{-ikz} = \rho \exp[i(\varphi - kz)];$$

$\vec{B} = (0, 0, B)$ is the solenoid field;

$k_c = B\sqrt{1 + \kappa^2}/p$;

$q = (k_c/k) - 1$;

b is the transverse magnetic field value at the periodic orbit;

$\vec{b}(x, y, z)$ is the 3-vector of the periodic field:

$$\vec{b}(x, y, z + \lambda) = \vec{b}(x, y, z).$$

The relationship between the helical magnetic field in the two frames is

$$b_x + ib_y = (b_\rho + ib_\varphi)e^{i\varphi},$$

where b_ρ, b_φ, and b_z are functions of only ρ and $\psi \equiv \varphi - kz$;

Q_+ and Q_- are Q values or tunes, i.e., transverse oscillation frequencies about the periodic orbit;

ψ_+ and ψ_- are the phases of free transverse oscillations ($\psi'_\pm = kQ_\pm$);

I_+ and I_- are the corresponding action variables (adiabatic invariants, or generalized Courant-Snyder invariants);

Λ_+ and Λ_- are the transverse cooling decrements ($I'_\pm = -\Lambda_\pm I_\pm$ after averaging over $\psi_\pm$);

Λ_γ is the energy cooling decrement:

$$\Lambda_\gamma = -\frac{d}{d\gamma}\langle\gamma'\rangle,$$

where the brackets $\langle\,\rangle$ mean averaging over free transverse oscillations (i.e., $\psi_\pm$) and z.

Figure 5 shows some of the important geometrical relationships between the magnetic fields and particle coordinates used below. Consider a particle of momentum p at a radius of $a(p)$ in a stable helical orbit about the z axis of the structure, which is parallel to the solenoidal field B. The parameter $\kappa = p_\perp/p_z$ is the tangent of the pitch angle of the helical orbits. In the numerical example in Sec VI, this angle is 45° and $\kappa = 1$ as shown in the figure. The transverse helical dipole field b is orthogonal to the z axis and to the radius vector a. The beam has to be specially prepared and injected into the channel so that the net transverse

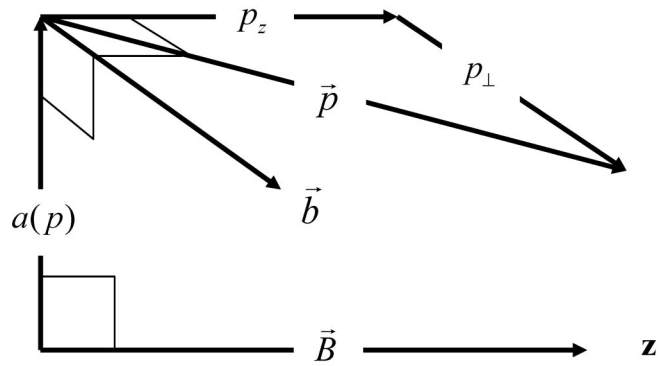

FIG. 5. Diagram of important relationships. The z axis coincides with the solenoid axis. At the periodic orbit, the transverse helical dipole field b is orthogonal to B and the radius vector a. The pitch angle of the helix is the arctan ($\kappa = p_\perp/p_z$).

displacements and divergences of its centroid are matched to the helical equilibrium orbit.

Figure 6 is an illustration of how the beam moves around the structure axis under the influence of the transverse dipole and solenoidal fields. The periodic equilibrium orbit is a helix of constant radius; particles oscillate transversely about this orbit and oscillate longitudinally with respect to the rf with frequencies or tunes as described below. The motion is in the gaseous hydrogen energy absorber that fills the volume of a contiguous series of pillbox rf cavities, which continuously replenish the lost energy. Superconducting coils outside the rf cavities provide the magnetic field of the helical channel.

B. Helical field

A static magnetic field in vacuum can be represented as a gradient vector of a scalar function:

$$\vec{b} = \vec{\nabla}U,$$

where $U(\vec{r})$ satisfies the equation $\nabla^2 U = 0$.

In the case of a helical structure, U should reflect helical invariance by being a function of $\psi \equiv \varphi - kz$ and ρ:

$$U(\vec{r}) = U(\rho, \psi).$$

Then

$$b_\rho = \frac{\partial U}{\partial \rho}, \qquad b_\varphi = \frac{\partial U}{\rho\,\partial \varphi}, \qquad b_z = -k\rho b_\varphi.$$

The Fourier expansion

$$U = \sum_{\ell \neq 0} U_\ell(\rho)e^{i\ell\psi}$$

leads to an equation for $U_\ell(\rho)$:

$$\frac{1}{\rho}\frac{d}{d\rho}\left(\rho\frac{dU_\ell}{d\rho}\right) - \left(\frac{1}{\rho^2} + k^2\right)\ell^2 U_\ell = 0.$$

A solution regular at $\rho = 0$ is a modified Bessel function:

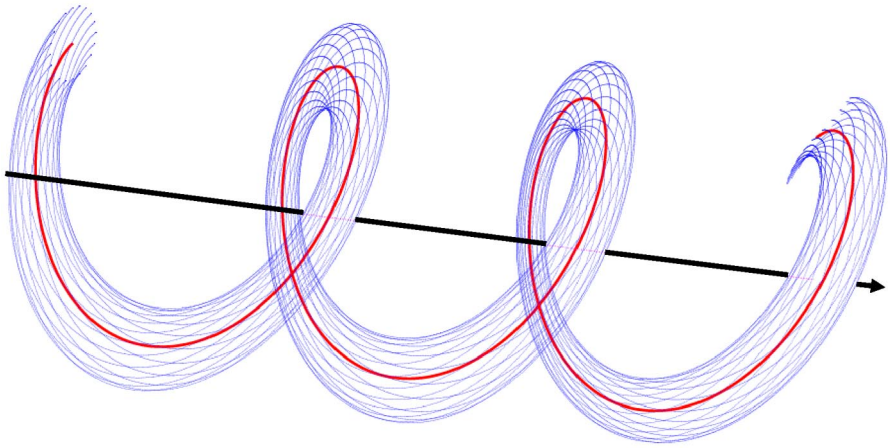

FIG. 6. (Color) Illustration of motion of the beam about the z axis (black), which coincides with the solenoid center. For a given momentum, muons (blue) oscillate about the periodic equilibrium orbit (red). This view in perspective shows 20 muons as they oscillate about the equilibrium orbit for three helix periods.

$$U_\ell = \text{const} \times I_\ell(\ell k\rho),$$

$$I_\ell(t) = \left(\frac{t}{2}\right)^\ell \sum_{n=0}^{\infty} \frac{(t^2/4)^n}{n!(n+\ell)!} \to \begin{cases} (\frac{t}{2})^\ell/\ell! & t \ll 1 \\ \frac{e^t}{\sqrt{2\pi t}} & t \gg \ell^2. \end{cases} \quad (3.1)$$

Each harmonic is independent and corresponds to a current distribution

$$j_z, \qquad j_\varphi \propto e^{i\ell\psi}.$$

The most important harmonics are the dipole ($\ell = 1$),

$$b_\varphi = 2b_d I_1(k\rho)(\cos\psi)/k\rho, \qquad b_\rho = 2b_d I_1'(k\rho)\sin\psi,$$
$$b_z = -k\rho b_\varphi, \quad (3.2)$$

and quadrupole ($\ell = 2$):

$$b_\varphi = \left(\frac{\partial b_\varphi}{\partial \rho}\right)_o \frac{I_2(2k\rho)}{k^2\rho}\cos 2(\psi - \psi_2),$$
$$b_\rho = \frac{1}{k}\left(\frac{\partial b_\varphi}{\partial \rho}\right)_o I_2'(2k\rho)\sin 2(\psi - \psi_2), \quad (3.3)$$
$$b_z = -k\rho b_\varphi, \qquad \psi_2 = \text{const},$$

where b_d and $(\frac{\partial b_\varphi}{\partial \rho})_o$ are the dipole and quadrupole strengths at $\rho = 0$, respectively. Sextupole ($\ell = 3$) and octupole ($\ell = 4$) harmonics might be needed for particular improvements. We note that this description corresponds to a field produced by simple external conductors and that other helical configurations of conductors are possible that would best be described by complementing the field description above with MacDonald functions. In fact, our considerations below rely only on the helical invariance of the fields and not on the details of the magnet design.

C. Equations of motion in a helical field

Here we derive the equations of motion in the absence of absorbers and rf fields. Since the corresponding forces for absorbers and rf are weak, these effects can be treated using perturbative methods after the magnetic dynamical problem is solved. The Cartesian coordinates are the two transverse coordinates x, y, and the longitudinal coordinate z which coincides with the axis of the magnetic structure, having unit vectors $\vec{e}_x, \vec{e}_y, \vec{e}_z$. In the following calculations we use the definitions and relationships from above and

$$\frac{dz}{dt} \equiv (\dot{z}), \qquad \beta_z dt = dz, \qquad \frac{d}{dz} \equiv ('), \qquad \vec{\rho} = (x, y), \quad (3.4)$$

$$\vec{p}_\perp = p_z \vec{\rho}', \qquad \frac{p_z}{p} = \frac{\beta_z}{\beta} = \frac{1}{\sqrt{1 + (\vec{\rho}')^2}}. \quad (3.5)$$

Let us use the initial Lorentz equation

$$\dot{\vec{\rho}} = (B\vec{e}_z + \vec{b}) \times \vec{\beta} \quad (3.6)$$

in order to separate out the equation for transverse motion

$$\dot{\vec{\rho}}_\perp = (B + b_z)\vec{e}_z \times \vec{\beta}_\perp + \beta_z \vec{b}_\perp \times \vec{e}_z. \quad (3.7)$$

Using (3.4) and (3.5), and complex representation with

$$u = x + iy, \qquad i^2 = -1,$$

we can rewrite (3.7) as follows:

$$(p_z u')' = i(B + b_z)u' - i(b_x + ib_y). \quad (3.8)$$

This equation is complemented by the expression for p_z', which can easily be obtained using the conservation of total momentum p,

$$p_z' = -\frac{1}{2} p \frac{(|u'|^2)'}{(1 + |u'|^2)^{3/2}}. \quad (3.9)$$

Next, transform Eq. (3.8) to the rotating (helical) frame x_1, x_2, z with unit vectors $\vec{e}_1(z), \vec{e}_2(z), \vec{e}_z$, where the subscript 1 corresponds to the radial coordinate and field directions and the subscript 2 indicates the azimuthal coordinate and field directions.

Using the relationships

$$\hat{x} \equiv x_1 + ix_2 = ue^{-ikz},$$

$$u' = (\hat{x}' + ik\hat{x})e^{ikz},$$

$$\vec{\rho} = x\vec{e}_x + y\vec{e}_y = x_1\vec{e}_1 + x_2\vec{e}_2,$$

$$\vec{e}_x + i\vec{e}_y = (\vec{e}_1 + i\vec{e}_2)e^{ikz},$$

and

$$b_x + ib_y = (b_1 + ib_2)e^{ikz},$$

we find

$$p_z(\hat{x}'' + 2ik\hat{x}' - k^2\hat{x}) + (p_z' - iB - ib_z)(\hat{x}' + ik\hat{x}) + i(b_1 + ib_2) = 0, \tag{3.10}$$

with

$$p_z = \frac{p}{\sqrt{1 + |\hat{x}' + ik\hat{x}|^2}},$$
$$p_z' = -\frac{1}{2}p\frac{(|\hat{x}' + ik\hat{x}|^2)'}{(1 + |\hat{x}' + ik\hat{x}|^2)^{3/2}}.$$

Recall that

$$b_z = k(x_2b_1 - x_1b_2),$$

and the transverse field components b_1 and b_2 are functions of only x_1 and x_2, but not z. Thus, the transverse x_1 and x_2 dynamics in the helical frame is conservative, although the equations are coupled and nonlinear.

D. Helical orbits

1. Periodic orbits

It follows from the periodicity of the helical fields that there will be periodic orbits with the same periodicity. The periodic orbit is determined as a solution of (3.10) at

$$\rho = \text{const} \equiv a, \qquad x_1 = a, \qquad x_2 = 0,$$
$$\varphi' = \text{const} = k, \qquad \text{i.e., } \psi' = 0, \qquad \psi = 0,$$
$$b_2 = b_2(ka) \equiv b, \qquad b_1(\psi = 0) = 0, \qquad p_z = \frac{p}{\sqrt{1 + \kappa^2}}.$$

The equilibrium equation is obtained as follows:

$$\frac{k_c}{k} - 1 = \frac{(1 + \kappa^2)^{3/2}}{kp\kappa}b, \tag{3.11}$$

or

$$p(a) = \frac{\sqrt{1 + \kappa^2}}{k}\left[B - \frac{1 + \kappa^2}{\kappa}b\right], \tag{3.12}$$

or

$$\frac{b}{B} = \frac{\kappa}{1 + \kappa^2}\left(1 - \frac{k}{k_c}\right) = \frac{\kappa}{1 + \kappa^2}\left(\frac{q}{q + 1}\right). \tag{3.13}$$

2. Dispersion

The dispersion factor

$$\hat{D} = \frac{p}{a}\frac{da}{dp}$$

plays a key role in the emittance exchange effect. It can be found immediately using the equilibrium Eq. (3.12):

$$\frac{p}{a}\frac{da}{dp} = \left(\frac{a}{p}\frac{dp}{da}\right)^{-1};$$

the result can be expressed as

$$\hat{D}^{-1} = \frac{\kappa^2 + (1 - \kappa^2)q}{1 + \kappa^2} + g, \tag{3.14}$$

where the effective field index at the periodic orbit is

$$g \equiv \frac{-(1 + \kappa^2)^{3/2}}{pk^2}\frac{\partial b}{\partial a}. \tag{3.15}$$

Note that the dispersion factor $\hat{D}$ does not vanish at $a \to 0$, while the dispersion $D = \hat{D}a$ disappears.

E. Transverse oscillations about the periodic orbit

1. Tunes of the helical orbits

Consider a position u_1, u_2, relative to the periodic orbit

$$u_1 = x_1 - a(p); \qquad u_2 = x_2. \tag{3.16}$$

Assume $b_1 = 0$ and $(\frac{\partial b_2}{\partial \psi}) = 0$ at $\psi = 0$. After a linear expansions of Eq. (3.10) with

$$k^2(u_1^2 + u_2^2) \ll 1, \qquad (u_1')^2 + (u_2')^2 \ll 1, \tag{3.17}$$

and taking into account the field laws and equilibrium relationship in (3.11), we obtain two linear equations:

$$u_1'' + \frac{q - 1}{1 + \kappa^2}ku_2' + k^2\hat{D}^{-1}u_1 = 0, \tag{3.18}$$

and

$$u_2'' - (q - 1)ku_1' + k^2(q - g)u_2 = 0. \tag{3.19}$$

These equations are conservative but coupled. The coupling is due to a difference between the Coriolis force and the nonequilibrium part of the Lorentz force of the solenoid. At $k_c = 2k$, u_1 and u_2 become decoupled (in linear approximation). In the following development we do not assume that u_1 and u_2 are decoupled, but treat the general case. The solution of these equations can be found as

eigenvectors

$$\begin{pmatrix} u_1 \\ u_2 \end{pmatrix} = \begin{pmatrix} c_1 \\ c_2 \end{pmatrix} e^{ikQz}, \quad \text{at} \begin{pmatrix} c_1 \\ c_2 \end{pmatrix} = \text{const},$$

where we obtain the zero determinant equation:

$$Q^4 - 2Q^2R + G = 0, \tag{3.20}$$

with

$$G = (q - g)\hat{D}^{-1} = \left(\frac{2q + \kappa^2}{1 + \kappa^2} - \hat{D}^{-1}\right)\hat{D}^{-1} \tag{3.21}$$

and

$$R \equiv \frac{1}{2}\left(1 + \frac{q^2}{1 + \kappa^2}\right). \tag{3.22}$$

Thus, the Q values are found:

$$Q^2 = Q_\pm^2 \equiv R \pm \sqrt{R^2 - G}, \tag{3.23}$$

and the stability area is established:

$$0 < G < R^2. \tag{3.24}$$

Note that

$$Q_+^2 \cdot Q_-^2 = G, \tag{3.25}$$

while

$$Q_+^2 + Q_-^2 = 2R. \tag{3.26}$$

Thus we have two tunes for the normal mode oscillations. For a solenoidal field alone, there is only a single frequency, but when the helical field is added the frequency is split.

2. Transverse oscillations

Using Eq. (3.18), we find the normal oscillation behavior:

$$X_\pm \equiv \left| \begin{matrix} u_1 \\ u_1' \\ u_2 \\ u_2' \end{matrix} \right|_\pm = a_\pm \left| \begin{matrix} \cos\psi_\pm \\ -kQ_\pm \sin\psi_\pm \\ (\alpha_\pm/Q_\pm)\sin\psi_\pm \\ k\alpha_\pm \cos\psi_\pm \end{matrix} \right|, \tag{3.27}$$

where $a_\pm = \text{const}$, $\psi_\pm = Q_\pm kz + \text{const}$, and

$$\alpha_\pm = \frac{1 + \kappa^2}{q - 1}(Q_\pm^2 - \hat{D}^{-1}).$$

We note the useful relationships

$$\hat{D}\alpha_+\alpha_- = -(1 + \kappa^2) \tag{3.28}$$

and

$$\frac{Q_+^2}{\alpha_+} - \frac{Q_-^2}{\alpha_-} = \frac{\alpha_+ - \alpha_-}{1 + \kappa^2} = \frac{2}{q - 1}\sqrt{R^2 - G}. \tag{3.29}$$

The general solution X is a sum of $X_\pm$ and the helix path:

$$\left| \begin{matrix} x_1 \\ x_1' \\ x_2 \\ x_2' \end{matrix} \right| = X_+ + X_- + \left| \begin{matrix} a(p) \\ 0 \\ 0 \\ 0 \end{matrix} \right|. \tag{3.30}$$

3. Amplitudes

The solution in (3.27) can be treated also as a transformation from x_1, x_1', x_2, x_2' to variables of amplitudes and phases of normal mode oscillations. This is reasonable to the extent that perturbative forces related to nonlinearities or nonadiabatic changes of fields and absorbers are small during a single oscillation period. The squared amplitudes are of primary importance. The transformed relationships can be easily found using (3.27) and (3.30)

$$x_2' - k\alpha_\mp(x_1 - a) = (\alpha_\pm - \alpha_\mp)ka_\pm \cos\psi_\pm, \tag{3.31}$$

and

$$\alpha_\mp x_1' + kQ_\mp^2 x_2 = \frac{1}{Q_\pm}(\alpha_\pm Q_\mp^2 - \alpha_\mp Q_\pm^2)ka_\pm \sin\psi_\pm. \tag{3.32}$$

Thus,

$$k^2a_+^2 = \frac{[x_2' - \alpha_- k(x_1 - a)]^2}{(\alpha_+ - \alpha_-)^2} + Q_+^2 \frac{(\alpha_- x_1' + Q_-^2 kx_2)^2}{(\alpha_+ Q_-^2 - \alpha_- Q_+^2)^2} \tag{3.33}$$

and

$$k^2a_-^2 = \frac{[x_2' - \alpha_+ k(x_1 - a)]^2}{(\alpha_+ - \alpha_-)^2} + Q_-^2 \frac{(\alpha_+ x_1' + Q_+^2 kx_2)^2}{(\alpha_+ Q_-^2 - \alpha_- Q_+^2)^2}. \tag{3.34}$$

4. Transverse adiabatic invariants

The effective beam volume in phase space is measured in terms of action variables, or adiabatic invariants $I_\pm$, which are canonically conjugate with the oscillation phases $\psi_\pm$. The action variables are proportional to squared amplitudes:

$$I_\pm = \frac{1}{2}\beta\gamma kQ_\pm a_\pm^2 \cdot R_\pm, \tag{3.35}$$

where we have introduced the coefficients $R_\pm(E)$. To find them, one can use the canonical relationships (see the Appendix)

$$\frac{\partial}{\partial E} I_\pm(\vec{P}_\perp, \vec{\rho}, E) = -\frac{\partial}{\partial \psi_\pm} t(I_\pm, \psi_\pm), \tag{3.36}$$

where the energy ($-E$) and time (t) are considered as one of three "old" canonical pairs, together with $\vec{p}_\perp$ and $\vec{\rho}$ (while the z coordinate is treated as the "time argument"). To determine the time t as function of "new" variables

$(a_\pm, \psi_\pm)$, one has to integrate the equation

$$t' = \frac{1}{\beta_z}$$

along a "solved" particle trajectory. In linear approximation for free particle oscillations near the helical orbit $\vec{a}(p, z)$, we have (see the Appendix)

$$t = \hat{t} + \frac{\kappa}{\beta\sqrt{1+\kappa^2}}\left[\frac{1+\alpha_+}{Q_+}a_+ \sin\psi_+ + \frac{1+\alpha_-}{Q_-}a_- \sin\psi_-\right],$$
$$\hat{t}' = \text{const}, \tag{3.37}$$

where we have introduced a "shortened time" $\hat{t}$ as a new canonical variable conjugate to the energy, $-E$. Using the relationships (3.32) and (3.37), the shortened time can be expressed as a function of initial variables:

$$\hat{t} = t + \frac{1}{\beta\sqrt{1+\kappa^2}}\left[Dx_1' + \left(1 - \frac{q-1}{1+\kappa^2}\hat{D}\right)\kappa x_2\right]. \tag{3.38}$$

Note that the rate $\hat{t}$ changes is constant on a particle trajectory in a magnetic field.

Returning to the derivatives $\frac{\partial a_\pm^2}{\partial E}$, they can be found using the relationships in (3.35)–(3.37), in which the variables of the rotating frame (x_1, x_1', x_1, x_2') are to be considered as functions of (x, p_x), (y, p_y) and energy E. The calculation in the Appendix gives

$$\frac{\partial}{\partial E}a_\pm^2 = \mp\frac{2a(1+\kappa^2)}{e\beta^2}\frac{1+\alpha_\pm}{\alpha_\pm}\alpha_\pm \cos\psi_\pm. \tag{3.39}$$

Using Eqs. (3.35)–(3.37) gives

$$R_\pm = \pm\frac{\alpha_\pm}{(1+\kappa^2)^{3/2}}\frac{\alpha_+ - \alpha_-}{Q_\pm^2}. \tag{3.40}$$

Thus solutions and relationships (3.31)–(3.40) provide a full set of canonical transformations from the initial variables $(\vec{p}, \vec{r})$ to action and phase variables in a magnetic field before a rf field has been introduced.

5. Beam envelopes on a helical orbit

In the rotating frame of the helical orbit, each of the two normal mode oscillations is recognized in transverse space as an elliptical orbit with tune Q_+ or Q_- [see Eq. (3.27)]:

$$\left|\begin{array}{c} u_1 \\ u_2 \end{array}\right|_+ = a_+ \left|\begin{array}{c} \cos\psi_+ \\ (\alpha_+/Q_+)\sin\psi_+ \end{array}\right|,$$
$$\left|\begin{array}{c} u_1 \\ u_2 \end{array}\right|_- = a_- \left|\begin{array}{c} \cos\psi_- \\ (\alpha_-/Q_-)\sin\psi_- \end{array}\right|. \tag{3.41}$$

With random phase distributions, there are two normal beam ellipsoids of aspect ratios

$$\left(\frac{\sigma_1}{\sigma_2}\right)_+ = \frac{Q_+}{\alpha_+}, \qquad \left(\frac{\sigma_1}{\sigma_2}\right)_- = \frac{Q_-}{\alpha_-}. \tag{3.42}$$

For ensembles with adiabatic invariants $I_\pm$, one can average over $\psi_\pm$ to find the related sizes σ_1 and σ_2:

$$(\sigma_1)_\pm^2 = \pm\frac{I_\pm Q_\pm}{\gamma\beta k\alpha_\pm(\alpha_+ - \alpha_-)},$$
$$(\sigma_2)_\pm^2 = (\sigma_1)_\pm^2\left(\frac{\alpha_\pm}{Q_\pm}\right)^2. \tag{3.43}$$

Thus, σ_1 and σ_2 rms sizes can be explicitly found as determined by the two canonical (and uncorrelated) emittances ε_+ and ε_- by substituting for $I_\pm$ with $\langle I_\pm\rangle = \varepsilon_\pm$ into (3.43) and adding a contribution due to energy spread:

$$\sigma_1^2 = D^2\left(\frac{\Delta p}{p}\right)^2 + (\sigma_1)_+^2 + (\sigma_1)_-^2,$$
$$\sigma_2^2 = (\sigma_2)_+^2 + (\sigma_2)_-^2. \tag{3.44}$$

The canonical emittances $\varepsilon_\pm$ will not be disturbed by an adiabatic change of beam optics parameters along the beam path in the helical transport line. These uncorrelated emittances (i.e., the averaged values of adiabatic or generalized Courant-Snyder invariants) also can be conserved in transfers from the helical channel to sections with different optics, such as a conventional alternating gradient transport with uncoupled planes. However, special optics will be needed to match such a transition in order to avoid an increase of beam emittances.

F. Longitudinal oscillations in a rf field

A rf field has to be applied to compensate for energy loss in an absorber to achieve substantial ionization cooling. Thus the beam must first be captured and bunched before the cooling described in this paper can be accomplished. The capture and bunching processes will be described in a paper to follow this one. In this section we introduce the basic characteristics of longitudinal dynamics of particles in a bunched beam subject to a rf field on a helical beam path without absorber.

1. Basic equations

Longitudinal motion of particles in a rf field is governed by equations for energy E and time t as a pair of canonically conjugate variables, with the z coordinate considered a time argument and the rf wave number k_{rf} expressed in terms of the rf cavity resonant frequency and particle longitudinal velocity,

$$k_{\text{rf}} \approx \omega/\beta_z.$$

Assuming, as usual, that the change of particle energy along one period of magnetic and electric field and "betatron" oscillations is small, we can express the equations in terms of energy and shortened or average time t, given by Eqs. (3.37) and (3.38). A convenient variable is a reference time

$$\tau = \hat{t} - (k_{\text{rf}}/\omega)z. \tag{3.45}$$

Note that the rate of change of $\hat{t}$ as a function of z is not influenced by particle transverse oscillations in a focusing magnetic field. Neglecting the phase $\omega\tau$ and the rate of change of energy on transverse amplitudes, we obtain the shortened canonical equations

$$\gamma' = -\gamma'_{\max}\sin\omega\tau = -\frac{\partial}{\partial\tau}H_S \tag{3.46}$$

and

$$\tau' = \frac{1}{\beta}\sqrt{1+\kappa^2} - \frac{k_{\rm rf}}{\omega} = \frac{\partial}{\partial\gamma}H_S, \tag{3.47}$$

where

$$H_S = \int\left(\frac{1}{\beta}\sqrt{1+\kappa^2} - \frac{k_{\rm rf}}{\omega}\right)d\gamma - \frac{\gamma_{\max}}{\omega}\cos\omega\tau \tag{3.48}$$

is the effective longitudinal or synchrotron Hamiltonian, and $\gamma'_{\max}$ is the maximum rate of energy change due to the rf field.

The Hamiltonian and Eqs. (3.46) and (3.47) determine the equilibrium phase $\omega\tau = 0$, the equilibrium or resonance energy $\gamma_{\rm res}$, such that

$$\left(\frac{1}{\beta}\sqrt{1+\kappa^2}\right)_{\gamma=\gamma_{\rm res}} = \frac{k_{\rm rf}}{\omega}, \tag{3.49}$$

and the phase space trajectory of particle oscillations around the equilibrium orbit where

$$H_S(\gamma,\tau) = \text{const.} \tag{3.50}$$

2. Translational mobility of a particle on a helical path

For a particle of energy $E = m\gamma$, the rate of change of phase is given in linear approximation by

$$\hat{\tau}' = \eta(\gamma - \gamma_{\rm res}) \equiv \eta\Delta\gamma, \tag{3.51}$$

where we have introduced a new parameter, η, the translational mobility:

$$\eta = \frac{d}{d\gamma}\frac{\sqrt{1+\kappa^2}}{\beta} = \frac{\sqrt{1+\kappa^2}}{\gamma\beta^3}\left(\frac{\kappa^2}{1+\kappa^2}\hat{D} - \frac{1}{\gamma^2}\right). \tag{3.52}$$

This parameter is analogous to the momentum slip factor in a synchrotron, where the factor $\frac{\kappa^2}{1+\kappa^2}\hat{D}$ can be identified with $\frac{1}{\gamma_T^2}$.

3. Synchrotron tune

The rate of change of energy for a particle with phase $\omega\tau$ is given in linear approximation by

$$\Delta\gamma' = -\gamma'_{\max}\omega\tau. \tag{3.53}$$

Equations (3.51) and (3.53) determine the synchrotron tune, the frequency of phase and energy oscillations near the equilibrium where $\tau = 0$ and $\gamma = \gamma_{\rm res}$:

$$\tau'' + \omega^2 Q_S^2\tau = 0 \quad \text{and} \quad Q_S^2 = \eta\gamma'_{\max}/\omega. \tag{3.54}$$

4. Synchrotron adiabatic invariant, canonical phase, and admittance

The adiabatic invariant of oscillations about the equilibrium is determined as an area in phase space bounded by the ellipse given by Eq. (3.50):

$$I_S = \frac{1}{2\pi}\oint\Delta\gamma d\tau. \tag{3.55}$$

For a small oscillation near the equilibrium, I_S is proportional to the Hamiltonian function:

$$I_S \approx \frac{H_S}{\omega Q_S} = \frac{\eta}{2\omega Q_S}(\Delta\gamma)^2 + \frac{\omega Q_S}{2\eta}\tau^2. \tag{3.56}$$

More generally, there is the relationship

$$dH_S = \omega Q_S(I_S)dI_S,$$

with $Q_S(I_S)$ as the amplitude-dependent synchrotron frequency that takes into account the nonlinear behavior of the rf field as a function of phase $\omega\tau$. A canonical variable conjugate to the synchrotron invariant I_S is the synchrotron phase Ψ_S, which varies uniformly on an unperturbed orbit:

$$\Psi'_S = \omega Q_S(I_S). \tag{3.57}$$

The maximum I_S value for captured particles, the admittance, corresponds to oscillations near the synchrotron separatrix:

$$H_S = \frac{\gamma_{\max}}{\omega} \quad \text{and} \quad (I_S)_{\rm adm} = \frac{2}{\pi\omega}\sqrt{\frac{\gamma'_{\max}}{\eta\omega}}. \tag{3.58}$$

On the separatrix trajectory, the frequency Q_S is zero because the motion stops at the points $\omega\tau = \pm\pi$.

IV. COOLING DECREMENTS

A. Absorber drag force

Muons passing through an absorber experience energy and momentum loss due to collisions with electrons. The collision effect averaged over impact parameters is described by the well-known formula for the drag force:

$$\dot{\vec{p}} = \frac{-F\vec{p}}{p}, \qquad F = \frac{4\pi Zne^4\log}{m_e\beta^2}, \tag{4.1}$$

where Z and n are the absorber atomic number and concentration, m_e the electron mass, and β the muon velocity. Here log is a symbol for the Coulomb logarithm of ionization energy loss for fast particles:

$$\log \equiv \ln\left(\frac{2p^2}{h\nu m_\mu}\right) - \beta^2, \tag{4.2}$$

with $h\nu$ the effective ionization potential [27]. A typical

magnitude of the log is about 12 for the conditions described below.

Similar to the radiation force for relativistic electrons in a magnetic field, the drag force produces a damping effect on muon transverse oscillations in a focusing field:

$$\vec{p}\,'_{\perp} = -\Lambda_0 \vec{p}_{\perp}, \qquad \Lambda_0 = \frac{F}{\gamma\beta^2 m_\mu}.$$

Unlike the radiation force, however, the drag force cannot damp the beam energy spread since its characteristic energy dependence, dF/dE, is negative or is too small when it is positive ($\gamma^2 > \log$):

$$E' = -F(E), \qquad \Delta E' = -(dF/dE)\Delta E,$$
$$(dF/dE) = 2\Lambda_0\left[-\frac{1}{\gamma^2} + \frac{1-(\beta/\gamma)^2}{\log}\right]. \tag{4.3}$$

To achieve longitudinal cooling requires emittance exchange with transverse oscillations as discussed in Sec. II. Emittance exchange, in turn, requires the introduction of a beam bend that creates dispersion, a correlation between the orbit and energy of a particle. Use of a continuous homogeneous absorber, rather than wedges at discrete points, implies a positive dispersion along the entire cooling path, a condition that we have shown exists for an appropriately designed helical dipole channel. We have also shown that this condition is compatible with stable periodic orbits.

The linear theory of the damping process including wedge effects was developed earlier [15] and later applied and developed in some detail for a homogenous absorber [17]. The treatment in this paper follows the analysis in these previous works but includes more detail. Below we will calculate the longitudinal and transverse damping rates along a helical transport line in a homogeneous absorber with rf fields. As an example of how the cooling rates can be manipulated, we will then indicate how to achieve balanced 6D cooling, where the three decrements are equal.

B. Longitudinal decrement

1. Synchrotron oscillations in the absorber

Energy loss due to muon collisions with absorber electrons can be included after averaging over collision parameters and transverse oscillations about the energy-dependent helical orbit:

$$\gamma = -\gamma'_{\max}\sin\omega\tau - \frac{F}{m_\mu}\sqrt{1+\kappa^2}. \tag{4.4}$$

Expanding energy loss in a linear approximation as a function of energy near the reference orbit, we obtain synchrotron oscillation equations

$$\Delta\gamma' = -\gamma'(\sin\omega\tau - \sin\omega\tau_{eq}) - \Lambda_\gamma\Delta\gamma, \tag{4.5}$$

where

$$\gamma'_{\max}\sin\omega\tau_{eq} = -\frac{F}{m_\mu}\sqrt{1+\kappa^2}\,\Big|_{\gamma=\gamma_{\rm res}}, \tag{4.6}$$

and we have introduced the energy decrement as

$$\Lambda_\gamma = \frac{d}{d\gamma}\frac{\langle F\rangle}{m_\mu}\sqrt{1+\kappa^2}$$
$$= \left[-\frac{2}{\gamma^2} + \frac{2[1-(\beta/\gamma)^2]}{\log} + \hat{D}\frac{\kappa^2}{1+\kappa^2}\right]\Lambda_0. \tag{4.7}$$

For positive Λ_γ, synchrotron oscillations will damp with a characteristic exponent Λ_γ. Note that the synchrotron oscillations in the absorber may last some time since

$$\Lambda_\gamma \ll \omega Q_S, \tag{4.8}$$

where $Q_S^2 = \eta\omega\gamma'_{\max}\cos\omega\tau_{eq}$.

The relationship (4.8) follows from the condition $\gamma' \ll \omega\gamma_{\rm res}$, taking into account that $\Lambda \sim \gamma'_{\max}/\gamma_{\rm res}$ unless the translational mobility parameter η is very small. Consequently we can continue to treat the phase $\omega\tau$ and energy motion in terms of oscillations even though the reduction in the synchrotron potential well might not be small ($F \le m\gamma'$). We can characterize the oscillations by a modified synchrotron adiabatic invariant as determined by the integral in (3.55), but with a Hamiltonian

$$\hat{H} = \frac{\eta}{2}(\Delta\gamma)^2 - \gamma'_{\max}(\cos\omega\tau + \omega\tau\sin\omega\tau_{eq})/\omega.$$

Damping due to an emittance exchange mechanism can then be considered a slow process.

2. Synchrotron oscillation decrement

Under condition (4.8) one can calculate the damping rate of I_S using a perturbative method. Considering the adiabatic invariant a function of $\Delta\gamma$ and $\omega\tau$ we find the instantaneous and average rates of change of the adiabatic invariant:

$$I'_S = -\frac{\partial I_S}{\partial\gamma}\Lambda_\gamma\Delta\gamma.$$

Using the canonical relationship $\frac{\partial I_S}{\partial\gamma} = \frac{\partial\tau}{\partial\Psi_S}$ and taking into account that

$$\tau' = \frac{\partial\tau}{\partial\Psi_S}\Psi'_S = \frac{\partial\tau}{\partial\Psi_S}\omega Q_s(I_S),$$

we find a simple damping equation:

$$\langle I'_S\rangle = -\Lambda_\gamma\oint\Delta\gamma d\tau/2\pi = -\Lambda_\gamma I_S. \tag{4.10}$$

Note that the linear reduction of the Hamiltonian has not been used in this derivation. Thus in the approximation of a constant energy decrement as in (4.5), the nonlinearity of synchrotron oscillations does not affect the cooling rate.

Note, finally, that the instantaneous rate of change of phase $\omega\tau$ is influenced by the transverse component of the drag force ($\sim x_1'$) according to Eq. (3.38), but the average effect is zero:

$$\langle \tau \delta\tau' \rangle \sim \left\langle \tau \frac{\partial \hat{t}}{\partial x_1'} x_1' \right\rangle = 0.$$

C. Transverse decrements

To derive the transverse rates, we have to calculate the average partial power $\langle I_\pm' \rangle$. This can be easily done considering $I_\pm$ as functions of transverse vector momentum $\vec{p}_\perp$, coordinate $\vec{\rho}$, and energy $E = m\gamma$:

$$I_\pm' = \frac{1}{\beta_z} \frac{\partial I_\pm}{\partial \vec{p}_\perp} \vec{F}_\perp + \frac{\partial I_\pm}{\partial \gamma} \cdot \gamma', \tag{4.11}$$

with

$$\begin{aligned} \vec{F}_\perp &= -F \cdot \frac{\vec{\beta}_\perp}{\beta} = -F \frac{\vec{p}' \beta_z}{\beta}, \\ \gamma' &= -\frac{F}{m_\mu} \sqrt{1 + (\vec{p}')^2}. \end{aligned} \tag{4.12}$$

We avoid the derivation of the expressions $I_\pm(\vec{p}_\perp, E, \vec{\rho}, z)$; instead, we use the canonical relationships shown in the Appendix, Eqs. (A6) and (A7), then

$$I_\pm' = -F \left[\frac{1}{\beta} \vec{p}' \frac{\partial \vec{\rho}}{\partial \psi_\pm} - \frac{\partial t}{\partial \psi_\pm} \sqrt{1 + (\vec{p}')^2} \right]. \tag{4.13}$$

Thus, we can simply use the solutions in (3.27) and (3.37) in order to perform averaging over the phases $\psi_\pm$. Note that

$$\begin{aligned} \vec{p}' \frac{\partial \vec{\rho}}{\partial \psi_\pm} &= \mathrm{Re}\left(\hat{x}' \frac{\partial \hat{x}^*}{\partial \psi_\pm} \right) \quad \text{and} \\ \sqrt{1 + (\vec{p}')^2} &\approx \sqrt{1 + \kappa^2} + \frac{\kappa}{\sqrt{1 + \kappa^2}} (k u_1 + u_2'). \end{aligned} \tag{4.14}$$

The force F has to be taken as shown in (4.12). The term on the right-hand side of the equations in (4.11) after averaging over $\psi_\pm$ becomes proportional to $a_\pm^2$ [see Eq. (3.27)], i.e., the cooling decrements can be defined:

$$\langle I_\pm' \rangle = -\Lambda_\pm I_\pm,$$

taking into account (3.35). Performing the averaging, we find

$$\begin{aligned} \frac{\Lambda_\pm}{\Lambda_o} = \pm \frac{1 + \kappa^2}{(\alpha_+ - \alpha_-)\alpha_\pm} \Big[& 2\alpha_\pm + \alpha_\pm^2 + Q_\pm^2 \\ & - \frac{\kappa^2}{1 + \kappa^2} (1 + \alpha_\pm)^2 \Big]. \end{aligned} \tag{4.15}$$

Taking into account relationships in (3.28) and (3.29), we find the sum of transverse decrements:

$$\frac{\Lambda_+ + \Lambda_-}{\Lambda_o} = 2 - \frac{\kappa^2}{1 + \kappa^2} \hat{D}. \tag{4.16}$$

Combining all the three decrements, we find

$$\begin{aligned} \Lambda_+ + \Lambda_- + \Lambda_\gamma &= 2\Lambda_o \left(\beta^2 + \frac{1}{2} \frac{p}{\log} \frac{\partial \log}{\partial p} \right) \equiv \Lambda \\ &= 2\Lambda_0 \hat{\beta}^2, \end{aligned} \tag{4.17}$$

where we have introduced the parameter

$$\hat{\beta} = \sqrt{\beta^2 + \frac{1}{2} \frac{p}{\log} \frac{\partial \log}{\partial p}} = \sqrt{\beta^2 + \frac{1 - (\beta/\gamma)^2}{\log}}, \tag{4.18}$$

although in the following we will not distinguish between $\hat{\beta}$ and β, assuming

$$\beta^2 \gg \frac{1}{2} \frac{p}{\log} \frac{\partial \log}{\partial p}.$$

This result (4.17) agrees with the *dissipation theorem* [28–30]:

$$\sum_{\alpha=1}^{3} \Lambda_\alpha = -\left\langle \frac{1}{\beta_z} \frac{\partial}{\partial \vec{p}} \vec{F}(\vec{p}, \vec{r}) \right\rangle.$$

The distribution of the two transverse cooling rates is characterized by the difference $\Lambda_+ - \Lambda_-$. Using the definitions $\alpha_\pm$, etc., we obtain

$$\frac{\Lambda_+ - \Lambda_-}{\Lambda_o} = \frac{1}{\sqrt{R^2 - G}} [q^2 - 1 + \kappa^2 (R\hat{D} - 1)] \frac{1}{1 + \kappa^2}. \tag{4.19}$$

D. Equating the cooling decrements

If the three cooling decrements are equal,

$$\Lambda_\gamma = \Lambda_+ = \Lambda_- = \Lambda/3,$$

then

$$\hat{D} = 2 \frac{1 + \kappa^2}{\kappa^2} \left(1 - \frac{2}{3} \beta^2 \right) \tag{4.20}$$

and

$$q \equiv \frac{k_c}{k} - 1 = \beta \sqrt{\frac{1 + \kappa^2}{3 - \beta^2}}. \tag{4.21}$$

As follows from Eq. (3.14), conditions (4.20) and (4.21) also determine the effective field index g as a function of κ and β:

$$g = -\frac{1 - \kappa^2}{1 + \kappa^2} \sqrt{\frac{1 + \kappa^2}{3 - \beta^2}} + \frac{\kappa^2}{2(1 + \kappa^2)} \frac{4\beta^2 - 3}{3 - 2\beta^2}. \tag{4.22}$$

Condition (4.21) indicates the necessity of sufficiently strong solenoidal and dipole fields according to

Eqs. (3.11) or (3.13), while condition (4.22) determines the quadrupole strength.

The balanced cooling area in terms of parameters κ and β can be limited by the dynamical stability condition (3.24), which can be rewritten as

$$0 < \left[\beta\left(\frac{1+\kappa^2}{3-\beta^2}\right)^{1/2} + \kappa^2\frac{\frac{3}{4}-\beta^2}{3-2\beta^2}\right] < \left(\frac{(1+\kappa^2)^2}{4\kappa^2}\,\frac{(1-\frac{2}{3}\beta^2)}{(1-\frac{1}{3}\beta^2)^2}\right). \tag{4.23}$$

In the region $\beta^2 < 3/4$, the periodic orbit seems to appear stable at any κ value, although for $\beta^2 > 3/4$ condition (4.21) also leaves the beam stable in a wide range of $\kappa < 1$. Note, however, that if κ is too small then the beam stability is worse, as can be seen from the formula for the oscillation tune Q_-,

$$Q_- \approx \sqrt{G/2R} \approx \kappa\left(\frac{\sqrt{3-\beta^2}}{3-2\beta^2}\,\beta\right)^{1/2}. \tag{4.24}$$

V. EQUILIBRIUM EMITTANCES

A. Scattering and straggling

Besides the average ionization energy loss when moving through the absorber, each muon exchanges momentum with the atoms of the absorber, both in direction and magnitude. The average angular scattering from absorber nuclei and electrons is

$$\frac{d\theta_{sc}^2}{dz} = \frac{Z+1}{\gamma\beta^2}\,\frac{m_e}{m_\mu}\,\Lambda. \tag{5.1}$$

The spread about the average energy loss is effectively only caused by collisions with electrons, because of the large nucleon mass relative to the electron mass:

$$\frac{d}{dz}(\delta\gamma)^2 = \frac{\gamma\beta^2}{4\log}(\gamma^2+1)\frac{m_e}{m_\mu}\,\Lambda. \tag{5.2}$$

It is well known that the momentum or energy spread does not include the factor of the Coulomb log since it is determined characteristically by interactions with the maximum momentum transfer. The contribution of low momentum transfer collisions to energy diffusion appears insignificant, contributing at most to angular scattering and energy loss. Correspondingly, the energy straggling grows rapidly with the Lorentz factor of the muon beam.

B. Longitudinal equilibrium emittance, energy spread, and bunch length

The equilibrium synchrotron emittance results from the balance between damping and growth rates due to both energy straggling and angle scattering. In the vicinity of the reference orbit, the adiabatic invariant can be represented as a quadratic function of energy deviation from the equilibrium value and reference time τ as shown in (3.56). Then the diffusion growth rate of I_S can generally be found as

$$(I_S')_d = \frac{\eta}{2\omega Q_S}\,\frac{d}{dz}(\delta\gamma)^2 + \frac{\omega Q_S}{2\eta}\,\frac{d}{dz}(\delta\hat{t})^2, \tag{5.3}$$

where the straggling rate is given by Eq. (5.2). The diffusion rate of $\hat{t}$ can be found using Eq. (3.38) taking into account the continuity of the total phase, $\omega t - k_{\rm rf} z$, in a collision,

$$\frac{d}{dz}(\delta\hat{t})_{sc}^2 = \frac{D^2}{2\beta^2(1+\kappa^2)}\,\frac{d}{dz}\theta_{sc}^2, \tag{5.4}$$

with the angle scattering rate as given by (5.1).

Applying the Langevin balance equation [31],

$$I_S' = -\Lambda_\gamma I_S + (I_S')_d,$$

we obtain the normalized equilibrium synchrotron emittance:

$$\varepsilon_S \equiv \langle I_S\rangle_{eq} = (I_S')_d/\Lambda_\gamma = \frac{\Lambda}{4\Lambda_\gamma}\,\frac{m_e}{m_\mu}\,\gamma\beta^2\left[\frac{\eta}{\omega Q_S}\,\frac{\gamma^2+1}{2\log} + \frac{Z+1}{\gamma^2\beta^6}\,\frac{\omega Q_S}{\eta k^2}\,\frac{\hat{D}^2\kappa^2}{1+\kappa^2}\right]. \tag{5.5}$$

The first term in the brackets in (5.5) corresponds to energy straggling and the second term is due to ωt diffusion due to scattering.

Now, knowing the equilibrium emittance, one can easily determine the equilibrium energy spread and bunch length, relying on Eq. (3.56):

$$\langle(\Delta\gamma)^2\rangle = \frac{\omega Q_S}{\eta}\,\varepsilon_S \quad\text{and}\quad \langle\tau^2\rangle = \frac{\eta}{\omega Q_S}\,\varepsilon_S. \tag{5.6}$$

C. Equilibrium transverse emittances

In order to calculate the scattering rates of transverse emittances, one can use the general expressions (3.33)–(3.35) and (3.40), where the helix radius a is a function of total momentum p. Both the angle and energy scattering will contribute to the growth of transverse amplitudes. Calculating the growth rate due to momentum jumps along the x_2 direction, we have to take into account that this axis is not perpendicular to the particle total momentum direction, but makes an angle with it whose tangent is $\kappa = p_\perp/p_z$; thus we find

$$k^2(a_\pm^2)_{sc}' = \frac{1/(1+\kappa^2)}{(\alpha_+-\alpha_-)^2}\left\{\frac{1}{2}\left[1+\frac{Q_\pm^2}{\alpha_\pm^2}(1+\kappa^2)^3\right]\frac{d\theta_{sc}^2}{dz} + \frac{\kappa^2}{\gamma^2\beta^4}[1+\sqrt{1+\kappa^2}\hat{D}\alpha_\mp]^2\,\frac{d}{dz}(\delta\gamma)^2\right\}. \tag{5.7}$$

Applying Langevin's balance equations

$$a_{\pm}^2 = -\Lambda_{\pm} a_{\pm}^2 + (a_{\pm}^2)'_{sc}, \tag{4.8}$$

we find the following expressions for the equilibrium normalized transverse emittances:

$$\langle I_{\pm} \rangle = \varepsilon_{\pm} = \frac{\Gamma_{\pm}}{4kQ_{\pm}} \frac{m_e}{m_{\mu}\beta} \frac{\Lambda/\Lambda_{\pm}}{(1+\kappa^2)^{5/2}}, \tag{5.9}$$

where

$$\Gamma_{\pm} \equiv \frac{(Z+1)[\alpha_{\pm}^2 + (1+\kappa^2)^3 Q_{\pm}^2] + \kappa^2[\alpha_{\pm} - (1+\kappa^2)^{3/2}]^2(\gamma^2+1)/2 \log}{\alpha_{\pm}^2 + (1+\kappa^2)\hat{D}^{-1}}.$$

VI. NUMERICAL EXAMPLE OF A HELICAL CHANNEL

Table I shows a numerical example of a helical cooling channel using the equations derived in earlier sections. The beam momentum of 100 MeV/c is low compared to the 200 MeV/c of earlier studies in order to attain the best transverse and longitudinal equilibrium emittances as well as to shorten the beam path and reduce the integrated energy loss in the absorber. A rather tight helix ($\kappa \approx 1$) has been chosen in this calculation to moderate the dispersion required for balanced cooling. Lower dispersion improves beam stability and reduces the contribution of energy spread to the radial beam size, the straggling contribution to equilibrium transverse emittances due to dispersion (to about 6%), and the angle scattering contribution to the longitudinal emittance (to 33%). Note that the calculated 6D emittance may not be a minimum, although

TABLE I. Estimated parameters of a helical 6D cooling channel.

Parameter	Unit	Initial	Middle[d]	Final
Beam momentum, p[a]	MeV/c	100	100	100
Solenoid field, B	T	3.5	8	14
Cyclotron wavelength, $\lambda_c = 2\pi/k_c$[a]	m	0.60	0.26	0.14
Helix period, $\lambda = 2\pi/k$	m	1	0.44	0.22
Helical magnet inner radius	cm	30	12	7
Transverse field at magnet coil	T	1.7	4.2	7.0
Transverse field at beam center	T	0.7	1.6	3.0
Helix quadrupole gradient	T/m	1.2	7.5	20
Helix orbit radius, a[a]	cm	15	6	3
Dispersion, D	cm	37	15	7.5
Transverse tunes, Q_+/Q_-		0.94/0.57	0.94/0.57	0.94/0.57
Transverse beta functions, β_+/β_-	cm	16/26	6/10	3.2/5.2
Accelerating rf field amplitude	MV/m	40	40	40
Frequency, $f = \omega/2\pi$	GHz	0.2	0.8	1.6
Absorber energy loss rate dE/ds	MeV/m	14	14	14
6D cooling decrement length, Λ^{-1}	m	4	4	4
Individual decrement lengths	m	12	12	12
Synchrotron beta function, β_s	m	0.95	0.47	0.32
Synchrotron tune, $Q_s = 1/\omega\beta_s$		0.25	0.12	0.08
Synchrotron admittance, I_a	cm	3.0	0.37	0.14
Synchrotron emittance, ε_S	cm	1.5[b]	0.15[b]	3×10^{-2}[c]
Relative momentum spread	%	7.5[b]	3[b]	2[c]
Bunch length	cm	30[b]	7.5[b]	1.1[c]
Beam width, Δa	cm	3[b]	0.56[b]	0.15[c]
Transverse emittances, $\varepsilon_+/\varepsilon_-$	cm rad	1.7/1.7[b]	0.2/0.2[b]	$(1/3) \times 10^{-2}$[c]
Beam widths, σ_1/σ_2	cm	8/5[b]	1.8/1.1[b]	0.45/0.28[c]

[a]Reference orbit.
[b]Maximum deviation from reference orbit.
[c]rms equilibrium value.
[d]At the beginning of the 0.8 GHz section.

further optimization has yet to improve the estimated equilibrium values significantly. The cooling effect in this calculation in terms of reduction of the 6D emittance is 5×10^5. The total energy loss in the absorber is about 1.12 GeV. For a channel of continuous dense hydrogen gas with 14 MeV/m of energy loss, this implies a 6D cooling channel length, $L = \frac{1.12}{0.014}/\sqrt{1+\kappa^2} = 56$ m.

VII. DISCUSSION

The initial low momentum muon beam with relatively small momentum spread (7.5%) in the example above could be obtained using a short helical channel with an absorber but no rf. This possibility was proposed and treated previously [17]. Using emittance exchange in this precooling helical channel, all the cooling power of the absorber (with or without wedges) can be taken from the transverse coordinates and concentrated on the longitudinal one to cool the energy spread. Maintaining the transverse emittances, or even by allowing some increase in them for more reduction of energy spread, it is possible to decrease the absolute energy spread a factor of 10 or more before the bunch length is increased significantly. Then, the beam can be captured and bunched by a rf field and injected into the basic cooling channel described by Table I. In this way, the total 6D emittance reduction factor could exceed 10^6. The estimated length of such a deceleration and capture section is less than 25 m.

The example channel assumes smaller, higher-frequency rf cavities will be used when the beam dimensions have been cooled enough to allow them. Reduced transverse dimensions imply that the desired strength of the magnetic fields would be easier to achieve. Higher frequencies make it easier to achieve the desired rf gradients. Short adiabatic helical transition sections would be used to match one stage to the next.

In order to optimize the rf cavity acceptance, each cavity axis could be centered on and aligned with the periodic orbit as the beam wound around the axis of the solenoid, perhaps with the rf waveguides passing through the gap in the helical dipole coil. The large aperture magnets and rf cavities for the 200 MHz stage may be a serious technical challenge and future studies will be toward replacing the initial stage with precooling sections to reduce the beam size. The precooling under consideration involves transverse cooling with a helical quadrupole section and longitudinal cooling in a short helical dipole section without rf.

The estimated cooling channel length of 56 m for a bunched muon beam of 100 MeV/c assumes that the channel contains rf cavities that operate while filled with dense hydrogen gas. At 50 atm and 77 K, hydrogen gas density is about 21.5% of liquid hydrogen and the corresponding dE/ds for muons with 100 MeV/c momentum, or 46 MeV kinetic energy, is about 14 MeV/m. In this case, the rf cavities must provide sufficient gradient to compensate for $\frac{dE}{dz} = \frac{dE}{ds}\sqrt{1+\kappa^2} = 20$ MeV/m energy loss and provide sufficient rf bucket area for longitudinal beam stability. Thus an average accelerating gradient of around 40 MeV/m is required.

The project by Muons, Inc. and IIT presently underway at Fermilab to develop high-gradient pressurized rf cavities is designed to explore the use of hydrogen and helium gas up to more than 100 atm pressure at temperature down to 77 K. Surface gradients of 80 MV/m for stable operation have been achieved at 800 MHz with 20 μs pulses in hydrogen at 17 atm at liquid nitrogen temperature using molybdenum electrodes. Scaling from the measured Paschen curve data from Lab G, hydrogen gas itself at 50 atm and 77 K will support gradients up to 330 MV/m. Future proof-of-principle tests include operation in strong magnetic fields and in intense ionizing radiation. Providing sufficient power is also a necessary condition for high-gradient cavities. A scheme has been investigated that implies that 50 MV/m could be generated at 200 MHz using cold copper pillbox cavities for the short pulses required for a neutrino factory or muon collider using pulse compression techniques [32,33].

A cooling channel based on the use of helical magnets and a continuous homogeneous absorber offers advantages compared to other designs. One important advantage is that the cooling system can be described relatively simply with a time-independent, beam-path-independent Hamiltonian that does not depend on z. Thus the stability and evolution of the beam as it cools can be understood using well-established analytical linear and perturbative nonlinear techniques. The next steps in the development of the concepts presented here include simulations to verify the linear and nonlinear aspects of the beam dynamics and to continue the experimental investigations to the point that a complete, realistic 6D cooling channel can be designed, prototyped, and built. This concept and particular example are being developed and simulated by Muons, Inc. and the Thomas Jefferson National Accelerator Facility [34]. A description of the project and a preliminary exposition of the ideas presented in this paper were first reported in [35].

VIII. CONCLUSIONS

A magnetic channel filled with continuous absorber without special edge shaping can be used for emittance exchange cooling of the 6D emittance of a muon beam. This is true for any magnetic arrangement where higher momentum corresponds to a longer path length in a homogeneous absorber and therefore larger ionization energy loss.

The dynamical properties of an attractive example of such a channel have been investigated in some detail, where a solenoidal field is combined with a helical field to provide superior 6D cooling. The continuous nature of the magnetic fields and their helical invariance allows periodic orbits to be found and their stability and cooling properties to be completely analyzed. We have shown that

a continuous, homogenous absorber using high-gradient hydrogen-gas-filled rf cavities could provide exceptional 6D cooling in a rather short channel.

Six-dimensional cooling using a homogeneous absorber may be a way to achieve the beam brightness needed for a muon collider. If engineering studies and simulations bear out this prediction, the case for a muon collider as a future energy frontier machine will be strengthened.

Recent discoveries have made a neutrino factory an attractive physics opportunity. The 6D cooling suggested here could provide a neutrino factory with superior performance and reduced costs.

ACKNOWLEDGMENTS

We are pleased to thank Dr. Boyce, Dr. Chattopadhyay, Dr. Dylla, Dr. Leemann, and Dr. Merminga of Thomas Jefferson National Accelerator Facility for the opportunity to continue this research and to investigate with simulations and further analytic calculations the validity of the proposals suggested here. We thank Dr. A. Bogacz and Dr. K. Yonehara for helpful comments. We also thank S. Derbeneva and L. Even for help in preparing the manuscript. Thomas Jefferson National Accelerator Facility is operated by the Southeastern Universities Research Association, Inc. under U.S. Department of Energy Contract No. DE-AC05-84ER40150. Muons, Inc. is supported in part by SBIR Grant No. DE-FG02-03ER83722.

APPENDIX: HAMILTONIAN FRAMEWORK AND CANONICAL RELATIONSHIPS

Hamilton's method provides some important relationships of beam dynamics in a magnetic field (or a stationary electromagnetic field). It is based on the introduction of a Hamiltonian with corresponding equations of motion. An ordinary Hamiltonian form is the energy function

$$\hat{E} = \sqrt{p^2 + m^2} + A_o = \sqrt{(\vec{P} - \vec{A})^2 + m^2} + A_o,$$

with equations of motion

$$\dot{\vec{P}} = -\frac{\partial}{\partial \vec{r}}\hat{E}(\vec{P}, \vec{r}, t),$$

and

$$\dot{\vec{r}} = \frac{\partial}{\partial \vec{P}}\hat{E}.$$

In the case of a particle beam transported along a fixed direction z, it is convenient to consider z as a time argument, while the time t can be treated as one of three independent coordinates x, y, t. Hamilton's function and equations of motion in this representation can be quickly derived using the covariant equation for the wave function $\Psi(\vec{r}, t)$, or the relativistic Schroedinger equation

$$[(\vec{E} + A_o)^2 - (\hat{\vec{P}} + \vec{A})^2 - m^2]\Psi = 0,$$

where

$$\hat{E} = i\hbar\frac{\partial}{\partial t} \quad \text{and} \quad \vec{P} = -i\hbar\vec{\nabla}$$

are the time and space components of 4-vector momentum as a quantum operator. In the quasiclassical limit, this equation can be rewritten, optionally, in two possible forms:

$$i\hbar\frac{\partial}{\partial t}\Psi = [\sqrt{(\hat{\vec{P}} + \vec{A})^2 + m^2} - A_o]\Psi \equiv H_t\Psi,$$

with equations of motion

$$\dot{\vec{P}} = -\frac{1}{i\hbar}[H_t, \vec{P}] = \{H_t, \vec{P}\} \rightarrow -\frac{\partial H_t}{\partial \vec{r}},$$

and

$$\dot{\vec{r}} = \frac{\partial H_t}{\partial \vec{P}},$$

or

$$\begin{aligned} i\hbar\frac{\partial}{\partial z}\Psi &= -[\sqrt{(\hat{E} + A_o)^2 - (\vec{P}_\perp + \vec{A}_\perp)^2 - m^2} + A_z]\Psi \\ &\equiv H_z(\vec{P}_\perp, \vec{\rho}, \hat{E}, t, z)\Psi, \end{aligned} \tag{A1}$$

with equations of motion

$$\vec{P}'_{\pm} = -\frac{\partial}{\partial \vec{\rho}}H_z$$

and

$$\vec{\rho}\,' = \frac{\partial}{\partial \vec{P}_\perp}H_z$$

$$\hat{E}' = -\frac{1}{i\hbar}[H_z, \hat{E}] = \frac{\partial H_z}{\partial t}, \qquad t' = -\frac{\partial}{\partial \hat{E}}H_z.$$

Thus, in the z representation Hamilton's function coincides with the canonical momentum (with reversed sign) $P_z = p_z + A_z$ taken as a function of energy and transverse momentum according to the covariant expression $E^2 - p^2 = m^2$.

For a helical structure, it is convenient to consider particle dynamics in terms of a helical frame (x_1, x_2, z), with

$$x_1 + ix_2 = (x + iy)e^{-ikz}. \tag{A2}$$

The new Hamiltonian and equations of motion can be simply found using the wave equation in (A1), taking into account that

$$\vec{\nabla}_\perp \equiv \vec{e}_x\frac{\partial}{\partial x} + \vec{e}_y\frac{\partial}{\partial y} = \vec{e}_1\frac{\partial}{\partial x_1} + \vec{e}_2\frac{\partial}{\partial x_2}$$

and

$$\vec{P}_\perp = \vec{e}_1 P_1 + \vec{e}_2 P_2,$$

while

$$\frac{\partial}{\partial z}\Psi(x, y, z) = \left(\frac{\partial}{\partial z} - kx_1\frac{\partial}{\partial x_2} + kx_2\frac{\partial}{\partial x_1}\right)\Psi(x_1, x_2, z).$$

Thus, the new Hamiltonian is

$$H_h = -\sqrt{(\hat{E} + A_o)^2 - m^2 - (P_1 + A_1)^2 - (P_2 + A_2)^2} + A_z + k(x_2P_1 - x_1P_2). \tag{A3}$$

This is the so-called helical invariant. Since the components of the vector potential A_1, A_2, A_z are functions of only x_1, x_2 (i.e., ρ and $\psi \equiv \varphi - kz$), the Hamiltonian H_h is conserved for any particle trajectory, together with the energy E (assuming no rf and space charge forces).

Solving the equations of motion in a helical structure, one can find the generalized phases $\Psi_\pm$ and adiabatic invariants (quantum numbers) $I_\pm$ as functions of $x_1, P_1; x_2, P_2; E$. In these variables, the Hamiltonian (A3) is a function of only I_+, I_-. and E:

$$I'_\pm = \frac{\partial}{\partial\psi_\pm}H_h(I_+, I_-, E) = 0$$

and

$$\psi'_\pm = \frac{\partial}{\partial I_\pm}H_h(E, I_+, I_-) = kQ_\pm(E, I_+, I_-) = \text{const}. \tag{A4}$$

The energy E, being a global invariant in a magnetic field, is not redefined, but there should appear a new time variable $\hat{t}$ as a canonical phase with a constant rate,

$$\hat{t}\,' = -\frac{\partial}{\partial E}H_h(E, I_+, I_-) = \text{const}, \tag{A5}$$

while the time t on a particle trajectory can be considered as a function of all the new variables including $\hat{t}$ and E. There is a set of differential relationships between the new and old canonical variables [36]. For our situation, the important relationships are

$$\frac{\partial I_\pm}{\partial\overline{P}_\perp} = \frac{\partial\overline{P}}{\partial\psi_\pm} \tag{A6}$$

and

$$\frac{\partial I_\pm}{\partial E} = -\frac{\partial t}{\partial\psi_\pm}. \tag{A7}$$

These can be simply proved comparing the Poisson brackets $\{I_\pm, \vec{\rho}\}$ and $\{I_\pm, t\}$ in terms of old and new variables.

In order to find the dynamical sense of $\hat{t}$, one has to integrate the equation

$$t' = \frac{1}{\beta_z} = \frac{\sqrt{1 + (\vec{\rho}\,')^2}}{\beta}$$

along a solved particle trajectory. The inverse particle velocity β_z^{-1} can be represented as

$$\beta_z^{-1} = \langle\beta_z^{-1}\rangle + \tilde{\beta}_z^{-1},$$

where $\tilde{\beta}_z^{-1}$ oscillates as a function of ψ_+, ψ_-:

$$\langle\tilde{\beta}_z^{-1}\rangle = 0.$$

Note that $\langle\beta_z^{-1}\rangle = 1/\langle\beta_z\rangle$.

If we introduce the waving fraction of time $\tilde{t}$ as

$$t = \langle t\rangle + \tilde{t}(\psi_+, \psi_-), \qquad \langle\tilde{t}\rangle = 0,$$

where

$$\tilde{\beta}_z^{-1} = \tilde{t}\,' = k\left(Q_+\frac{\partial}{\partial\Psi_+} + Q_-\frac{\partial}{\partial\Psi_-}\right)\tilde{t},$$

then the variable $\hat{t}$ can be identified as

$$\hat{t} = t - \tilde{t}(\psi_+, \psi_-).$$

This can be proved by comparing Eq. (A5) to the equation for the original time:

$$t' = -\left(\frac{\partial}{\partial E} + \frac{\partial I_+}{\partial E}\frac{\partial}{\partial I_+} + \frac{\partial I_-}{\partial E}\frac{\partial}{\partial I_-}\right)H_h(E, I_+, I_-) = \hat{t}\,' + kQ_+\frac{\partial t}{\partial\psi_+} + kQ_-\frac{\partial t}{\partial\psi_-}.$$

Note the important relationships which follow from Eqs. (A4) and (A5):

$$\frac{\partial}{\partial I_\pm}\frac{1}{\langle\beta_z\rangle} = -k\frac{\partial}{\partial E}Q_\pm. \tag{A8}$$

These show that the so-called slippage factors, i.e., emittance-related dispersion of the translation velocity $\langle\beta_z\rangle$, are simply proportional to the chromaticity of particle tunes [20,21].

To determine the time t as function of new variables $(a_\pm, \psi_\pm)$, one has to integrate the equation

$$t' = \frac{1}{\beta_z} = \frac{1}{\beta}\sqrt{1 + |\hat{x}' + ik\hat{x}|^2}$$

along a solved particle trajectory. In linear approximation for free particle oscillations near the helical orbit $\vec{a}(p, z)$, we have

$$t' \approx \frac{\sqrt{1 + \kappa^2}}{\beta} + \frac{\kappa(ku_1 + u_2')}{\beta\sqrt{1 + \kappa^2}}.$$

To integrate u_1, we have to substitute u_1 as the solution shown in (3.30):

$$\int dz\cdot u_1 = \int(a_+\cos\psi_+ + a_-\cos\psi_-)dz = \frac{a_+}{kQ_+}\sin\psi_+ + \frac{a_-}{kQ_-}\sin\psi_-.$$

Then we obtain Eq. (3.37). The derivatives $\frac{\partial a_\pm^2}{\partial E}$ can be found using the relationships in (3.31)–(3.34), in which the variables of the rotating frame (x_1, x_1', x_2, x_2') are to be considered as functions of (x, p_x), (y, p_y), and energy E:

$$\hat{x} \equiv x_1 + ix_2 = (x + iy)e^{-ikz},$$

$$\hat{x}' \equiv x_1' + ix_2' = -ik(x + iy)e^{-ikz} + \frac{(p_x + ip_y)e^{-ikz}}{\sqrt{E^2 - m^2 - |p_x + ip_y|^2}}.$$

Thus, we find

$$\frac{\partial \hat{x}}{\partial E} = 0 \quad \text{and} \quad \frac{\partial \hat{x}'}{\partial E} = -\frac{\hat{x}' + ik\hat{x}}{p_z^2}E. \tag{A9}$$

In first approximation, if we neglect the deviations off the equilibrium orbit on the right-hand equation in (A9), then

$$\frac{\partial x_1'}{\partial E} = 0, \qquad \frac{\partial x_2'}{\partial E} = -\frac{ka}{p_z^2}E = -\frac{ka}{E\beta^2}(1 + \kappa^2).$$

Now, we can take the derivatives

$$\frac{\partial}{\partial E}a_\pm^2 = 2\frac{x_2' - \alpha_\mp k(x_1 - a)}{(\alpha_+ - \alpha_-)^2}\left[-\frac{ka}{E\beta^2}(1 + \kappa^2) + \alpha_\pm\frac{kda}{\beta dp}\right] = \pm\frac{2a}{E\beta^2}\frac{[\hat{D}\alpha_\mp - 1 - \kappa^2]}{\alpha_+ - \alpha_-}a_\pm\cos\psi_\pm. \tag{A10}$$

Finally, using the relationship in (3.28), we find Eq. (3.39).

[1] Muon Collaboration, M. M. Alsharo'a *et al.*, Phys. Rev. ST Accel. Beams **6**, 081001 (2003).

[2] A. N. Skrinsky, in *Proceedings of the 2002 Joint USPAS-CAS-Japan-Russia Accelerator School, Long Beach, CA, 2002*, edited by Helmut Wiedemann, Daniel Brandt, Eugene A. Perevedentsev, and Shin-ichi Kurokawa (World Scientific, Singapore, 2004).

[3] Muon Collider Collaboration, C. M. Ankenbrandt *et al.*, Phys. Rev. ST Accel. Beams **2**, 081001 (1999).

[4] S. Geer, Phys. Rev. D **57**, 6989 (1998).

[5] Feasibility Study on a Neutrino Source Based on a Muon Storage Ring, edited by D. Finley and N. Holtkamp, http://www.fnal.gov/projects/muon_collider/nu-factory/fermi_study_after_april1st/

[6] BNL Report No. BNL-52623, 2001, edited by S. Ozaki, R. Palmer, M. Zisman, and J. Gallardo, http://www.cap.bnl.gov/mumu/studyii/FS2-report.html

[7] A. N. Skrinsky and V. V. Parkhomchuk, Sov. J. Part. Nuclei **12**, 223 (1981).

[8] D. M. Kaplan, in *Proceedings of Snowmass 2001, Snowmass Village, CO*, http://www.slac.stanford.edu/econf/C010630/papers/M102.PDF

[9] Invented by Y. S. Derbenev and A. Kondratenko at the Institute of Nuclear Physics in Novosibirsk, the Siberian snake is a device to be inserted into the lattice of a circular accelerator to preserve the polarization of a proton beam during the acceleration process. See [22] below.

[10] R. P. Johnson *et al.*, in *First International Workshop on Hydrogen in Materials and Vacuum Systems*, edited by G. Myneni and S. Chattopadhyay, AIP Conf. Proc. No. 671 (AIP, New York, 2003), pp. 328–335.

[11] Rolland Johnson and Daniel Kaplan, DOE STTR Proposal No. 70255B0I-I, 2002.

[12] R. E. Hartline, R. P. Johnson, M. Kuchnir, C. M. Ankenbrandt, A. Moretti, M. Popovic, D. M. Kaplan, and K. Yonehara, http://www-mucool.fnal.gov/mcnotes/public/pdf/muc0285/muc0285.pdf

[13] Sanborn C. Brown, *Basic Data of Plasma Physics, The Fundamental Data on Electrical Discharges in Gases, American Vacuum Society Classics* (AIP, New York, 1993), p. 149.

[14] MICE Collaboration, G. Gregoire *et al.*, http://hep04.phys.iit.edu/cooldemo/micenotes/public/pdf/MICE0021/MICE0021.pdf

[15] http://www.muonsinc.com/

[16] http://wwwasd.web.cern.ch/wwwasd/geant4/geant4.html

[17] Y. Derbenev, http://www-mucool.fnal.gov/mcnotes/public/ps/muc0108/muc0108.ps.gz

[18] V. Balbekov, http://www-mucool.fnal.gov/mcnotes/public/ps/muc0246/muc0246.ps.gz

[19] Al Garren, Harold Kirk, and Steve Kahn, http://www.fnal.gov/projects/muon_collider/eexchange/workshop03/garren.pdf; see also http://www.physics.ucla.edu/hep/mc/tucson/rc2003.htm

[20] Steve Kahn, Alper Garren, and Harold Kirk, http://www.fnal.gov/projects/muon_collider/eexchange/workshop03/kahn1.pdf

[21] M. Syphers E. Courant, W. Fischer, A. Luccio, F. Mariam, S. Peggs, F. Pilat, T. Roser, S. Tepikian, N. Tsoupas, E. Willen, T. Katayama, K. Hatanaka, T. Kawaguchi, M. Okamura, T. Tominaka, H. Wu, V. Ptitsin, and Y. Shatunov, in *Proceedings of the 1997 Particle Accelerator Conference, Vancouver, Canada* (IEEE, Piscataway, NJ, 1997).

[22] Ya. S. Derbenev and A. M. Kondratenko, in *High Energy Physics with Polarized Beams and Polarized Targets*, edited by G. H. Thomas, AIP Conf. Proc. No. 51 (AIP, New York, 1979), p. 292.

[23] E. Willen, M. Anerella, J. Escallier, G. Ganetis, A. Ghosh, R. Gupta, M. Harrison, A. Jain, W. MacKay, A. Marone, J. Muratore, S. Plate, R. Thomas, P. Wanderer, and K. C. Wu, in *Proceedings of the Particle Accelerator Conference, Portland, OR, 2003* (IEEE, Piscataway, NJ, 2003).

[24] V. Balbekov *et al.*, http://www-mucool.fnal.gov/mcnotes/public/pdf/muc0202/muc0202.pdf

[25] A. Artamonov, Ya. Derbenev, and N. Inozemtsev, Sov. Phys. Tech. Phys. **34**, 380 (1989).

[26] A. Artamonov, Ya. Derbenev, and N. Inozemtsev, Sov. Phys. Tech. Phys. **34**, 495 (1990).

[27] L. D. Landau and E. M. Lifshits, *Electrodynamics of Continuous Media* (Pergamon, Oxford, 1984), 2nd ed.

[28] A. A. Kolomensky, Sov. At. Energy **19**, 1511 (1965).

[29] Y. M. Ado and V. Balbekov, Sov. At. Energy **39**, 40 (1971).

[30] Ya. Derbenev and A. Skrinsky, Sov. Phys. Rev. **1**, 165 (1981).
[31] http://en.wikipedia.org/wiki/Langevin_equation
[32] R. A. Alvarez, Rev. Sci. Instrum. **57**, 2481 (1986).
[33] Z. D. Farkas *et al.*, in *Proceedings of the IX International Conference on High Energy Accelerators, Stanford, CA* (SLAC Report No. SLAC-PUB-1453, 1974), p. 576.
[34] Rolland Johnson and Yaroslav Derbenev, DOE SBIR proposal No. 72180B03-I, 2003.
[35] Yaroslav Derbenev and Rolland P. Johnson, in *Proceedings of the International Conference on Beam Cooling (COOL2003), Mt. Fuji, Japan, 2003*, http://members.aol.com/muonsinc/COOL03_6-d_rev1.pdf; Nucl. Instrum. Methods Phys. Res., Sect. A (to be published).
[36] L. D. Landau and E. M. Lifshits, *Mechanics*, Course of Theoretical Physics Vol. I (Pergamon, Oxford, 1978), 3rd ed.

A Simple Beam Line for the MuCool Test Area

Charles M. Ankenbrandt, David Harding,
James Lackey, Elliott McCrory, Milorad Popovic,
Fermi National Accelerator Laboratory

Daniel Kaplan, Katsuya Yonehara,
Illinois Institute of Technology

Robert E. Hartline, and Rolland P. Johnson
Muons, Inc.

Feb. 9, 2004

Abstract

This note describes a simple beam line to transport H^- beam from the end of the Fermilab 400 MeV Linac to the MuCool Test Area (MTA). The design uses existing dipoles and quadrupoles and other equipment now available at Fermilab. Deflection of single 15 Hz beam pulses from the Linac to the MTA is accomplished using pulsed magnets that are essentially Main Injector trim dipoles with thinner laminations. The beam size is kept small to control beam losses and allow the use of existing surplus or spare equipment. An upgrade of the beam line to illuminate larger objects at high intensity is described.

Introduction

The MuCool Test facility will be used to test liquid hydrogen absorbers for muon beam cooling for a Neutrino Factory or Muon Collider as well as to test high gradient RF cavity structures and cavities that are cryogenically-cooled or superconducting. At first this equipment will be tested without beam. Later, after the beam dump and shielding berm are finished, the equipment will be tested with beam.

To test liquid hydrogen absorbers, the MuCool experimenters would ultimately like a beam of H^- or protons with 400 MeV kinetic energy, 50 mA peak current, and 50 microsecond pulse length at 15 Hz with variable beam size (from 1 to 30 cm at the device under test). Of course this beam must be delivered with tolerable beam losses. These demanding requirements, particularly the high intensity and the desired variability in beam size make the optics, operation, and shielding of such a facility particularly challenging and costly.

However, a beam with limited integrated intensity and small transverse size will satisfy the initial needs of some of the experimenters, such as tests of pressurized RF cavities by Muons, Inc. and the irradiation of detector components with small intensity beams or short bursts of high intensity pulses for MuCool. Accordingly, this note presents a simple design of a conventional beam line that can be built in the near future based on

components that are now available as spare parts or left over from previous projects. This design can be upgraded to provide the full capabilities required for complete testing of large devices with intense beam. The simple beam line design, components, cost, and operating conditions, as well as an upgrade for testing objects of large transverse dimensions, are discussed below.

Beam Line Design

The design presented here is based on using eight of the fifteen spare quadrupoles from the Linac to Booster transfer line and six dipoles from the decommissioned Electron Cooling Ring.

Extraction

The beam will be directed toward the MuCool Test Area using two pulsed dipole magnets with the first located after the last Linac accelerating module and just before the Q74 quadrupole and the second just downstream of the chopper. At 400 MeV, this pair of magnets will produce a horizontal bend of 5 degrees. The magnets will pulse fast enough to allow only one of the Linac's 15 Hz beam pulses to be selected by an appropriate T-clock event, just as the NTF operates now.

There are at present two options for the pulsed magnet and power system to be used for extraction from the Linac. The first option is to use a pair of new magnets based on a Main Injector trim magnet design with a corresponding power supply designed by Dan Wolff. A second option would be to build a new copy of the 32-degree NTF magnet, which could be powered by a spare Transrex power supply. Here we describe only the first option, which seems more desirable considering long-range maintenance.

Pulsed Extraction Magnet Design

To achieve the required 5-degree bend while keeping the magnetic field under 0.65 T to avoid stripping the H- ions, we use two identical magnets, one on either side of the chopper. The magnets are built using laminations from IDH dipoles (Main Injector horizontal trims) with a hollow conductor coil for lowered inductance and improved cooling. The first magnet bends the beam 2.5° (44 mr). The second magnet is centered 1.75 m downstream of the first, on the other side of the chopper where the beam is separated from the straight Linac beam by 7.6 cm. A 5 cm (2 inch) diameter vacuum pipe carries both beams through the first magnet. Two pipes pass through the second magnet after the chopper with the straight beam passing between the coils and the extracted beam passing through the center of the magnet as shown in figure 1.

Standard 0.635 mm laminations of transformer steel are suitable for pulsed operation. The IDH die exists and is in good shape. Figure 1 shows the lamination profile and DC field distribution. The coils are three layers of seven turns each on each pole. The conductor is 10.4 mm square copper with a 5.8 mm cooling water passage. The coils are wrapped in fiberglass tape and vacuum impregnated. Each magnet needs to contribute 0.14 T-m to the bend. Scaling from the IDH measurements, the dipoles will need to run

at 385 A. The water flow is sufficient at this current to allow DC operation, so pulsed mode operation will be stable.

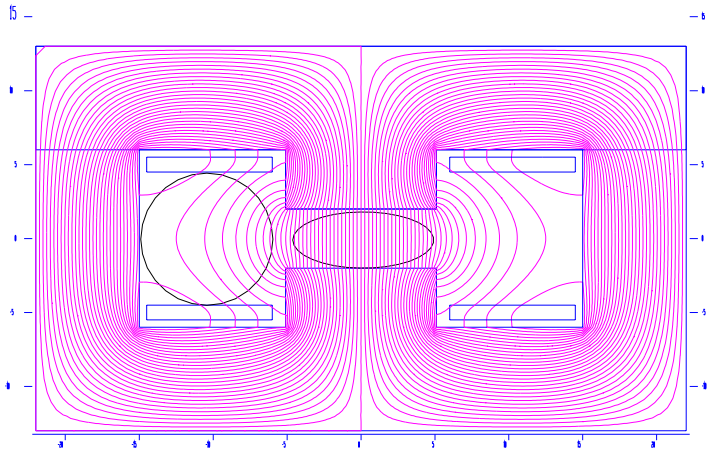

Figure 1. IDH dipole (Main Injector horizontal trim) profile showing field calculation. In the case of the second, downstream pulsed magnet, the straight-ahead Linac beam pipe passes through the magnet between the coils as shown by the circle in the figure.

Wolff Pulsed Power Supply

The estimated cost of a pulser for the magnets described above is based on two 1 meter magnets operating at 0.14T with a 3"x3" aperture. This corresponds to 90 joules of stored energy. Another 40% has been added to account for fringing and end effects (total=126 joules). Depending on the eddy-current losses, the estimate ranges from $8k to $18k for component costs, where the lower value would correspond to using a ceramic beam pipe. The estimates do not include any accelerator controls modules, the cost of cables (controls, load, and AC), or the cost of cable installation (electricians).

Linac Modifications

In order to place the first pulsed magnet upstream of the chopper, the prototype bunch length detector (BLD) can be removed (gaining 9 inches) and the quadrupole and wire scanner can be reconfigured to be closer together, as they are in other areas of the Linac, (gaining another 3 inches). These components are shown in figure 2. The development of the BLD can continue using the other two BLDs that are installed elsewhere.

The round cover on the downstream end of the Chopper shown in figure 3 has to be modified to accommodate the second new, pulsed dipole. The beam pipe to the Booster and the one to the MTA separate at the cover and pass through the downstream pulsed-dipole as shown in figure 1.

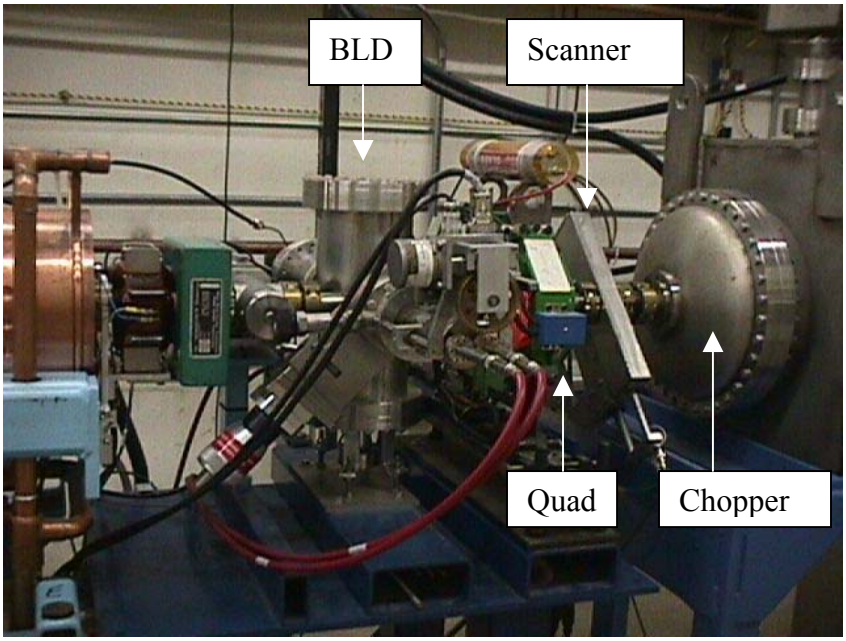

Figure 2. Proposed upstream pulsed-magnet location. The Bunch Length Detector (BLD) can be removed, and the Quadrupole and Wire Scanner can be moved closer together nearer to the chopper to free up twelve inches for the pulsed magnet.

Figure 3. Area downstream of the Chopper. The Wire Scanner and the Transformer can be moved downstream. The downstream cover on the Chopper will have to be modified to allow the insertion of the downstream pulsed magnet with the two beam pipes as indicated in figure 1

Linac to MTA Extraction Area

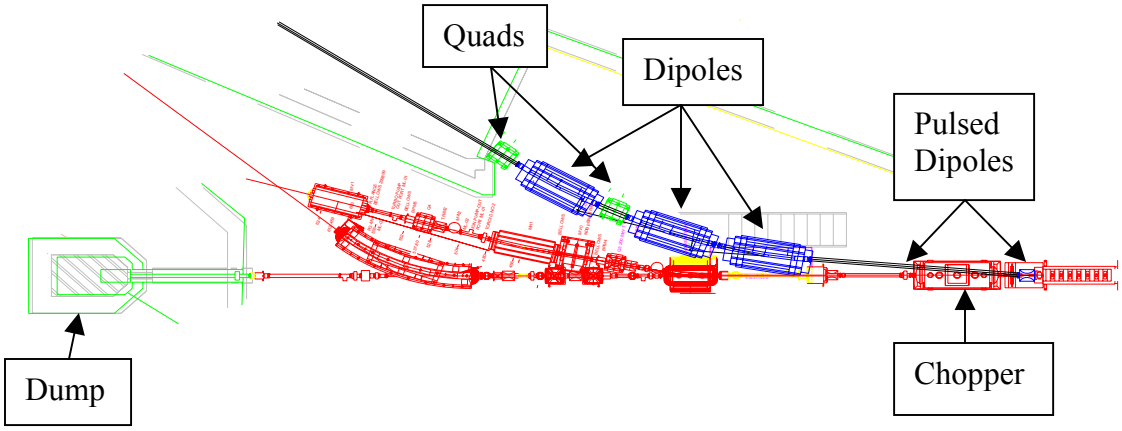

Figure 4. Extraction Area showing the new beam line to the MTA.

Linac to MTA Beam Line

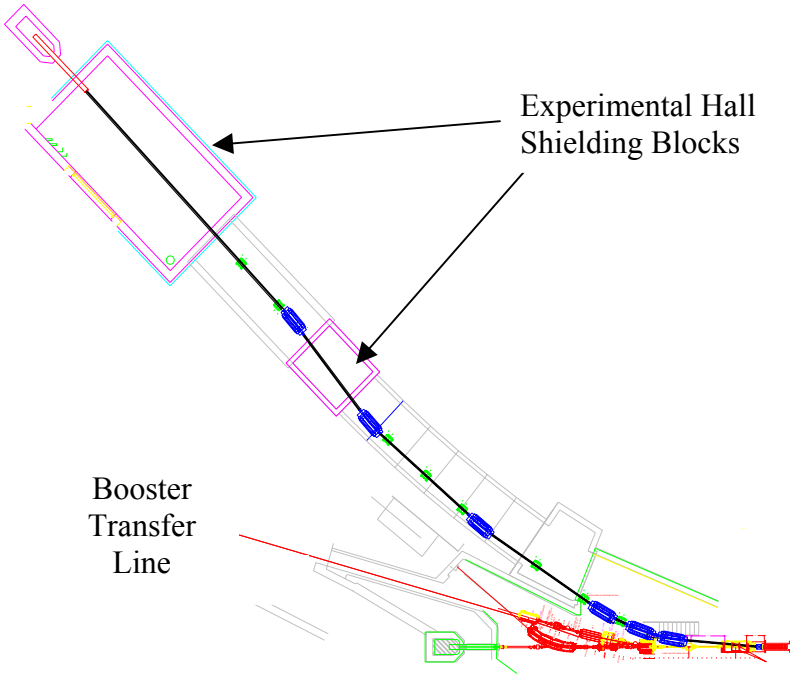

Figure 5. MTA Beam Line schematic, showing the six dipoles and eight quads.

Five bending magnets each bend the beam 9 degrees to the right and the sixth bending magnet bends the beam to the left 9 degrees, as shown in figure 5.

Beam Transport Simulations

A TRACE 3-D beam transport simulation starting from the upstream end of the last Linac module is shown in figure 6. In this simulation the last dipole magnet and two quadrupoles are just after the Linac shielding wall such that the beam drifts through the experimental enclosure to the dump area. Input beam parameters in the figure correspond to measured values.

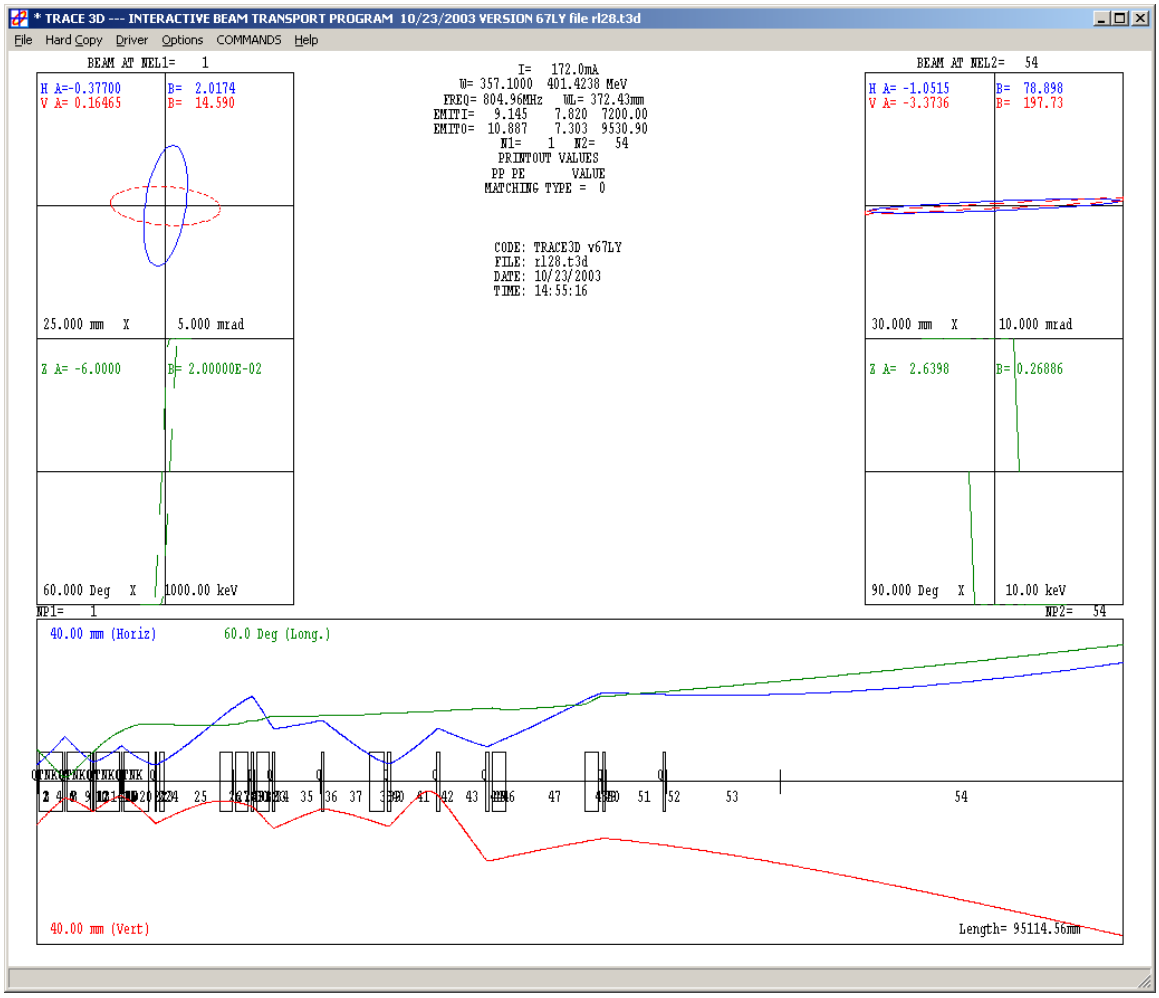

Figure 6. TRACE 3-D simulation of the proposed beam line. The blue line is the horizontal and the red line is the vertical beam envelope. The green line is the bunch length in degrees of 805 MHz RF wavelength.

The total emittance of the equivalent uniform beam (the beam followed by TRACE 3-D) in each phase plane is five times the rms emittance in that plane, and the displayed beam envelopes are $\sqrt{5}$ -times their respective rms values. Real beams have ill-defined

boundaries and, in general, one can expect a few percent (<10%) of the particles in a real beam to be outside the boundaries displayed by TRACE 3-D.

Real Estate and Utilities

Electrical power for the magnets is available from the L3 1500kVA transformer in the lower Linac gallery. This transformer powered the 200 MHz RF stations that were removed when the Linac was upgraded to 400 MeV. In the Linac lower gallery there is space for the power supplies. One Transrex power supply will power the pulsed magnet and two more will power the two groups of three dipoles. The same gallery will also house the rack with the six power supplies (similar to PowerTen) needed for the quadrupoles. Power cables will enter the Linac enclosure using existing linac penetrations. The two quadrupoles and any other magnets in the Experimental enclosure will be powered using power supplies housed in the Cryo Building and will get power from the MuCool transformer.

Operating Conditions

We believe that beam switching from the Linac will be clean such that we will lose less than 1% of the beam within the Linac enclosure. The H- beam will be transported to the last bending magnet in the Linac enclosure where a proton beam can be generated using a stripping foil. The magnet body and the enclosure shielding-wall will absorb unstripped H atoms. The number of particles that will be delivered to the area will be controlled with three independent parameters: repetition rate, pulse width, and Linac current. The present Linac can deliver a maximum of 50 mA of H^- for up to 50us, at up to a 15 Hz rate.

Any of these three parameters can be smaller by a factor ten or more. The maximum beam intensity may be limited by the installed shielding. The allowed beam loss within the Linac enclosure will be controlled by a loss monitor (sc200) in the Linac gallery and a monitor on the top of the berm. These monitors will inhibit beam on a pulse-to-pulse basis.

The line is designed under the assumption that loss can occur only in an accident condition. The pulsed magnet power supply and the power supply for the first three horizontal bending magnets will be the two critical devices that prevent beam from entering the MuCool experimental area.

An Upgrade for Objects with Large Transverse Dimensions

It is difficult to duplicate the qualities of muon beams to be found in future muon colliders or neutrino factories with the Fermilab Linac beam. Besides the fact that muons have different energy loss behavior than protons, it is difficult to make the pulses short and intense enough to mimic beams in these future machines. As examples, a beam pulse for a collider may have 10^{13} muons in a few nanoseconds while a neutrino factory beam

may have 10^{13} muons in a few microseconds. However, with a maximum current of 50 mA, it takes 32 microseconds to accumulate 10^{13} particles with the Linac.

Thus, any experiment to test equipment for these uses must have a plan to simulate the beam is some believable way. For large aperture liquid hydrogen energy absorbers it has been assumed that the MuCool test area should have the ability to illuminate an absorber with a wide beam by means of a system of large-aperture quadrupoles. However, we note that the narrow beam that is the subject of this paper can be scanned across the absorber with a system of programmed dipoles to illuminate the absorber with considerable flexibility and reduced cost. In this case the dipoles would be arranged to form a three or four-bump in each transverse plane such that the beam could be directed to the beam dump after passing through the absorber.

With such a scanned beam, the instantaneous rates (particles/s/mm^2) in each region of the absorber can be made to be more like those of cooling applications to be simulated.

Components and Costs

All magnets except the pulsed dipoles used for extraction (and the programmed dipoles that could be used in an MTA upgrade to the beam line for scanning large test devices) exist and are available. The spare Linac quads should be ready, though the six dipoles will probably need to be refurbished at some additional cost. Trim magnet specifications should be made considering the availability of existing magnets and supplies.

Eight quadrupoles can be powered by 30V/320Amp or 50V/60Amp power supplies that are standard power supplies used in the AD. The six dipoles from the Electron Cooling Ring experiment can be powered in groups of three using two Transrex power supplies from decommissioned Fixed Target Lines. As discussed above, the pulsed extraction magnets can be powered by an available Transrex or by a special supply that would be built according to contemporary AD standards.

The vacuum system, including pipes, bellows, pumps, power supplies, and pressure readouts, can be constructed from materials from decommissioned beam lines. Diagnostics, readouts, and control system components may also be available, although compatibility requirements with the accelerator controls may dictate some additional expenses to minimize total operation and construction costs.

In all cases, the detailed design of the beam line should be made with available components to minimize costs and to facilitate a timely construction schedule.

Acknowledgment

We thank Dan Wolff for his help in estimating the power supply parameters for the pulsed magnets.